UNLV Theses, Dissertations, Professional Papers, and Capstones

December 2017

Numerical Characterization of the Flow Field and Heat Transfer Inside the Receiver of a Parabolic Trough Solar Collector Carrying Supercritical Co2

Samad Gharehdaghimollahajloo
University of Nevada, Las Vegas, gharehda@gmail.com

NUMERICAL CHARACTERIZATION OF THE FLOW FIELD AND HEAT TRANSFER

INSIDE THE RECEIVER OF A PARABOLIC TROUGH SOLAR COLLECTOR

CARRYING SUPERCRITICAL CO$_2$

By

Samad Gharehdaghimollahajloo

Bachelor of Science – Mechanical Engineering

K. N. Toosi University of Technology

1998

Master of Science – Mechanical Engineering

University of Tehran

2009

A dissertation submitted in partial fulfillment

of the requirements for the

Doctor of Philosophy – Mechanical Engineering

Department of Mechanical Engineering

Howard R. Hughes College of Engineering

The Graduate College

University of Nevada, Las Vegas

December 2017

UNLV | GRADUATE COLLEGE

Dissertation Approval

The Graduate College
The University of Nevada, Las Vegas

September 8, 2017

This dissertation prepared by

Samad Gharehdaghimollahajloo

entitled

Numerical Characterization of the Flow Field and Heat Transfer Inside the Receiver of a Parabolic Trough Solar Collector Carrying Supercritical CO2

is approved in partial fulfillment of the requirements for the degree of

Doctor of Philosophy – Mechanical Engineering
Department of Mechanical Engineering

Samir F. Moujaes, Ph.D.	Kathryn Hausbeck Korgan, Ph.D.
Examination Committee Chair	*Graduate College Interim Dean*
Brendan O'Toole, Ph.D.	
Examination Committee Member	
Hui Zhao, Ph.D.	
Examination Committee Member	
Alexander Barzilov, Ph.D.	
Examination Committee Member	
Samaan Ladkany, Ph.D.	
Graduate College Faculty Representative	

ii

Abstract

NUMERICAL CHARACTERIZATION OF THE FLOW FIELD AND HEAT TRANSFER
INSIDE THE RECEIVER OF A PARABOLIC TROUGH SOLAR COLLECTOR
CARRYING SUPERCRITICAL CO_2

By

Samad Gharehdaghimollahajloo

Dr. Samir F. Moujaes, Examination Committee Chair

Professor, Department of Mechanical Engineering

University of Nevada, Las Vegas

The aim of this research is to provide a detailed numerical analysis of flow field and heat transfer inside the heat collecting element of a parabolic trough collector. The parabolic trough collector is used as the boiler in a direct Super Critical Carbon Dioxide (S-CO2) Brayton cycle.

A single collector is modeled and analyzed with different inlet conditions. The working fluid is supercritical since its pressure is increased to above critical pressure in the compressor while its temperature reaches 300 °C after passing through the recuperators and before entering the solar field. For the first time, this research considers both the non-uniform solar radiation irradiance around the trough receiver and the natural convection inside the receiver combined with the nonlinear variations in the physical properties of S-CO_2.

Moreover, to investigate the variations in the outputs during a typical day a pseudo steady state scheme is applied. The changes in ambient conditions are so slow compared to the variations in the flow field that in each time step the flow filed is considered to fulfill the steady state conditions. Hence, steady state numerical analysis is repeated for five time-steps (8 AM, 10 AM, 12 PM, 2 PM and 4 PM) and the results are graphed. A curve is then fitted to the thermal efficiency graph and outlet temperature of receiver graph to let the user interpolate the middle time steps.

Acknowledgements

Dedication

Dedicated to my family and the many friends who supported me on this journey.

Table of Contents

List of Tables

List of Figures

List of Abbreviations and Acronyms

ANSI	American National Standards Institute
Btu	British thermal unit
CF	capacity factor
CO_2	carbon dioxide
CPV	concentrating photovoltaics
CSP	Concentrated Solar Power
DNI	Direct-Normal Irradiance
DOE	Department of Energy
E	equation of time
G	Irradiance (W/m^2)
GHG	Green House Gases
GWh	Giga Watt Hour
GWP	Global Warming Potential
h	convection coefficient
ha	hectare
HTF	Heat Transfer Fluid
I	Irradiation for an hour
LCOE	Levelized Cost of Energy
MW	Mega Watt
MW_{ac}	Mega Watt of Alternative Current
Nu	Nusselt number
ODP	Ozone Depletion Potential
PTC	Parabolic Trough Collector
PV	photo voltaic
Re	Reynolds number
$S\text{-}CO_2$	Supercritical carbon dioxide
SNL	Sandia National Laboratory
t	Local time
t_s	Solar time
T_a	Ambient temperature
T_{dp}	Dew point temperature
T_s	Sky equivalent temperature
TES	Thermal Energy Storage
G_{SC}	Solar Constant

Greek

α	Absorptance
α_s	Solar altitude angle
β	Slope of surface

γ	Surface azimuth angle
γ_s	Solar azimuth angle
δ	Solar Declination
ε	Emittance
η	Efficiency
θ	Angle, Angle between surface normal and incident radiation
θ_z	Solar zenith angle
λ	Wavelength
μ	Dynamic viscosity
ν	Kinematic viscosity
ρ	Reflectance, Density
σ	Stefan-Boltzmann constant
φ	Latitude
ω	hourly angle

Chapter 1: Introduction

1.1 Solar Energy in the USA: Past, Present and Future

Investing in solar energy is beneficial for the United States in several ways. First and foremost, replacing fossil-fuel combustion with renewable energies like solar energy reduces air pollutants and greenhouse gases. Second of all, sunlight is a free resource. Hence, once solar technologies are installed, they require minimal non-solar inputs and their operating and maintenance (O&M) costs are very low. Consequently, in contrast to conventional fuels, solar energy market never suffers from supply disruptions and price volatility that are common in other energy sectors. Last but not least, investing on domestic solar energy industry is expected to create a growing number of jobs in renewable energies sector [1].

Regarding these facts the Department of Energy (DOE) is leading programs like CSE/PV roadmap and SunShot Initiative to expedite the solar industry growth. The main goal of SunShot Initiative is "to reduce the price of solar energy systems by about 75% between 2010 and 2020" [2]. The U.S. Solar industry achieved a record year in 2014, only three years after the beginning of SunShot Initiative program, by installing about 7,000 megawatts (MW) of solar electric capacity which set 34% growing over 2013. About 90 % of the installed capacity was within the PV sector, while installing 767 MW of concentrating solar power led to largest yearly growth ever in this sector. Together, 32% of all new electricity generating capacity in the U.S. was in solar industry- second only to the natural gas [3].
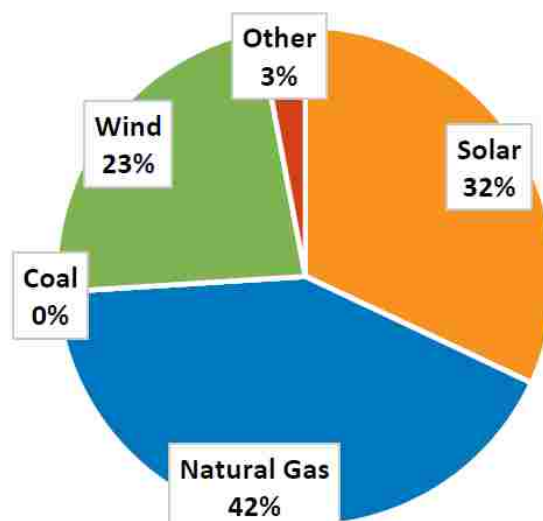
Figure 1 New Electric Capacity Installed in 2014 [3]

While the Photo Voltaic (PV) sector is currently the leading sector in growing solar industry, Concentrated Solar Power (CSP) is increasingly getting more share of the market. In last three

decades, CSP market growth in the USA has been sporadic. The first large CSP plants were built in California in the late 1980s. However, after building those power plants almost 15 years passed before the next commercial CSP plant was built. Then during 2007–2010 a number of new CSP plants were built in the United States and Spain. At the end of 2010, almost 10 GW of CSP projects were under development in the United States. By the end of that year, total installed CSP capacity in the world was about 1,300 MW, with 512 MW in the United States. Since then every year a number of CSP plants are installed and operated. Meanwhile the costs of CSP have been reduced slightly but still they are significantly more than those of conventional power plants. However, SunShot target for CSP technology is to reach $3.60/W installed system price with 14 hours of thermal storage capacity which is expected to enable this solar technology to be competitive in the wholesale electricity market by the end of decade.[1] To meet this goal DOE encourages researches and inventions in five sub-systems: solar field, HTF, TES, cooling technology, and power block (Figure 2).
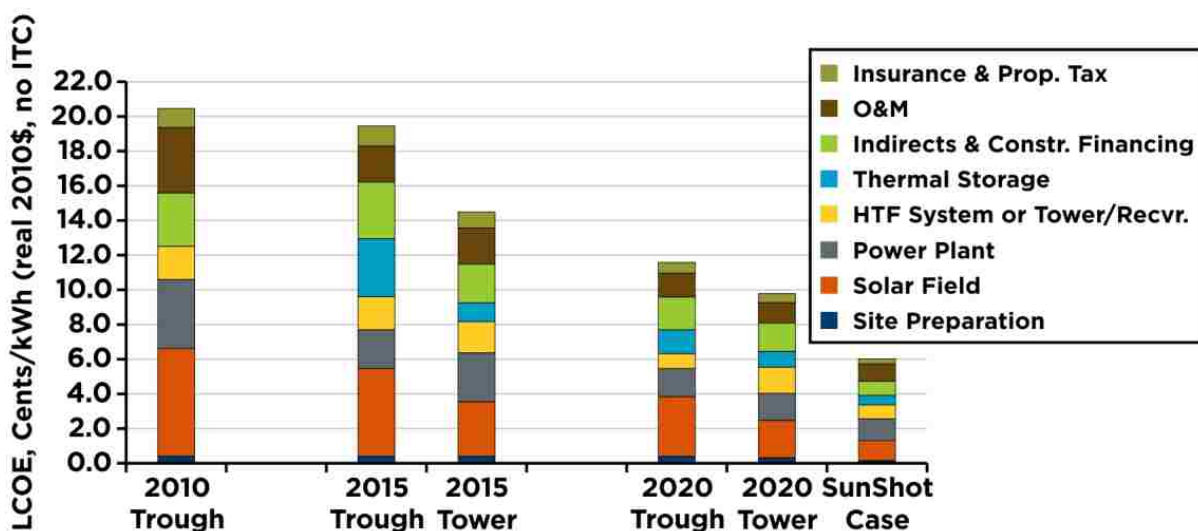
Figure 2 Current and Projected Costs for CSP Trough and Tower Technologies [2]

Alternative power cycles -such as supercritical steam, supercritical carbon dioxide Brayton, and air Brayton are investigated in recent decades as a solution to address these requirements. These power cycles offer the potential to increase the efficiency and/or decrease the cost of the power block. Among these methods, supercritical steam Rankine cycle is the most mature. Indeed, this method already exists at commercial utility-scale fossil fuel-fired plants. However, combining existing supercritical steam power plants with CSP systems might be quite challenging because most of these power plants are 400 MW electric or larger and may need

---

[1] "$/W" unit refers to 2010 U.S. dollars per watt-alternating current (AC) for CSP

to be scaled down to better accommodate CSP systems. Commercial natural gas Brayton cycles also currently exist while, S-CO_2 and air-Brayton systems are still in pilot and demonstration scale, respectively. The idea of utilizing supercritical carbon dioxide as the working fluid can be applied in a variety of thermal power plants including concentrating solar power plants. Two main candidates, among CSP systems, to combine with S-CO_2 cycles are central receiver systems and parabolic trough systems.

The aim of this research is to provide a detailed numerical analysis of heat transfer and flow field inside the receiver of a parabolic trough power plant which works on a direct S-CO_2 Brayton cycle. For the first time this research takes into account both the non-uniform solar radiation irradiance around the trough receiver and the natural convection inside it combined with the highly nonlinear variations in the physical properties of S-CO_2.

1.2 Why CSP?

PV currently is and for the coming decades will expectedly remain the greater sector in the solar industry market. However, its unstable nature makes huge problems in grid operation. In contrary, during slight changes in solar radiation, such as when a cloud passes overhead, CSP can provide stability in plant output because of its built-in thermal inertia. More importantly, CSP plants can be combined with fossil-fuel backup/hybridization, thermal energy storage (TES), or both to achieve higher levels of stability and dispatchability in addition to increased duration of energy output. These characteristics provide a stable energy resource that improves grid operations and allow CSP plants to earn capacity credits similar to those for fossil-fuel power systems [1]. Lastly, the efficiency of CSP plants are higher than PV systems and with the advent of direct S-CO_2 hybrid cycles it is expected to reach even higher efficiencies [19].

1.3 CSP Potential in the USA

CSP plants use mirrors or lenses to collect and focus direct-normal irradiance (DNI), i.e., part of solar radiation that can effectively be reflected or focused by mirrors and lenses, on a receiver element which absorbs the solar irradiance and transfers the heat to the working fluid. Therefore, in general, arid lands within 35° north and south of the equator offer the most

suitable conditions for constructing CSP plants. Southwest of the United States, which enjoys some of the best solar resources on the globe, is hence the best location for constructing CSP plants is the country. However, besides abundant solar resource, a potential region should have several other criteria for the effective deployment of large concentrating solar power plants. The land must be unoccupied, relatively flat, and suitable for development. To estimate the quantity of land suitable for constructing CSP and the amount of electrical energy that might be generated various assessments of the Southwest are performed. Figure 3 illustrates locations in the Southwest USA with characteristics ideal for CSP systems [10, 1].
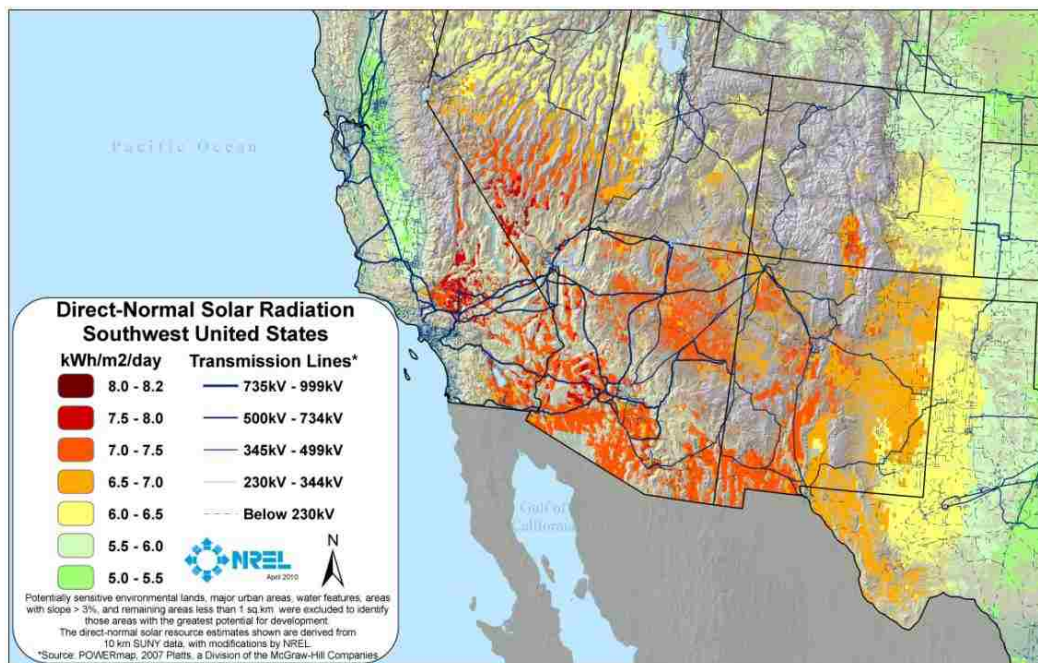
Figure 3 Areas with the best potential for CSP in the USA [10]

In total 22,593,000 hectare area is available in seven states including Utah, New Mexico, Arizona, Nevada, Texas, California, and Colorado. This relatively small area has nearly 7,500 GW of resource potential and assuming a capacity factor of 27% can annually generate more than 17.5 million gigawatt-hours (GWh) electricity [10,11]. The potential energy production exceeds U.S. demand by a factor of more than four. This estimation is however dependent in the technology and level of thermal energy storage deployed and hence capable of future growth [10,1].

State	Available Area (ha)	Capacity (GW)	Annual Electricity (GWh)
Utah	6,031,600	1,987	4,700,000
New Mexico	5,272,200	1,737	4,108,000
Arizona	3,525,700	1,162	2,748,000
Nevada	2,872,300	946	2,238,000
Texas	1,650,800	544	1,286,000
California	1,626,000	536	1,267,000
Colorado	1,614,100	532	1,258,000
Total CSP Resource	22,593,000	7,444	17,605,000

Table 1 Ideal CSP Resource Potential and Land Area in Seven Southwestern States

1.4   Literature Review

S-CO_2 is suggested to be utilized in a variety of solar power generation systems. Yamaguchi, H. et al. [61, 63] experimentally investigated the application of S-CO_2 in a Rankine power cycle where evacuated tubes were used as the heater of the cycle. In 2007 Zhang, X. R., Yamaguchi, H. et al. [62] developed a theoretical analysis of the same cycle. Chen, L et al. (2014) [64] used evacuated tubes carrying S-CO_2 with natural convection to produce hot water as hot as 80 ^{0}C. They achieved thermal efficiencies generally above 60 % which is much higher than previous natural water based and trans-critical CO_2 flow based convection collectors.

Song, Y. et al. (2012) [65] proposed a transcritical CO_2 power cycle driven by solar energy which uses the cold heat rejection to a liquefied natural gas (LNG) evaporation system. They used a flat plate solar collector as the heater and introduced a thermal storage system to provide stable power. The results showed that the main parameter in defining the net power output of such a system the amount solar radiation over a day. In addition, Song, Y. et al. (2012) [65] showed that equipping the system with the thermal storage tank allows it to generate power long after sunset. Their results also showed that there is an optimum turbine inlet pressure under given conditions where both the net power output and the system efficiency reach maximum values. Finally, Song, Y. et al. (2012) concluded that while the change in the turbine inlet temperature has a limited effect on the net power output and the system efficiency, the condensation temperature dominantly affects the system performance.

After years of development central receiver solar power plants finally reached full commercial operation in the last decade with the PS10 plant in Spain. Efforts to increase the thermal efficiency of this type of solar power plants, as the key parameter in reaching a competitive levelized cost of electricity, have been concentrated on two different methods: increasing the temperature of working fluid or/and using alternative power cycles like S-CO$_2$. Among a variety of alternative power cycles, the supercritical and transcritical closed Brayton cycles working with carbon dioxide are deemed interesting. This cycle, first proposed by Feher and Angelino [66, 67], has been studied for the last 40 years. Although Feher and Angelino initially suggested their cycle for nuclear power production in gas reactors, its applicability to solar power plants has also been explored [68, 70, 71, and 72].

Past efforts to study the S-CO$_2$ Brayton cycle have mostly been theoretical and focused on the general aspects of the cycle [15, 16, 35 and 43]. For instance Carstens et al. [73] and Dostal et al. [15] studied different layouts to increase cycle efficiency.

In recent years however, researchers increasingly tend to study different components of S-CO$_2$ Brayton cycle solely and much more in detail. From the point of view of main power plant equipment, Vilim et al. [74] and Gong et al [16] analyzed the necessary features of turbomachinery while Utamura [75] studied heat exchanger layouts. Yet, a major obstacle towards building a direct S-CO$_2$ Rankine cycle is to develop components specially designed for S-CO$_2$. To respond to this requirement SNL began efforts to manufacture an S-CO$_2$ Brayton cycle in recent years. After accomplishing an experimental study on low pressure closed Brayton cycles SNL is now working to develop large (>10 MW) S-CO$_2$ Brayton units for various electrical production schemes [17, 40].

Meanwhile a number of researchers developed computational analysis as an effective tool to improve the efficiency of supercritical power cycles. These analysis address a wide range of problems related to design and operate S-CO$_2$ power cycles including thermal – fluid analysis of heat exchangers or heat collector elements. Most of the past numerical analysis were restricted to simplified models like a tube exposed to the uniform heat flux [44] or heat augmentation by utilizing a var

iety of methods in a receiver tube which carries S-CO$_2$ [45, 52]. However, recently numerical simulation of the simplified models is being replaced with the more realistic models of the power plant equipment. As far as parabolic trough power plants are considered, part of these computational analyses are focused on the flow field and heat transfer around the heat collector

elements [24, 26, 49, 50, 51, 54] while a number of them simulate the flow field inside the receiver [8, 23, 34, 47, 52, 76, 77]. Most of the later simulate either super critical steam or oil as working fluid.

1.5   Summary and Objectives of the Research

Most of the previous computational simulations of Parabolic Trough Collectors (PTC) have simplified the heat flux on the receiver and hence have ignored the nonuniform nature of the flow field and heat transfer in PTC. In addition, most of the correlations that are developed analytically to predict the heat transfer and thermal efficiency of PTC are developed based on simple boundary conditions. A constant heat flux or a uniform temperature profile on the receiver are two most popular boundary conditions used in these analyses. In practice however, the nonuniform solar irradiance on the surface of the absorber tube results in a nonuniform heat flux, which in turn heats the flow asymmetrically and thus forms a highly nonuniform flow field. In order to accurately predict the heat transfer rate in the receiver, a three-dimensional computational fluid dynamics model is developed. The beam component of solar irradiation is reflected by a parabolic LS2 reflector and is concentrated on one side of the glass cover of a receiver tube while the diffuse component of solar irradiation heats up the entire system including the glass cover of the receiver uniformly. In addition, both the LS2 reflectors and the receiver tube emit thermal radiation to the surroundings including sky. The solar irradiance transmits through the glass cover of the receiver and emits to the absorber tube. While a large part of this irradiation is absorbed by the receiver and conducted to the flow inside, a small fraction of it reflects back on the cover glass. One of the contributions of this research is to model such a sophisticated network of heat transfer between different components of the system and the surroundings without implying any simplified boundary conditions.

Moreover, while past studies on heat transfer in PTC were mostly focused on supercritical steam, in this research the receiver is assumed to carry S-CO$_2$ which is widely believed to be the best candidate for working fluid in next generation of thermal power plants.

A detailed full-scale analysis of the flow field and heat transfer inside the receiver is conducted. The results are demonstrated by temperature, pressure, velocity and turbulent parameters contours as well as contours of physical properties of S-CO$_2$ along the receiver tube. The

simulation is repeated 5 times to see the variation in the flow field and heat transfer over a typical day.

The results of this research are expected to help future researchers develop new generation of PTCs suitable for direct S-CO$_2$ Brayton cycles in several ways. Firstly, this research paves the way towards investigating the receiver deformation due to thermal stress which deteriorates the thermal efficiency of PTC and is potential of breaking the glass cover. Distribution of these stresses depend on the distribution of the temperature. The later varies over the time by solar insolation and solar incident angle as well as the convection on the outer surface of the glass cover. Hence, stress analysis of solar collectors which is a key step in designing and developing a new generation of PTC totally relies on the results of heat transfer and flow field analysis.

In addition, this research will build a solid pavement for studying a variety of heat augmentation methods for PTC carrying S-CO$_2$. Such methods are widely used in different applications to enhance the thermal efficiency of systems. However, there is a limited literature on applying heat augmentation methods on receivers of PTCs especially in supercritical condition. The results of this research might also be used in future design applications of PTC. For instance, by changing the gas type and pressure inside the glass annulus designers can decide which gas and pressure yields in less convective heat loss. Or, how different coatings can affect the heat absorption of the receiver at different temperature ranges. Finally, the results can be useful in the operating of a parabolic trough power plant in the sense of predicting the optimum flow rate of the system.

Chapter 2: Theoretical Background

2.1 Thermal Power Cycles

Power cycles are usually categorized in two different ways. From the phase change of working fluid point of view, a power cycle can be either gas or vapor cycle. In a gas cycle the working fluid always remains in super heated phase wheras in vapor cycle the working fluid experiences both the sub cooled liquid phase and super heated phase during each pass. From another point of view, a power cycle can be either closed or open. In closed cycles, after a pass is completed the working fluid returns to its initial thermodynamic state and is recirculated in the system. In contrast, in open cycles after the fluid exits the turbine it is flushed to the ambient and is replaced with fresh fluid. [101, 103]

Usually gas turbines operate on Brayton cycle as illustrated in Fig. 20. In this open cycle, fresh air enters the compressor at ambient conditions. Inside the well-insulated compressor the pressure and consequently the temperature of fresh air increases. Then this high-pressure air is drawn into the combustion chamber and is mixed with the fuel. The mixture is then burnt at constant pressure which elevates its temperature by hundreds of degrees Celsius. The high-temperature and high-pressure gases produced in combustion chamber then enter the gas turbine where they expand to the atmospheric pressure while rotating the rotor of turbine. Compressor blades are installed on one end of the rotor shaft and consume a large portion of energy generated in gas turbine to compress the air while the other end of the rotor shaft is coupled to a generator which converts the rest of mechanical power into electricity. At the end, the exhaust gases are thrown out to the ambient, causing the cycle to be classified as an open cycle.
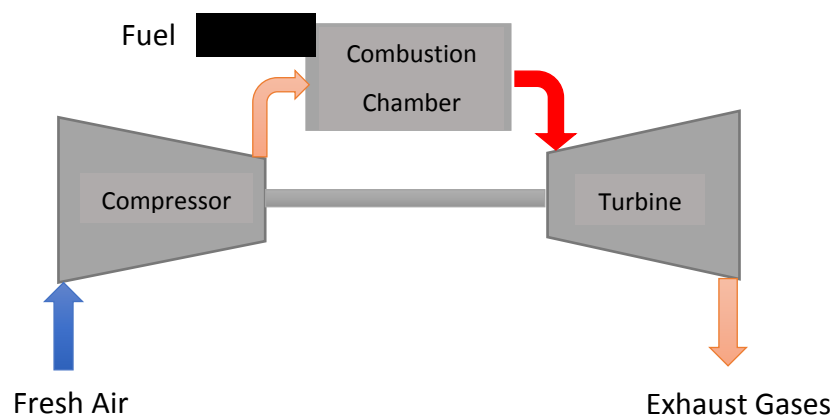
Figure 4 an open-cycle gas turbine

Thermal efficiency of an ideal Brayton cycle can be calculated using following equation.

$$\eta_{th,Brayton} = 1 - \frac{1}{r_p^{(k-1)/k}}$$

Where r_p represents the pressure ratio of the gas turbine and k stands for the specific heat ratio of the working fluid. This simple equation suggests that the efficiency of the Brayton cycle can be enhanced in two main methods. Firstly, the thermal efficiency of the simple Brayton cycle increases with the pressure ratio. Since P_{min} in an open cycle equals the ambient pressure and

(a) T-s diagram
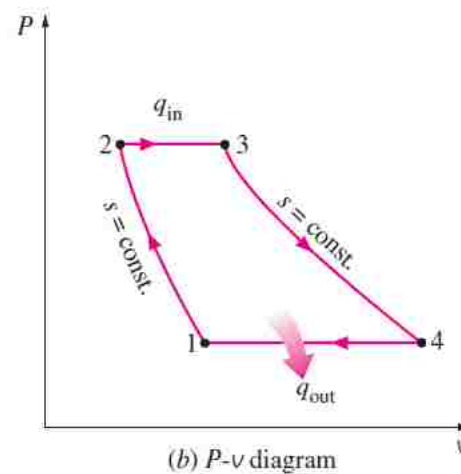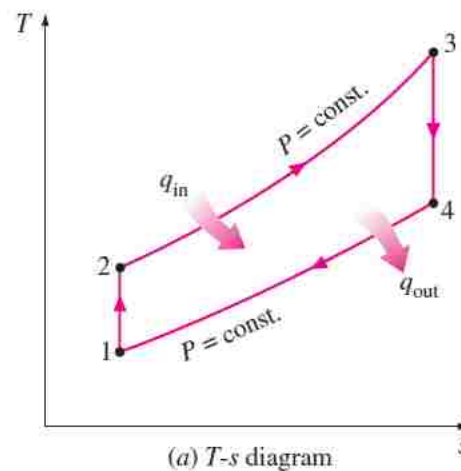
(b) P-v diagram

Figure 5 a) T-s and b) P-v diagrams for the ideal Brayton cycle [101].

is more or less constant, this method practically means to increase the compressor exit pressure. Secondly, the higher the specific heat ratio of the working fluid is the higher the thermal efficiency of the ideal Brayton cycle is. Hence, replacing the working fluid with high specific heat materials improves the thermal efficiency of these power plants. These two methods are applicable to the real gas turbine power plants too. Additionally, the temperature of exhaust gasses of gas turbine engines is censurably higher than the ambient temperature. Hence, the

energy of hot exhaust gases can be used further either to increase the temperature of high-pressure air leaving the compressor in a counter-flow heat exchanger, which is also known as a regenerator, or to boil the water in a steam cycle, combined power cycle. By using a regenerator or combing the gas cycle with a vapor cycle part of the heat loss is recovered which consequently increases the efficiency of the power plant. Several layouts and different techniques are developed and implemented in thermal power plants since the gas turbine power cycles were initially introduced. These methods discussed in details in text books but since they are beyond the scope of this dissertation the author would rather to skip them [4, 101].

Vapor power plants usually work on a closed cycle called Rankine cycle. The ideal Rankine cycle consist of four ideal processes. At first, the sub-cooled working fluid is compressed in an isentropic pump. Then the pressurized fluid is heated in a constant-pressure boiler where the subcooled liquid turns to superheated steam. The high pressure superheated steam then enters the steam turbine where it is expanded isentopically through passing the turbine. Finally, the low-pressure, low-temperature steam leaves the turbine as a high quality mixture and enters the condenser. Constant-pressure heat rejection process in the condenser completes the cycle. The mixture leaves the condenser as a saturated liquid at the condenser pressure which is usually below the atmospheric pressure [103].
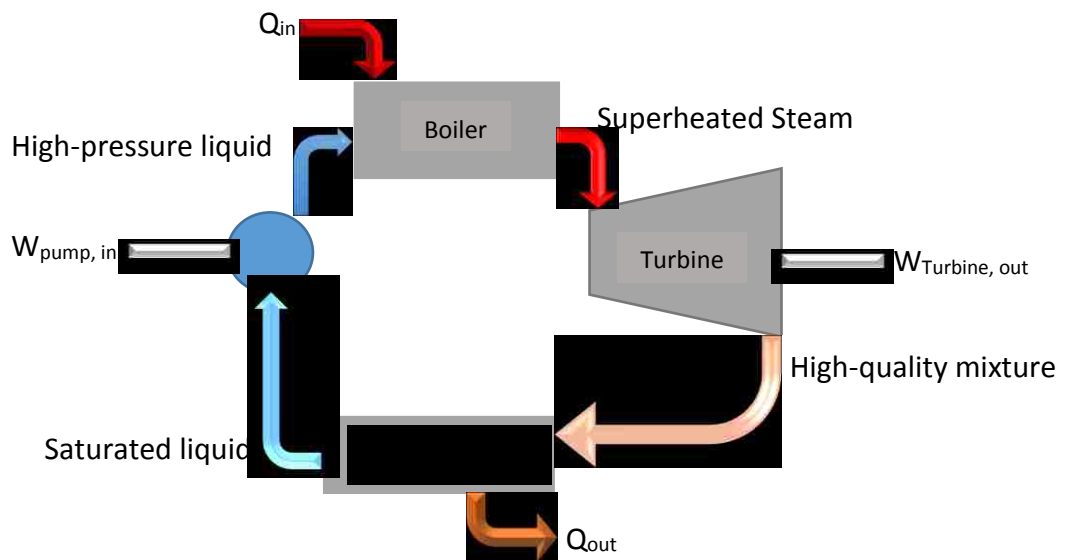
Figure 6 The simple ideal Rankine cycle.

In general three methods are used to enhance the thermal efficiency of steam power plants. First of all, lowering the condenser pressure automatically lowers the temperature at which the heat is rejected to the cold reservoir because the working fluid in condenser experiences a two-

phase process through which the pressure by itself determines all other thermodynamic properties including the temperature. However, lowering the condenser pressure cannot continue forever because the lowest possible pressure in the nature, absolute zero pressure, is only one atmosphere less than the ambient pressure. In fact, the condenser pressure of most vapor power plants is well below the atmospheric pressure but never meet absolute zero pressure.

Secondly, superheating the steam in boiler to higher temperatures increases the temperature at which the heat is transferred to the steam and consequently increases the thermal efficiency of vapor power plant. However, superheating of steam in boiler is applicable only to a limited degree due to safety requirements which does not allow exceeding metallurgically safe values. Lastly, increasing the working pressure of the boiler automatically increases the average temperature at which heat is transferred to the working fluid and consequently enhances the thermal efficiency of steam power plant [103].

In vapor power plants usually, all of these three approaches are applied in combination with reheating and regeneration techniques to increase the thermal efficiency of the power plant as much as possible. Yet, among the main three methods of efficiency enhancement increasing the boiler pressure has finally resulted in developing a new generation of power plants: supercritical thermal power plant [4].

Operating pressures of boilers which was about 2.7 MPa (400 psia) in 1922 have continuously increased over the years to above 30 MPa (4500 psia) today. In fact, nowadays "modern steam power plants operate at supercritical pressures (P_{cr} = 22.06 MPa for water) and have thermal efficiencies of up to 40 percent" [101].
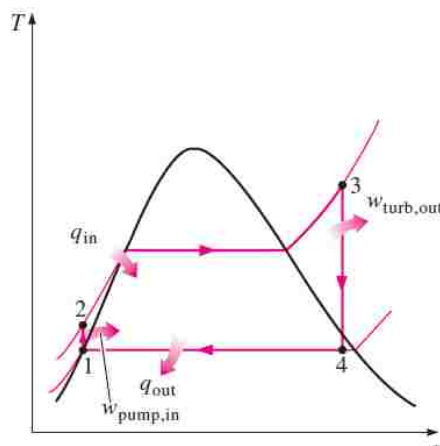
Figure 7 T-s diagram for the simple Rankine cycle. Adapted from [101]

14

An important difference between gas-turbine power plants and steam power plants is their back-work ratio, the ratio of the work consumed to compress the working fluid to the whole mechanical work generated by turbine. While in a gas power cycle usually more than one-half of the turbine work output is used to drive the compressor in steam power plants, where the back-work ratio is only a few percent. This is not surprising, however, since a liquid is compressed in steam power plants instead of a gas, and the steady-flow work is proportional to the specific volume of the working fluid.
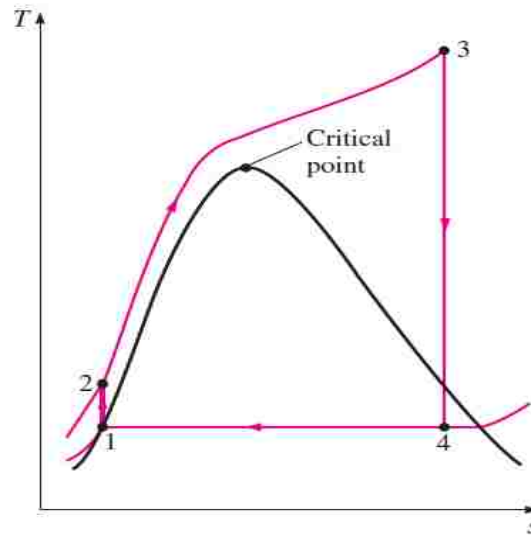
Figure 8 a supercritical Rankine cycle. Adapted from [101]

2.2 Supercritical Power Cycles

In general, thermal efficiency of any power cycle can be defined as the ratio of net work and consumed heat.

$$\eta_{th} = \frac{W_{net}}{Q_H}$$

In a thermal power plant $W_{net} = W_{Turbine} - W_{\frac{Compressor}{Pump}}$ which means the lower the work consumed in compression process is, the higher the thermal efficiency is.

In addition, regarding the second law of thermodynamics the higher the inlet temperature of the turbine the higher achievable thermal efficiency in a thermal power plant. Such a qualitative relationship is reflected in Carnot formula which determines the correlation between the efficiency of a reversible power cycle with the ration of hot and cold reservoirs temperatures [22].

$$\eta_{th,rev} = 1 - \frac{T_L}{T_H}$$

Although the situation is much more complicated in a real case, this simple equation shed a light on another method to increase thermal efficiency of a power cycle. All the efficiency enhancement methods discussed earlier in section 2.2 are actually, different schemes that decrease the reversibilities in power cycle and make it closer to ideal power cycle in the same temperature range. What if we want to increase the efficiency of the ideal cycle itself?

The temperature of cold reservoir T_L is always restricted by the ambient regardless of the cooling system. Hence, the attempts towards increasing the efficiency are mostly focused on either increasing T_H, which technically means to increase the turbine inlet temperature, or decreasing $W_{\frac{Compressor}{Pump}}$. However, in practice sometimes increasing T_H yields in more irreversibility and hence deteriorates the overall thermal efficiency of power plant. Gas turbines for example work in higher temperatures compared to steam turbines. However, thermal efficiency of a typical gas cycle is less than that of a typical Rankine cycle (Figure 24). The reason is that gas turbine utilizes air, compressible fluid, and a large amount of work is consumed for the compression process in compressor. In contrast, Rankin cycle can achieve high efficiency under low turbine inlet temperature conditions because the working fluid is compressed at a liquid state. In other words, liquid water is incompressible and requires less work for compression in boiler feed pumps [19]. The S-CO2 Brayton cycle on the other hand, is the power conversion system which combines the advantages of both a steam Rankine cycle and a gas turbine system. In other words, the fluid is compressed in the incompressible region where compressibility factor of CO_2 is around 0.2 and hence less work is needed to compress the working fluid (figure 25). Then the fluid is heated to the turbine inlet temperatures even higher than those achievable by current gas turbines [19, 17]. Thermodynamically, the main advantage of the Brayton carbon dioxide cycle relies on its high useful to expansion work ratio (i.e. much lower compression work than expansion work) which is in the range 0.7–0.85 when compressor inlet is in supercritical conditions [68].
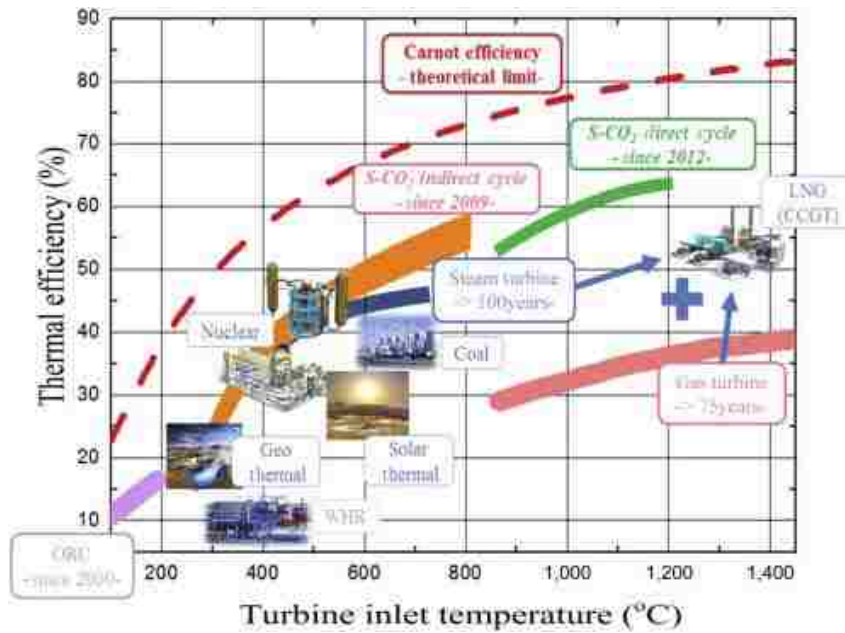
Figure 9 Thermal efficiencies of power conversion systems and applications [19]

Many potential advantages exist for the S-CO$_2$ power cycle and it can be applied to various heat sources. For instance, since the S-CO$_2$ cycle can be considered as an alternative to the steam Rankine cycle, it can be applied to nuclear energy. Besides, the S-CO$_2$ power cycle can be utilized as a topping cycle for fossil fuel powered plants, coal fired power plants for instance, and a bottoming cycle of gas combined cycle plants. There are also promising heat sources soon to be developed, which include several renewable energy sources such as high temperature fuel cells, concentrated solar power, and geothermal power. S-CO$_2$ power cycle is also suggested to be utilized and commercialized for the exhaust/waste heat recovery application especially from a small gas turbine, where using a steam Rankine cycle is not practically feasible [41].
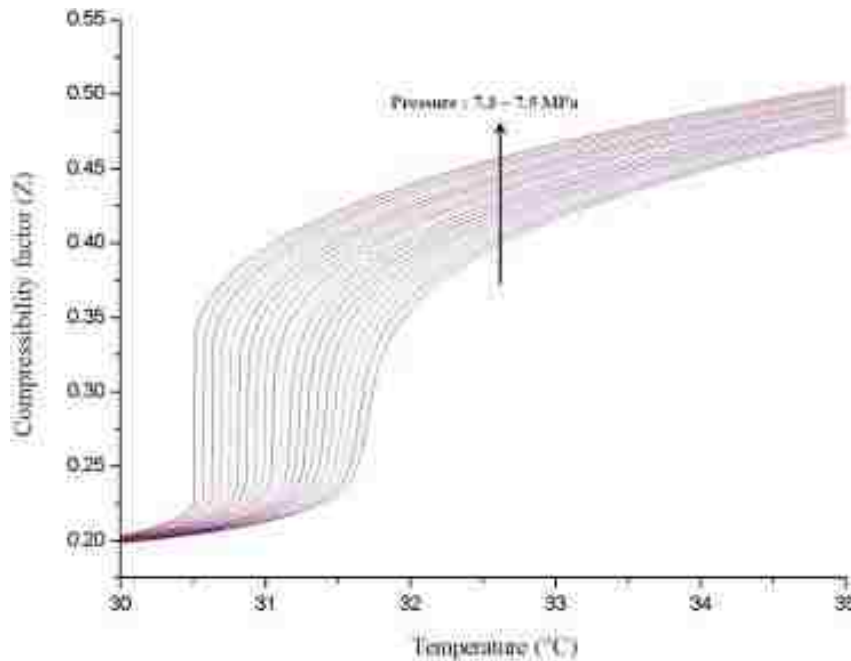
Figure 10 Compressibility factor of S-CO2 near the critical point [19].

In brief, the benefits of the S-CO$_2$ cycle can be summarized as follows [19].

1. The thermal efficiency can be increased up to 5% compared with the steam Rankine cycle.

2. The turbomachinery can be much smaller and the overall system size can be reduced up to four times compared with the conventional steam Rankine cycle (figure 26).

3. The competitiveness of S-CO$_2$ dry cooled systems over wet cooled systems is steel a controversial issue. Yet, the potential of the air-cooled S-CO$_2$ cycle can grow as the system design becomes more sophisticated and the component level technology becomes more advanced.

4. As the minimum pressure is higher than the CO$_2$ critical pressure (7.38 MPa), the purification system requirements are lower than those of the steam Rankine cycle to prevent air ingress. Thus, the power conversion system can be much simpler. In the steam cycle case, the low pressure in the condenser causes gas ingression and complex purification systems are required.

5. Among various fluids, CO$_2$ is relatively cheaper and less harmful when an appropriate ventilation system is installed to prepare for a sudden large release of CO$_2$ from the power conversion system.
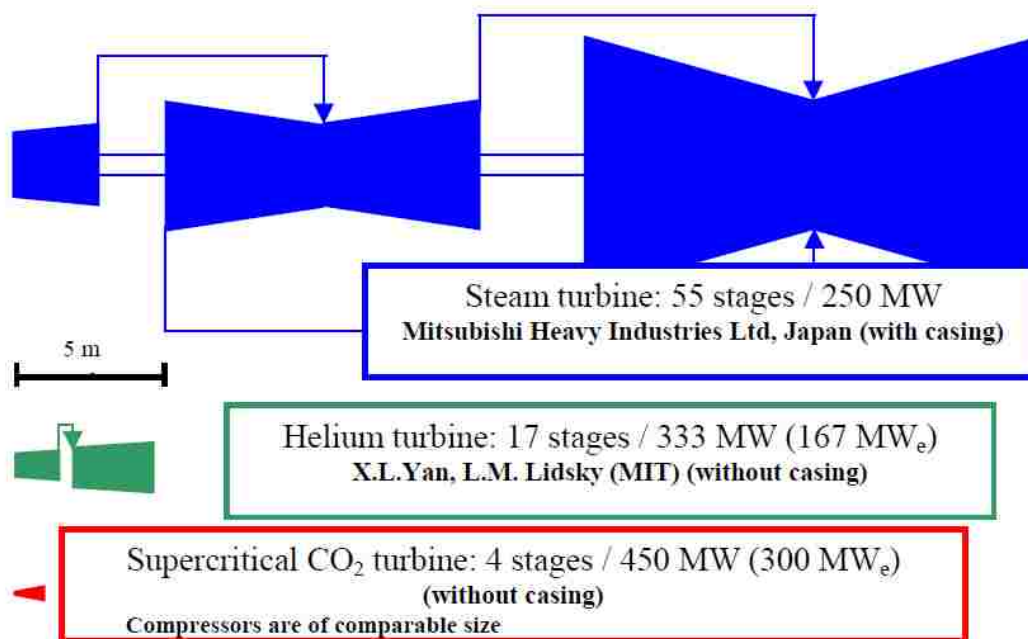
Figure 11 Comparison of Turbine sizes [15]

Although several layouts of S-CO$_2$ cycle are suggested and analyzed in previous researches [28, 29, 30, and 31], there is a limited literature about classifying S-CO$_2$ cycles [19]. In general, S-CO$_2$ cycles are modifications of closed Brayton cycle in super critical/transcritical region. The cycles can be categorized depending on whether the working flow is split or not. Ahn, Y. et al (2015) have classified different S-CO$_2$ closed Brayton cycles under twelve groups (figures 27 and 28). Despite the differences between these layouts solar resource has the same position in all of them. In fact, in CSP applications of S-CO$_2$ cycles solar collectors are utilized as the heater of the system. For instance, Sandia National Laboratories test loop is a split-flow recompression Brayton cycle. A schematic of this layout is illustrated in figure 29 where solar resource is modeled by a heater.

a)

Recuperation   Intercooling   Reheating

Interrecuperation   Precompression   Splitexpansion

b)

Recompression   Modified recompression   Preheating

Turbine split flow 1   Turbine split flow 2   Turbine split flow 3
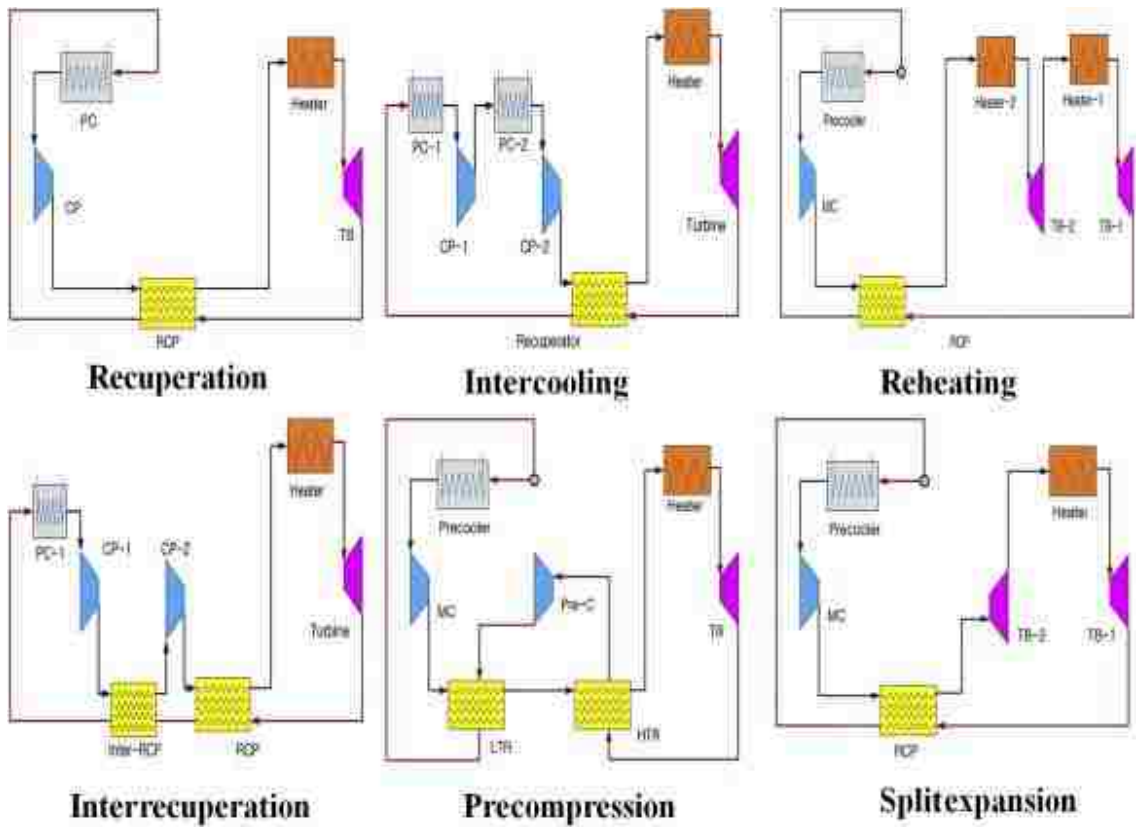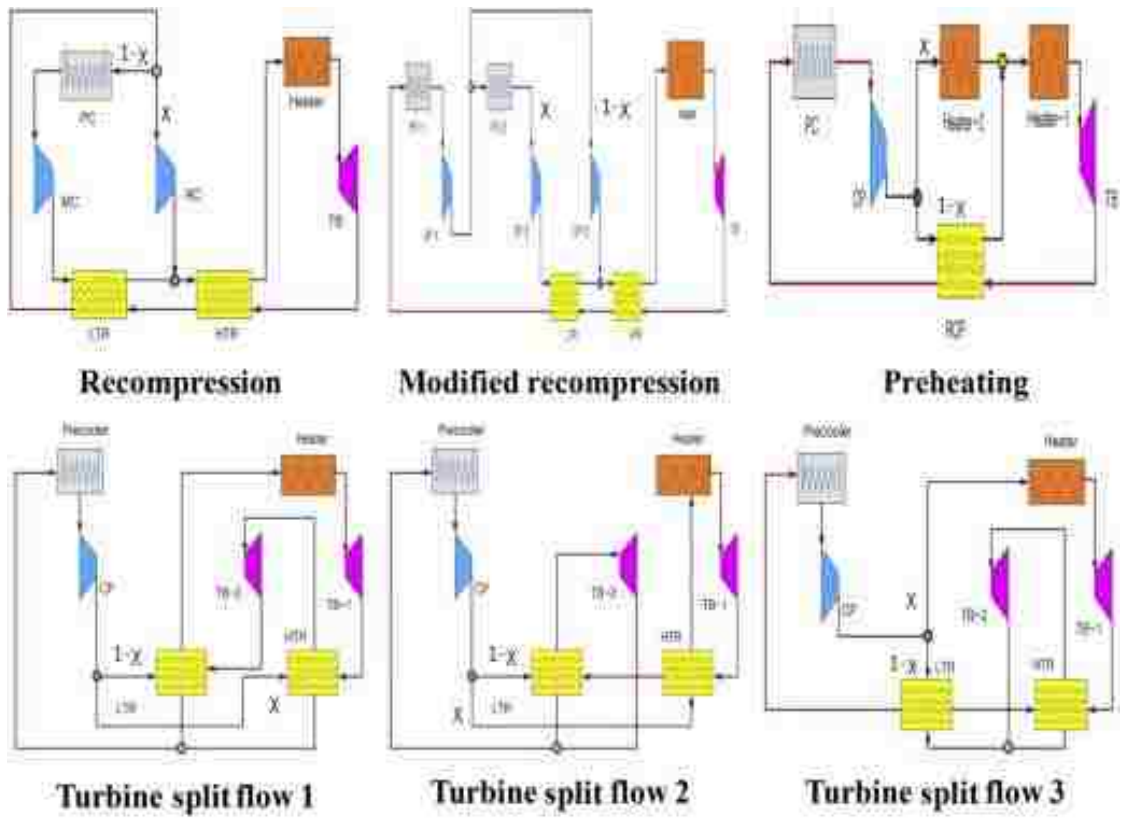
Figure 12 S-CO2 cycle a) single flow layouts b) split flow layouts [19]

20
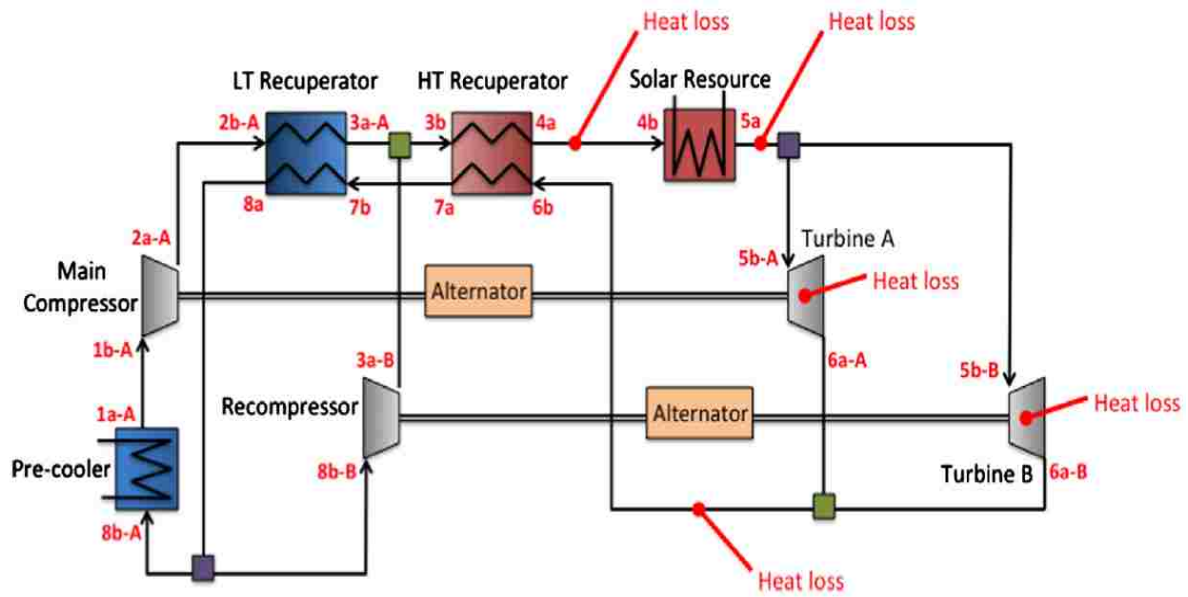
Figure 13 Layout of split-flow recompression Brayton cycle components [30]

Thermodynamic state points of this cycle are shown in figure 29. Phase change from critical to supercritical state occurs in the main compressor (process 1-2) by increasing the pressure from around 7.6 MPa to above 10 MPa. Then in two consecutive recuperators S-CO$_2$ absorbs heat from turbine exhaust (process 2-3 and 3-4) and its temperature increases from about 40 ^{0}C to about 350 ^{0}C. After this point the fluid enters solar collectors to absorb more heat and leaves the solar collectors with temperature at 400 ^{0}C (process 4-5). This high temperature S-CO$_2$ enters the turbine/turbines where due to expansion its pressure decreases to 7.6 MPa while its temperature decreases only about 20 ^{0}C. In return, the turbine generates mechanical work (process 5-6). The exhaust of turbine/turbines is a hot gas containing enormous amount of heat. So, in order to reduce heat loss, the exhaust gas is conducted to recuperators to exchange its heat with cold S-CO$_2$ that leaves the compressor (process 6-7 and 7-8). Finally, to remove further heat from the flow and bring it around the critical point of CO$_2$ a pre-cooler is used (process 8-1) which completes the cycle. To measure the efficiency of such a cycle one should analyze the whole components. However, the scope of this research is restricted to the solar receivers. So, in this research only a part of the heating process (process 4-5) is modeled and analyzed. Hence, it is impossible to prove that the thermal efficiency increases solely on the results of this research. Last but not least, following graphs qualitatively demonstrate some of the most important boundary conditions of the solar collectors set. Firstly, the inlet pressure of the solar collectors should be considerably more than critical pressure of CO$_2$ (usually above 10 MPa). Secondly, the inlet temperature of solar collectors should be a way higher than the critical temperature of CO$_2$.

21
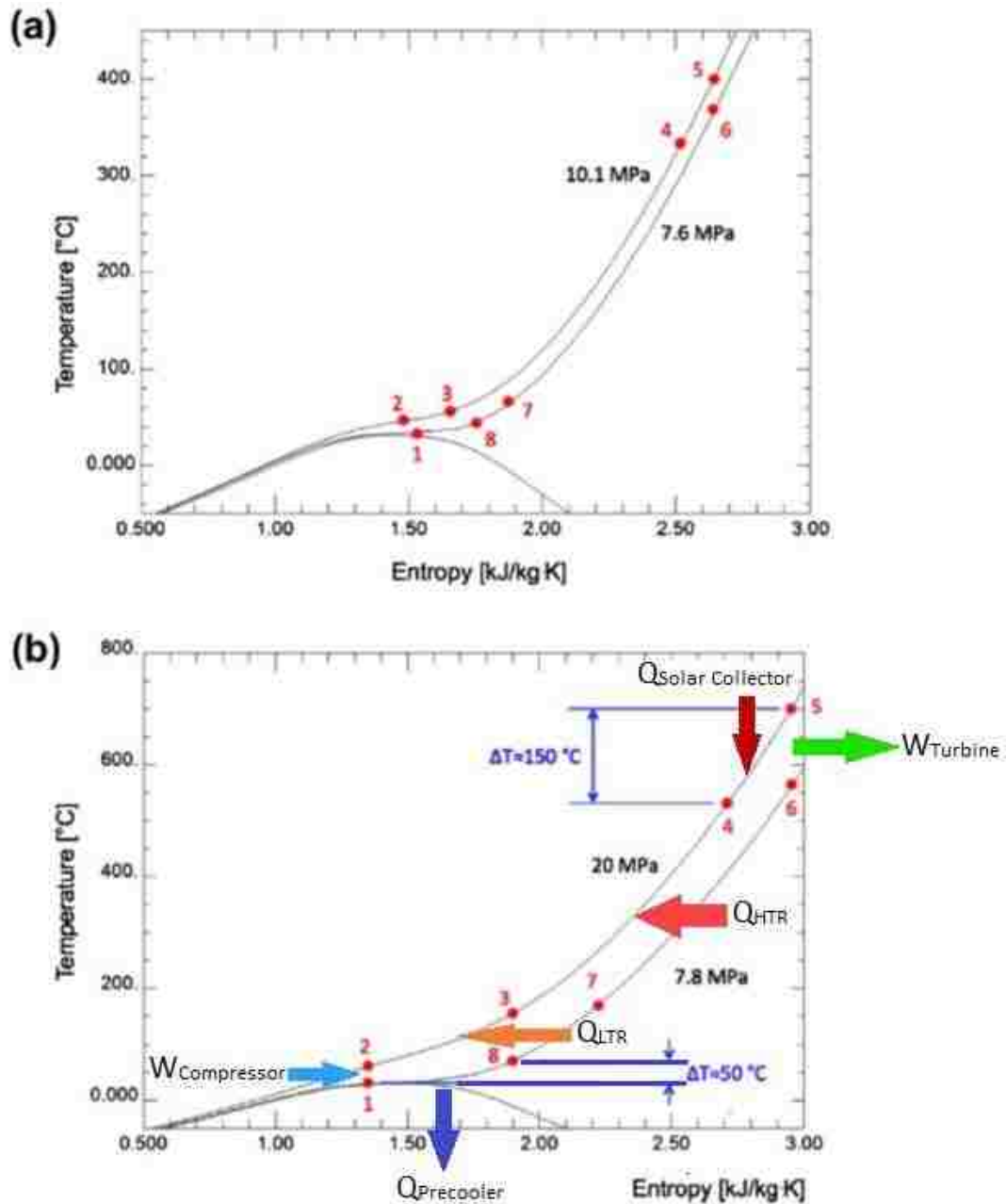
Figure 14 a) Typical current system operating conditions at Sandia National Laboratories and b) projected system operation by Dostal et al [15, 30]

2.3 Supercritical Carbon Dioxide (S-CO₂)

CO_2 is a non-flammable, non-toxic natural refrigerant with no Ozone Depletion Potential (ODP) and a negligible Global Warming Potential (GWP). Its critical temperature is 31.1 ^0C compared to 373.9 ^0C of water and considerably less than all other common alternative choices. Such a low critical temperature makes CO_2 a good candidate for heat absorption when it comes

to low degree applications [14]. The critical pressure of CO_2 is 7.38 MPa which is about three times less than that of water. The fluid becomes more incompressible near the critical point. For CO_2 near the critical point, the compressibility factor decreases by 0.2–0.5 as shown in figure 5 and the compression work can be substantially decreased [19]. In higher temperatures where material degradation due to high temperature and pressure operating conditions is a serious issue S-CO_2 shows better performance compared to other candidates including ultra-supercritical steam. Hence, it increases safety and reliability. In addition, as S-CO_2 is less corrosive compared with steam at the same temperature, the S-CO_2 cycle can potentially increase the turbine inlet temperature [20] and [21]. Moreover, CO_2 is abundant in the nature and comes in a low price. Table 2 compares the characteristics and properties of CO_2 with water and five common refrigerants [13]. Appendix B contains some of the characteristics of a number of refrigerants including CO_2.

Figure 6 demonstrates the phase diagram of CO_2 around its critical point above where saturation line disappears. This means that beyond critical point phase change from compressed fluid to superheated fluid occurs continuously without any distinguishable two-phase region. Photos d to g of figure 7 illustrate such a transition. In contrast with subcritical fluids (photos *a* and *b* from figure 7), during the phase change process of supercritical fluid liquid phase cannot be distinguished from the gas phase by any distinguishable interface. Hence, the validity of any numerical simulation of supercritical phase change which is based on two phase flow schemes is questionable. Yet sharp changes in the physical properties of the fluids around critical or pseudo-critical point add more sophistications to the numerical analysis.

Figure 8 shows that while the variation of physical properties of S-CO_2 at 7.58 MPa is almost linear both before 25 ^{0}C and after 40 ^{0}C, their behavior is extremely nonlinear between these two temperatures. For instance, a single degree centigrade increment in the temperature (from 32 ^{0}C to 33 ^{0}C) yields in about 30 % decrease in the density. Such a temperature gradient is expectable not only inside the pre-cooler of a S-CO_2 Brayton cycle, but also in the main compressor. Recuperators increase the temperature of S-CO_2 as high as $300 - 450$ ^{0}C before it enters the solar collectors which guarantees that the fluid does not experience sharp transcritical variations in its physical properties [15, 30].
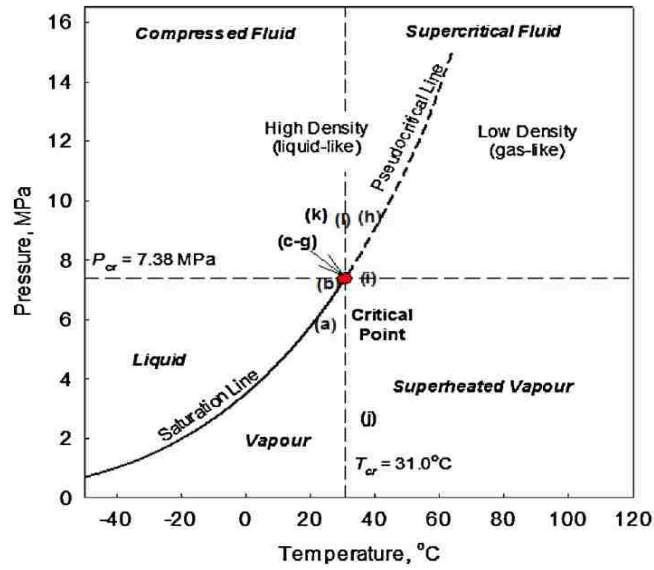
Figure 15 Phase Diagram of CO2. Extracted from [12]

Temp: 25.8 C;
Pressure: 5.54 MPa

Temp: 30.1 C;
Pressure: 7.23 MPa

Temp: 30.8 C;
Pressure: 7.32 MPa

Temp: 31.0 C;
Pressure: 7.39 MPa

Temp: 31.0 C;
Pressure: 7.41 MPa

Temp: 31.0 C;
Pressure: 7.39 MPa

Temp: 31.3 C;
Pressure: 7.41 MPa

Temp: 38.3 C;
Pressure: 9.32 MPa

Temp: 38.1 C;
Pressure: 7.30 MPa
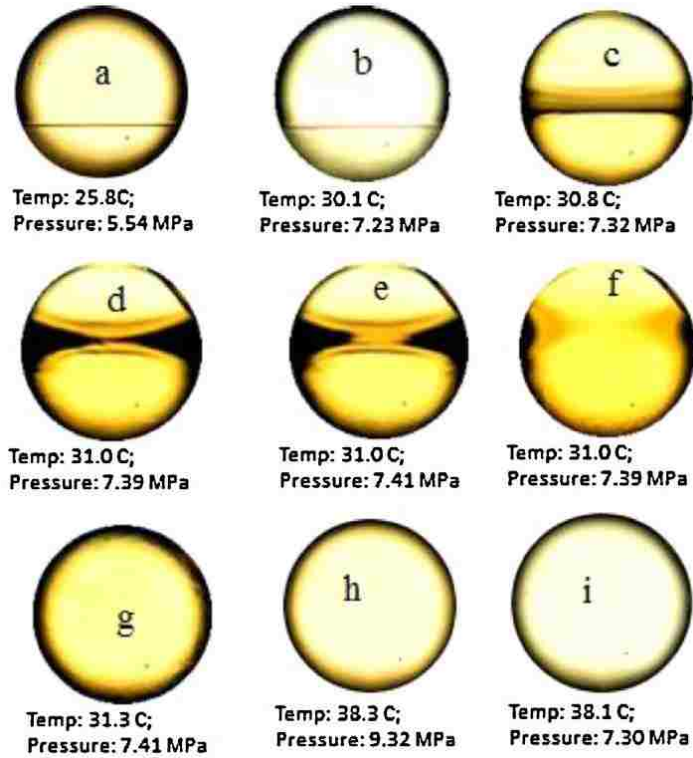
Figure 16 Transition of CO2 through various phases (a) sub-critical; (b)–(g) transition through critical point; (h) supercritical fluid; (i) between supercritical fluid and superheated vapor [12].

24
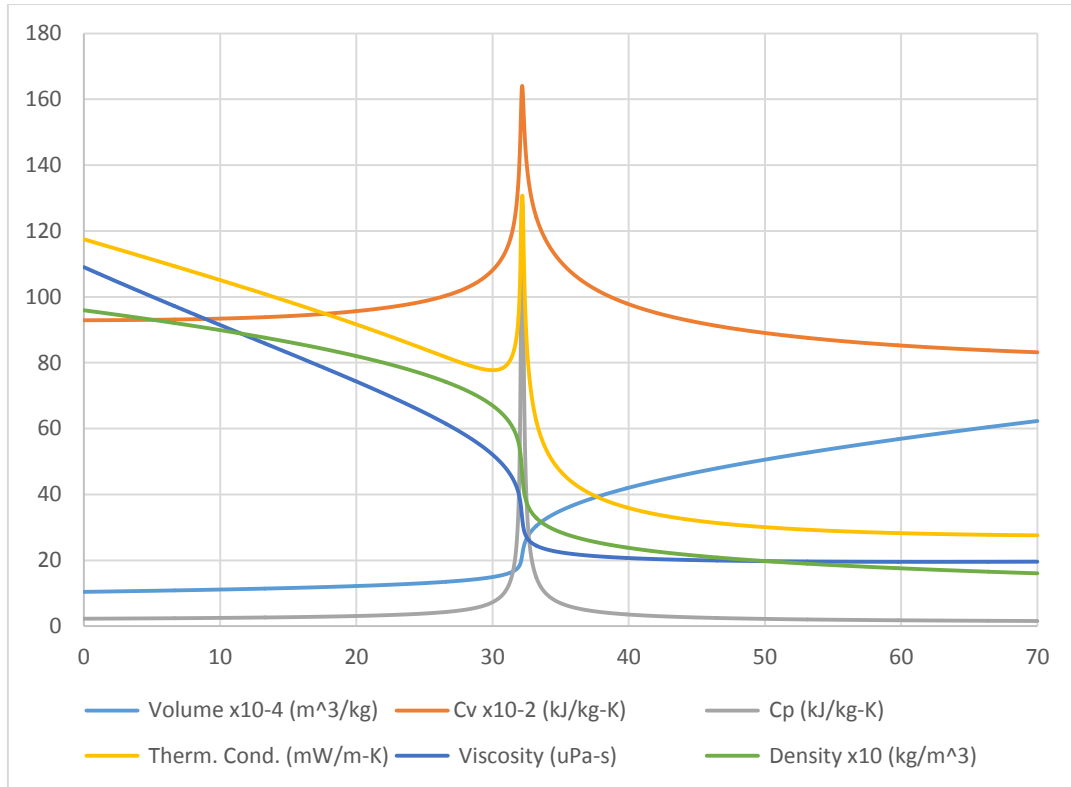
Figure 17 CO2 properties near pseudo-critical temperature at 7.58 MPa [81]

However, significant temperature gradients exist across the PTC receiver [8, 23] which results in considerable variations in density (Figure 55). Hence, the buoyant forces should be considered. In brief, a considerable potential of natural convection exists in the receiver because of significant temperature gradients that yield in considerable density variations.

2.4 Computational Modeling of S-CO$_2$

To define the thermodynamic state of a super critical gas a pair of independent intensive properties should be known. Since measuring the temperature and pressure are easier than other intensive thermodynamic properties, these two properties are widely used as the controlling properties in thermal power plants. However, defining a specific property as a function of two independent variables, temperature and pressure in this case, is a quite challenging task. Thermodynamic state equations developed by researchers in last two centuries are more sophisticated and less accurate in supercritical region compared to other regions in Pv diagram [22]. Therefore, to predict the thermodynamic properties of S-CO$_2$, knowing its temperature and pressure, one should either use tabulated data or reduce it to a single variable function.

Regarding the CPU requirements and memory restrictions in using tabulated data, in this research the second method is used.

Figure 33 illustrates the effect of pressure on specific heat capacity of carbon dioxide around its critical point. Visibly, change in pressure around the critical point strongly affect the physical properties. However, the situation in a PTC is a way far from pseudo critical region due to significantly higher temperature.
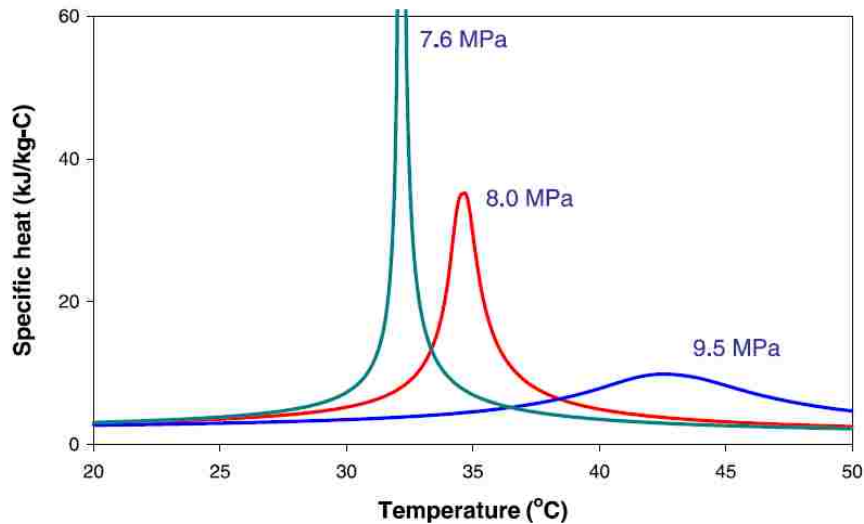
Figure 18 Pressure effect on the near-critical properties of CO2 [9, 81]

As stated earlier in a solar power plant S-CO2 enters the receiver at 300 ^{0}C and 10 MPa or higher. To see a significant difference in the physical properties of S-CO2 in such a state, the pressure variation should be of the order of an atmosphere. In practice however, neither the pressure loss along the 8-meter length receiver nor the pressure gradients across the 66 mm diameter receiver are large enough to cause considerable variations in the physical properties of S-CO_2. Indeed, the largest pressure gradients inside a PTC are of the order of kPa. On the other hand, both the temperature gradients across the receiver and temperature increment along it are large enough to cause significant changes in the thermal properties of S-CO_2. Figures 34 and 35 demonstrate the percentage of variation in thermodynamic properties of S-CO_2 at P = 10 MPa and 300 ^{0}C respectively. All Properties are scaled by dividing to the corresponding property at T = 300 ^{0}C and P = 10 MPa respectively. Comparing these two graphs show that the variation of thermodynamic properties of S-CO_2 inside the receiver due to pressure gradients is up to two orders of magnitude less than the variation due to temperature gradients.

In conclusion, the properties of CO_2 in working conditions of a PTC are a strong function of the temperature and a weak function of the pressure. Hence, it is reasonable to assume that the

physical properties of S-CO$_2$ inside the receiver tube are only a function of temperature at the inlet pressure of PTC.
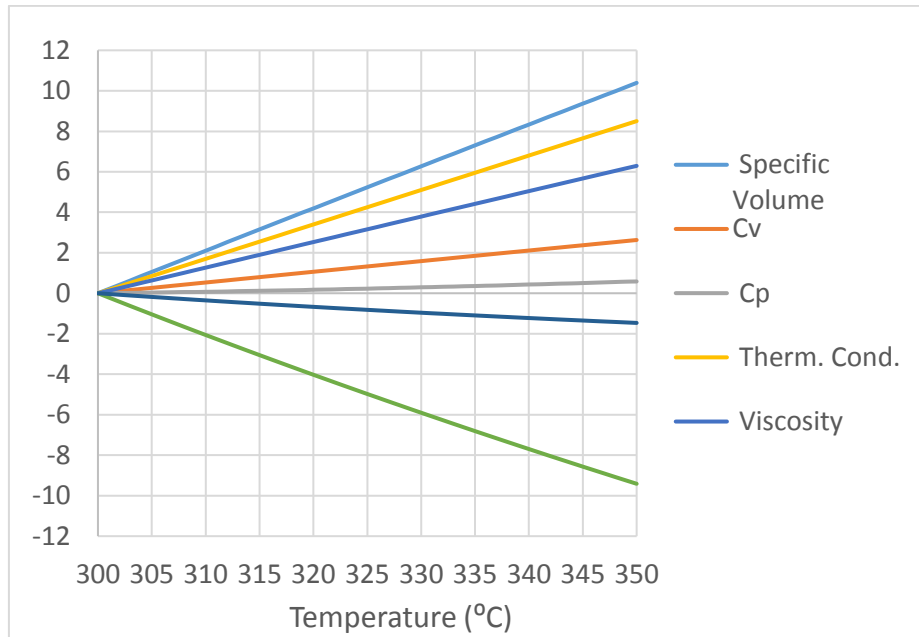
Figure 19 Percentage of Variation in Thermal Properties of S-CO2 at P = 10 MPa [81]
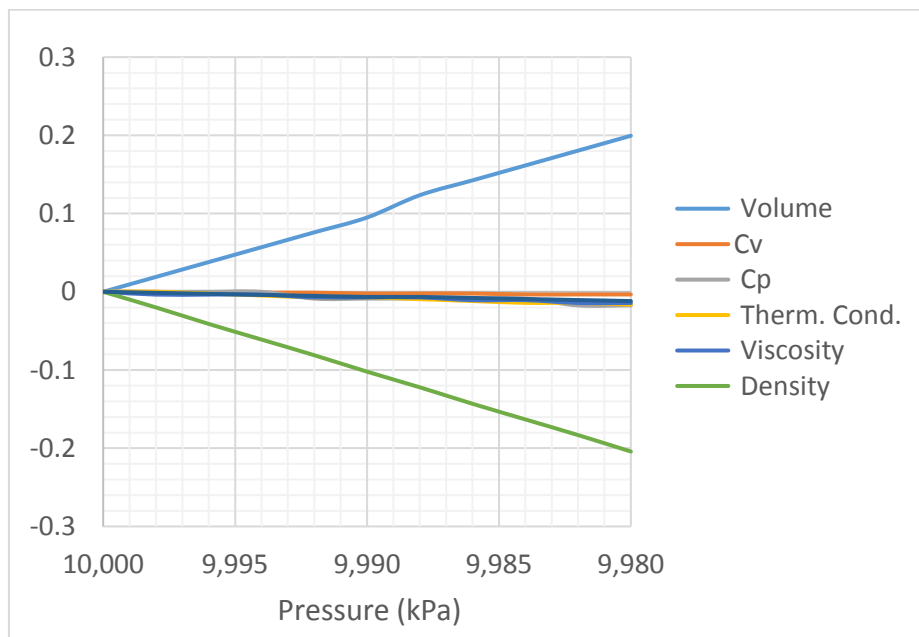
Figure 20 Percentage of Variation in Thermal Properties of S-CO2 at T = 300 ^{0}C [81]

In this research, it is assumed that S-CO$_2$ enters the receiver tube at 10 MPa and 300 ^{0}C. Therefore, REFPROP software from National Institute of Standards and Technology [81] is used to generate isobaric correlations at P = 10 MPa to predict the thermodynamic properties of carbon dioxide at each point inside the receiver. Appendix C contains graphs that illustrate these data.

2.5 Solar Radiation

Detailed information about the solar irradiation at any location is necessary for design of solar power plant. Long term data of solar irradiation are measured and collected in large number of stations across the United States. For the rest of locations data measured by satellites can be used to estimate the available solar irradiance at any particular time.

The average amount of solar radiation falling on a surface normal to the rays of the sun outside the atmosphere of the earth, extraterrestrial insolation, at mean earth-sun distance D_o is called the solar constant, I_o. There is a vast literature on measuring solar constant [97]. Several measurements suggest that solar constant is 1366.1 W/m^2 [84, 95]. However, neither the extraterrestrial insolation is constant nor it is a good estimation of the solar insolation received on the ground. Moreover, it doesn't reveal anything about the angle of solar incident at a specific location in a particular time. In this section the basics of a mathematical model to estimate the solar angles and solar incident on the parabolic trough collector is described in brief. Detailed discussion on about this method can be found in text books.
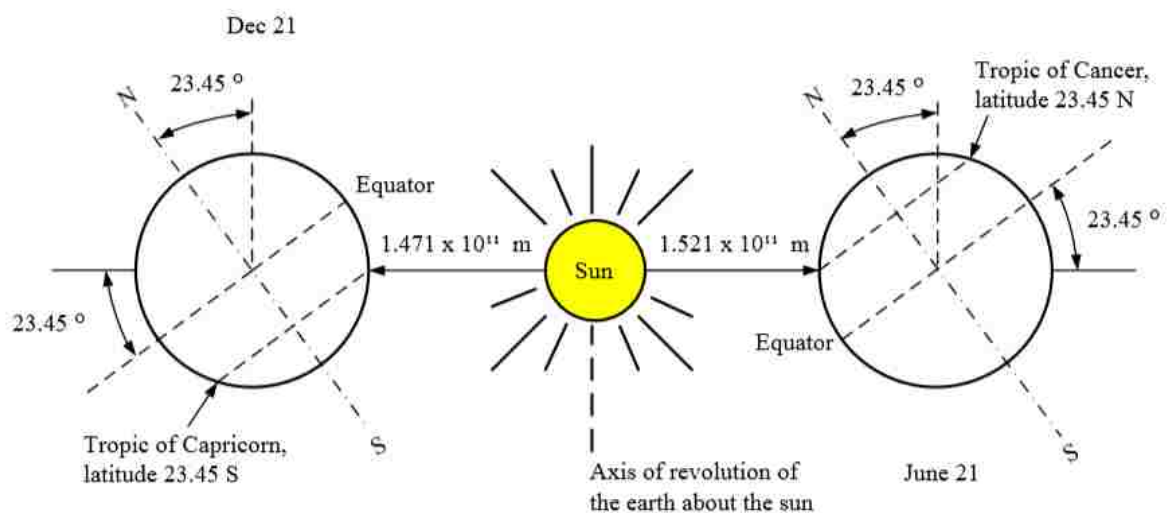
Figure 21 Motion of the Earth around the Sun [85]

Direction of Beam Radiation

The angle between the earth-sun line (through their center) and the plane through the equator is called the solar declination angle, δ_S (Figure 5).
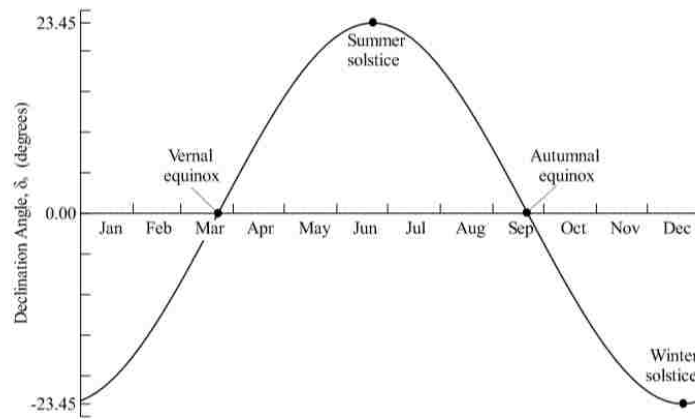
Figure 22 Variation of declination angle, throughout of the year

The declination angle varies between -23.45^0 on December 21 to +23.45^0 on June 21. The solar declination is given by:

$$\delta_S = 23.45^\circ \ \sin\left[\frac{360(284+n)}{365}\right]$$

where n is the day number with January 1 being n = 1. The position of the sun can be described at any time by two angles, the altitude and the azimuth angle (Figure 6). The solar altitude angle, α, is the angle between a line collinear with the sun rays and the horizontal plane [92]. The solar azimuth angle, a_s, is the angle between a due south line and the horizontal projection of the line joining the site to the sun [92]. The solar zenith angle, θ_z, is the angle between the site to sun line and the vertical at the site location:

$$\theta_z = 90 - \alpha$$

The solar altitude angle and azimuth angles are not fundamental; hence, they must be related to the fundamental angles (Figure 7): hour angle (h_s), latitude (L) and declination angle (δ_S).
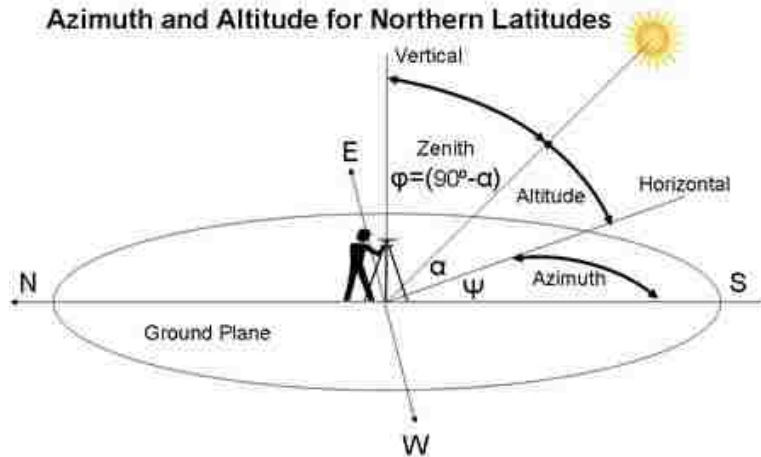
Figure 23 Earth surface coordinate system for observer at Q showing the solar azimuth angle, the solar altitude angle and solar zenith angle for central sun ray along direction vector. Also, shown unit vectors along their respective axes. Adapted from [93]

The solar hour angle is given by:

$$\omega = (t_s - 12) \times 15°$$

It should be noticed that the time used in solar analysis is the local standard time so before calculating the hour angle ω it is necessary to convert the recorded time to the solar time

$$t_s = t + E + (L_{st} - L_{loc}) \times 4 \frac{\text{min}}{\text{degree}}$$

where t_s is the solar time in hours, t denotes the local time, L_{st} is the standard meridian for the local time zone, and L_{loc} is the longitude of the location.
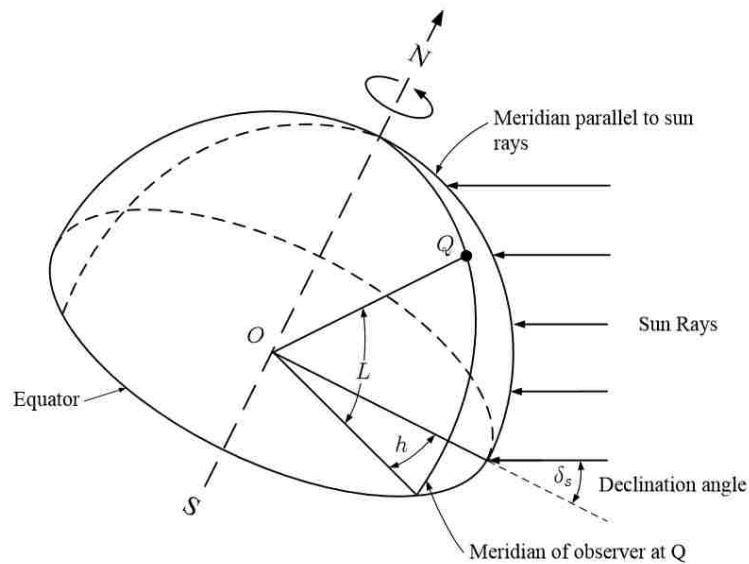
Figure 24 Fundamental sun angles: hour angle h, latitude L and declination, Adapted from [93]

E is the equation of time (Figure 8), which accounts for the variation of the rotational speed of the earth. An approximation for calculating the equation of time, E, in minutes is given by

Spencer [98] as cited by Iqbal [97] and is accurate to within about 30 seconds during daylight hours:

$$E = 229.2(0.000075 + 0.001868 \cos B - 0.032077 \sin B - 0.014615 \cos 2B - 0.04089 \sin 2B)$$

Where B is given by:

$$B = (n - 1)\frac{360}{365}$$

The latitude angle φ (Figure 7) is the angle between the line from the center of the earth to site and the equatorial plane. The latitude is considered positive north of the equator and negative south of the equator. Expression for solar altitude and solar azimuth may be defined in terms of latitude (φ), hour angle (ω), and declination angle (δ_S).

solar altitude angle: $\qquad \alpha = \sin^{-1}(\cos \delta_S \cos \phi \cos \omega + \sin \delta_S \sin \phi)$

solar azimuth angle: $\quad \gamma_s = sign(\omega) \times \left| \cos^{-1} \left(\frac{\cos \delta_S \sin \phi \cos \omega - \sin \delta_S \cos \phi}{\cos \alpha} \right) \right|$
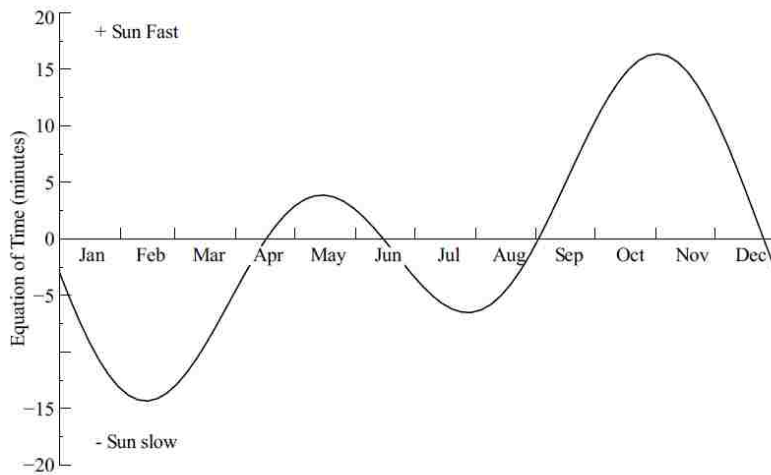
Figure 25 Equation of time EOT

The solar azimuth angle can be in any of the four trigonometric quadrants depending on the location, time of day, and the season [93].

Solar Incidence Angles on a Single Axis Tracking Collector

Parabolic Trough Solar Collectors track the sun by rotating around only one axis to minimize the angle of incidence of beam radiation on their surfaces and thus maximize the incident beam

radiation. A tracking drive system rotates the collector about an axis of rotation until the sun central ray and the aperture normal area are coplanar. Figure 26 shows how the rotation of a collector aperture about a tracking axis, r, brings the central ray unit vector S into the plane formed by the aperture normal and the tracking axis. Rotation axis can have any orientation but in practice is usually horizontal east-west, horizontal north-south, vertical, or parallel to the earth's axis. Table 2 summarizes the formula to compute the angle of incidence for different tracking modes [7].
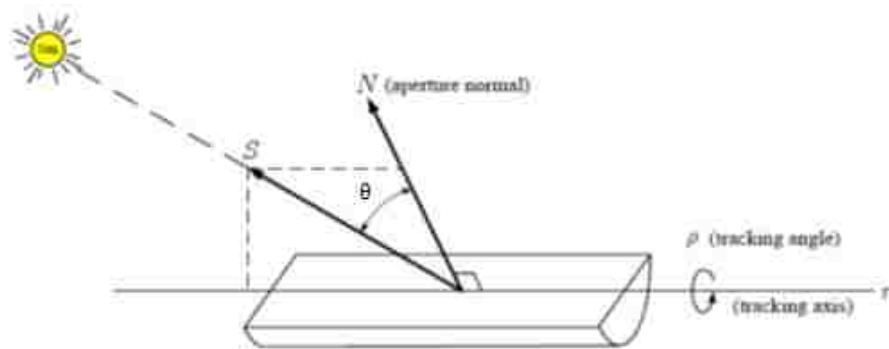
Figure 26 a single-axis tracking aperture. Adapted from [93]

Tracking mode	Angle of Incidence	Slope	Surface azimuth angle
Horizontal North–South with continuous adjustment	$Cos\,\theta = (cos^2\theta_z + cos^2\delta.sin^2\omega)^{\frac{1}{2}}$	$\tan\beta = \tan\theta_z\,\lvert\cos(\gamma-\gamma_s)\rvert$	$\gamma = \begin{cases} 90^{\circ} & if\ \gamma_s > 0 \\ -90^{\circ} & if\ \gamma_s \le 0 \end{cases}$
Horizontal East–West with continuous adjustment	$Cos\,\theta = (1 - cos^2\delta.sin^2\omega)^{\frac{1}{2}}$	$\tan\beta = \tan\theta_z\,\lvert\cos\gamma_s\rvert$	$\gamma = \begin{cases} 0^{\circ} & if\ \lvert\gamma_s\rvert < 90 \\ 180^{\circ} & if\ \lvert\gamma_s\rvert \ge 90 \end{cases}$
Horizontal East–West with a single daily adjustment	$Cos\theta = sin^2\delta + cos^2\delta.\cos\omega$	$\beta = \lvert\phi - \delta\rvert$	$\gamma = \begin{cases} 0^{\circ} & if\ \phi - \delta > 0 \\ 180^{\circ} & if\ \phi - \delta \le 0 \end{cases}$
Horizontal North–South parallel to the earth's axis with continuous adjustment	$Cos\ \theta\ =\ Cos\,\delta$	$\tan\beta = \dfrac{\tan\phi}{\cos\gamma}$	$\gamma = \tan^{-1}\dfrac{\sin\theta_z\ \sin\gamma_s}{\cos\theta'\ \sin\phi} + 180\ C_1C_2$ Where θ', C_1, and C_2 are defined as following
Vertical axis tracking with collector's fixed slope	$Cos\ \theta\ =\ \cos\theta_z\cos\beta + \sin\theta_z\sin\beta$	$\beta = Constant$	$\gamma = \gamma_s$
Two axes tracking mode	$Cos\,\theta = 1$	$\beta = \theta_z$	$\gamma = \gamma_s$

Table 2 Angle of incidence for six different tracking systems of collector

In calculating the surface azimuth angle for horizontal North–South collector parallel to the earth's axis with continuous adjustment:

$$Cos\ \theta' = cos\theta_z\ cos\phi + sin\theta_z\ sin\phi\ cos\gamma_s$$

$$C_1 = \begin{cases} 0 & if & \left(\tan^{-1}\dfrac{\sin\theta_z\ \sin\gamma_s}{\cos\theta'\ \sin\phi}\right)\gamma_s \geq 0 \\ & +1\ otherwise \end{cases}$$

$$C_2 = \begin{cases} +1 & if & \gamma_s \geq 0 \\ -1 & if & \gamma_s < 0 \end{cases}$$

Solar Radiation Data

Experimentally measured solar radiation data are available in several forms. Most radiation data available are for horizontal surfaces, including both direct and diffuse Radiation. Several solar radiation datasets are available with different formats and containing data collected in various locations. Some of these datasets are global while the others focus on a particular region on the globe. Typical Meteorological Year (TMY) data set is widely known as the best solar radiation dataset in the USA. TMY provides designers and other users with a reasonably sized annual data set that holds hourly meteorological values that typify conditions at a specific location over a longer period, such as 30 years. The latest revision of TMY datasets, TMY3s are data sets of hourly values of solar radiation and meteorological elements for a 1-year period. Their intended use is for computer simulations of solar energy conversion systems and building systems to facilitate performance comparisons of different system types, configurations, and locations in the United States and its territories. Because TMYs represent typical rather than extreme conditions, they are not suited for designing systems to meet the worst-case conditions occurring at a location. TMY3 contains data collected by measuring the solar radiation either on a horizontal surface or on a surface which tracks the sun so that the solar beams are always normal to the tracking surface. In this research TMY3 dataset of Albuquerque, NM is used to estimate the beam and diffuse solar irradiance as well as altitude and azimuth angle of sun in June 11th. In addition, the ambient temperature, dew point temperature, and wind velocity are also taken from TMY3 tables.

Estimating Hourly Available Solar Radiation

Sun can be roughly modeled as a blackbody emitting at temperature of 5777 K. However, due to its complicated physical structure, and its temperature and density gradients the sun does not, in fact, function as a blackbody radiator at a fixed temperature. Rather, the emitted solar radiation is the composite result of the several layers that emit and absorb radiation of various wavelengths. The resulting extraterrestrial solar radiation and its spectral distribution are measured by various methods in several experiments.

Although for engineering purposes, in view of the uncertainties and variability of atmospheric transmission, the energy emitted by the sun can be considered constant, in fact extraterrestrial radiation is not constant. The extraterrestrial radiation varies by the inverse distance square from the earth to the sun as:

$$S_{on} = S_{sc} \left(\frac{D_0}{D}\right)^2$$

where D is the distance between the sun and the earth, and D_0 is the yearly mean earth-sun distance (1.496×10^{11} m). The factor $(D_0/D)^2$ is calculated as [94]:

$$\left(\frac{D_0}{D}\right)^2 = 1.000110 + 0.034221 \cos B + 0.001280 \sin B + 0.000719 \cos 2B + 0.000077 \sin 2B$$

Estimating the solar irradiance on the ground using the extraterrestrial radiation is quite a difficult and inaccurate task. The reason is that as extraterrestrial solar radiation, I, passes through the atmosphere, a part of it is reflected back into the space, a part is absorbed by the air and water vapor, and some gets scattered by the molecules of air, water vapor, aerosols and dust particles (Figure 27) [94]. In addition, the composition of atmospheric gases at each specific location is not constant. Rather, it varies over the time for instance due to the existence of clouds. Consequently, solar radiation spectrum on the ground changes over the time. Figure 14 shows the extraterrestrial solar radiation spectrum, with the solar constant of 1366.1 W/m2, with the equivalent black body (normalized) curve and the atmosphere attenuated spectrum for air mass of 1.5.
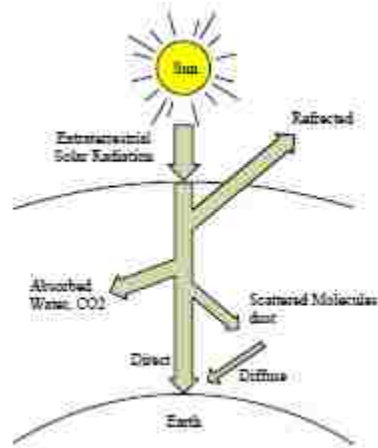
The part of solar radiation that reaches the surface of the earth with essentially no change in direction is called direct or beam radiation. The scattered diffuse radiation reaching the surface from the sky is called sky diffuse radiation. Measuring these two components of solar irradiance is not easy. However, one can easily measure the total (Global) Irradiance, I, on a horizontal surface using a pyranometer.
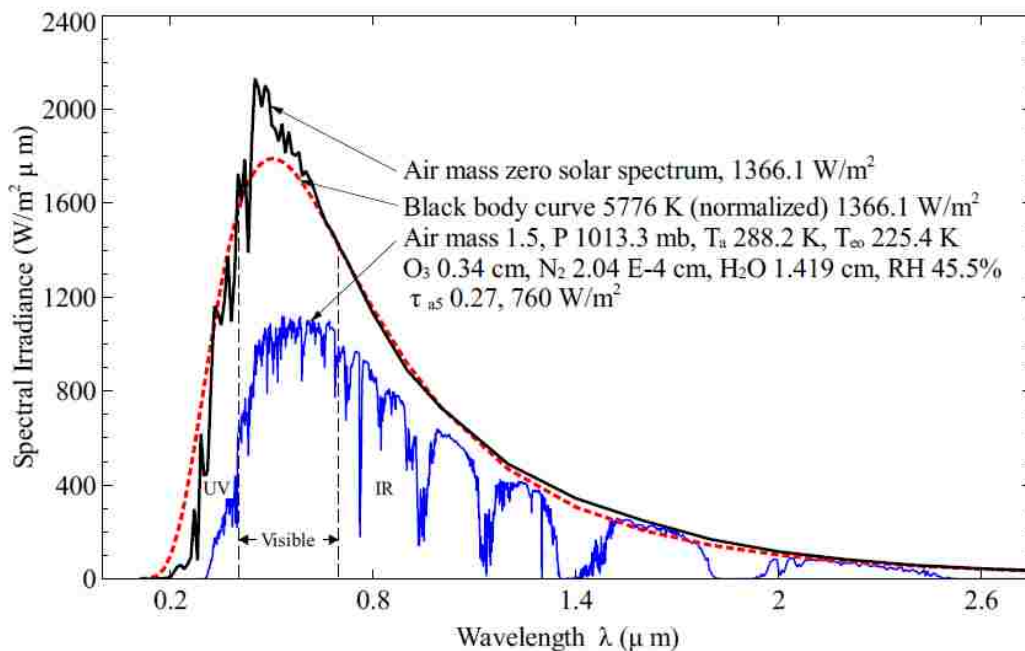
Figure 28 Extraterrestrial solar radiation spectrum (in vacuum below 280 nm, in air above 280 nm): also shown are equivalent black body and atmosphere-attenuated spectra (SMARTS2. U.S Standard Atmosphere USSA. rural aerosol model, Z= 48.19 degree (Air mass 1.5)). Adopted from [95, 96]

The split of total solar radiation on a horizontal surface into its diffuse and beam components is of interest in two contexts. First, methods for calculating total radiation on surfaces of other

36

orientation from data on a horizontal surface require separate treatments of beam and diffuse radiation. Second, estimates of the long-time performance of most concentrating collectors must be based on estimates of availability of beam radiation.
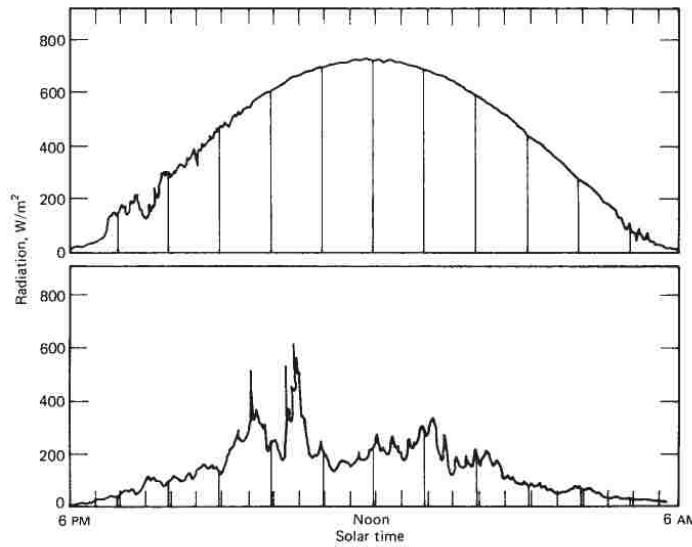
Figure 29 Total (beam and diffuse) solar radiation on a horizontal surface versus time for clear and largely cloudy day, latitude 43 degree, for days near equinox. Adapted from [95, 96]

To decompose the global irradiance on a horizontal surface into its beam and diffuse components the hourly clearness index should be determined beforehand. The usual approach is to correlate I_d/I, the fraction of the hourly radiation on a horizontal plane which is diffuse, with k_T, the hourly clearness index.

$$\frac{I_d}{I} = \begin{cases} 1.0 - 0.09k_T & for\ k_T \leq 0.22 \\ 0.9511 - 0.1604k_T + 4.388k_T^2 - 16.638k_T^3 + 12.336k_T^4 & for\ 0.22 < k_T \leq 0.80 \\ 0.165 & for\ k_T > 0.8 \end{cases}$$

Where, k_T, represents the clearness index for the specified hour. The clearness index can be calculated as following.

$$k_T = \frac{I}{I_o}$$

Where, I_o, denotes the Extraterrestrial Irradiance on a horizontal surface for an hour period. I_o might be calculated using the next equation.

$$I_o = \frac{12 \times 3600}{\pi} G_{sc} \left(1 + 0.033 cos\frac{360n}{365}\right) \times \left(cos\phi cos\delta [\,sin\omega_2 - sin\omega_1\,] + \frac{\pi(\,\omega_2 - \omega_1\,)}{180} sin\phi sin\delta\right)$$

37

The hourly beam component of Irradiance on a horizontal surface then can be calculated by subtracting the diffuse irradiance from the total Global Irradiance.

$$I_b = I - I_d$$

Radiation on Tilted Surfaces

The last step in calculation of radiation on a tilted collector is to correlate decomposed beam and diffuse radiation incidents on the horizontal surface to corresponding terms on tilted surface. Beam radiation on the tilted surface is correlated to that on a horizontal surface through a geometric coefficient as following

$$R_{b,ave} = \frac{a}{b}$$

Where

$$a = (\sin \delta \sin \phi \cos \beta - \sin \delta \cos \phi \sin \beta \cos \gamma) \times (\omega_2 - \omega_1) \times \frac{\pi}{180}$$

$$+(\cos \delta \cos \phi \cos \beta + \cos \delta \sin \phi \sin \beta \cos \gamma) \times (\sin \omega_2 - \sin \omega_1)$$

$$-(\cos \delta \sin \beta \sin \gamma) \times (\cos \omega_2 - \cos \omega_1)$$

And

$$b = (\cos \phi \cos \delta) \times (\sin \omega_2 - \sin \omega_1) + (\sin \phi \sin \delta) \times (\omega_2 - \omega_1) \times \frac{\pi}{180}$$

While estimating the beam component of solar irradiance on sloped collector is straightforward, that of diffuse term is more complicated. However, since parabolic trough only focuses the beam direction effectively, we skip the estimation of diffuse radiation. Detailed information about this topic are available in references.

Summary

In this research, the parabolic trough collector is assumed to be installed horizontally in an East-West direction with continuous adjustment using a one axis tracking system. It is assumed

that the PTC is installed in Sandia National Laboratories at Albuquerque, NM, USA. The latitude, longitude and elevation of this location is specified in Table 3.

Location	Latitude	Longitude	Elevation
Albuquerque, NM	35 ^{0}, 5'	-106 ^{0}, 39'	5,312 ft.

Table 3 the Latitude, Longitude, and Elevation of the Site

Table 4 summarize the angle of incidence, slope, and surface azimuth angle computed for Albuquerque in July 11th from 6 AM to 6 PM. These data are used in this research to trace the solar irradiance and compute solar incidence on the collector. Figure 19 illustrates the tabulated data in a graph.

Time	E	δ	θ$_z$	ϒ$_s$	θ	β	γ
6:00:00	-5.52	22.04	79.80	-109.92	67.96	62.2	0
7:00:00	-5.53	22.04	68.06	-102.24	63.41	27.8	0
8:00:00	-5.53	22.03	55.95	-94.53	53.19	6.7	0
9:00:00	-5.54	22.03	43.70	-85.91	40.73	3.9	180
10:00:00	-5.55	22.02	31.62	-74.54	27.38	9.3	180
11:00:00	-5.55	22.02	20.48	-55.16	13.64	12.0	180
12:00:00	-5.56	22.01	13.34	-12.3	0.24	13.0	180
13:00:00	-5.56	22	16.74	41.83	14.12	12.6	180
14:00:00	-5.57	22	26.93	68.16	27.85	10.7	180
15:00:00	-5.57	21.99	38.78	81.75	41.19	6.6	180
16:00:00	-5.58	21.99	51.01	91.16	53.62	1.4	0
17:00:00	-5.58	21.98	63.21	99.1	63.74	17.4	0
18:00:00	-5.59	21.98	75.14	106.7	68.02	47.3	0

Table 4 the angles of solar irradiance on a horizontal East-West oriented single axis tracking PTC installed in Albuquerque, NM, July 11, 2005
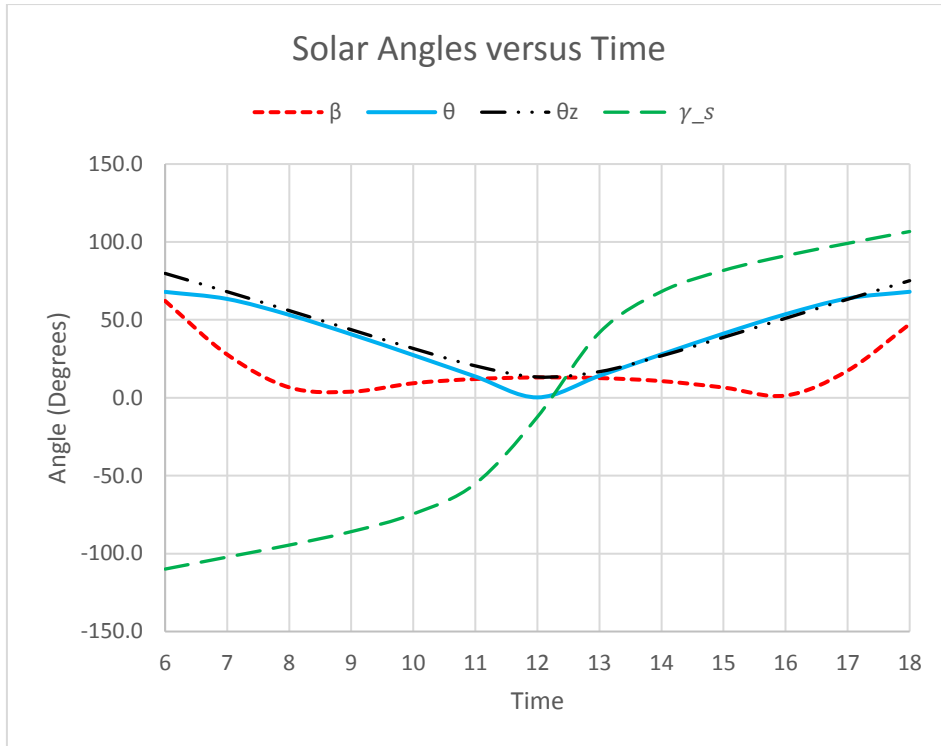
Figure 30 Angles of Solar Incidence on a Single Axis Tracking Collector Installed at Albuquerque, NM, USA.

Chapter 3: Numerical Simulation

3.1 Introduction

A parabolic trough power plant is indeed a power system such as a Rankine steam turbine/generator surrounded by large fields of mirrored parabolic trough collectors which work as the steam-generation system of power plant. Solar irradiation is collected in these fields to heat up a heat-transfer fluid (HTF). Some of these power plants consist also optional Thermal Energy Storage (TES) and/or fossil-fuel-fired backup systems. The use of TES results in both dispatchable generation and higher annual generation per unit of capacity, although the larger collector field and storage system lead to a higher upfront capital investment. Trough solar fields can also be deployed with fossil-fueled power plants to augment the steam cycle, improving performance by lowering the heat rate of the plant and either increasing power output or displacing fossil-fuel consumption. On the other hand, steam generation system is eliminated in direct steam CSP for the working fluid of receiver is the one that works in the turbine. Invention and development of turbomachinery that works with S-CO$_2$ paves the way towards constructing such a simple compact power plants. [17, 40]. S-CO2 can be used as working fluid in almost any type of CSP among which parabolic trough power plants are widely considered as the most mature technology [7, 47].
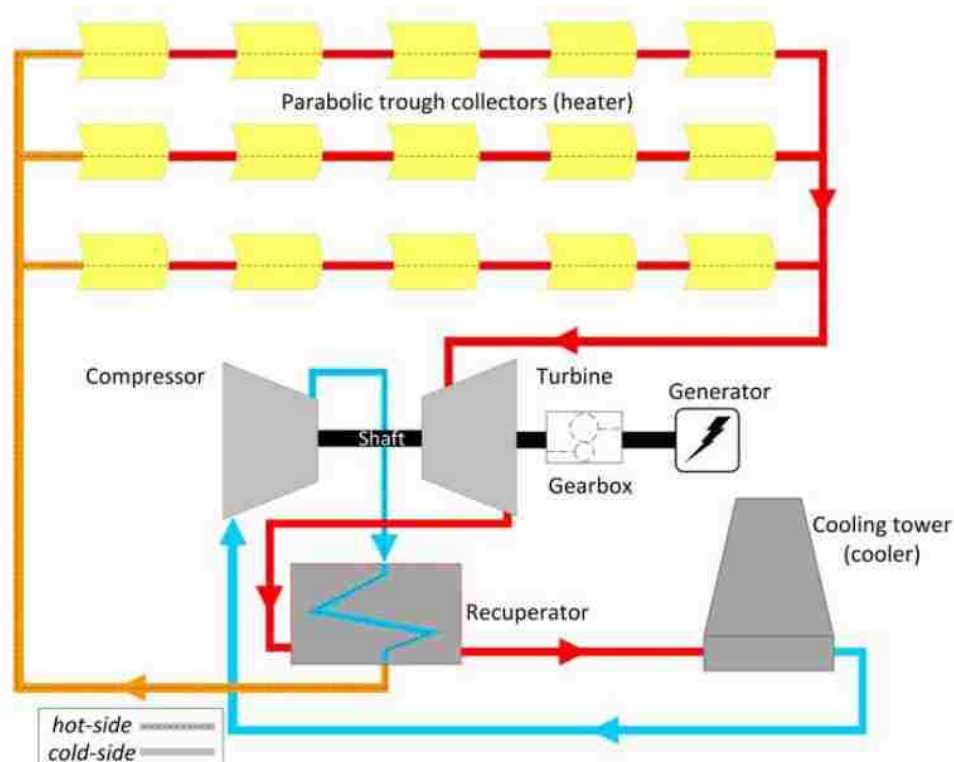
Figure 31 Schematic of a Parabolic Trough S-CO$_2$Power Plant [32]

The solar field of a parabolic trough power plant is made up of large modular arrays of 1-axis tracking solar collectors arranged in parallel rows, usually aligned on a north-south or east-west horizontal axis. Each solar collector has a linear parabolic-shaped reflector that focuses the direct beam solar radiation onto a linear receiver (absorber tube) located at the focal line of the parabola (Figure 37, 38). The collectors track the sun from east to west during the day, with the incident radiation continuously focused onto the linear receiver, within which an HTF is heated. The heated working fluid are then collected and sent to the turbine. The length of the path that HTF flows inside the solar receivers depends on several factors including the outlet temperature of recuperators, the inlet temperature of turbine, mass flow rate, concentration factor of reflectors, etc. However, regardless of the length of the path HTF flows inside the solar field its path consists of a series of identical collectors with the same angles towards the sun at each instance. For instance, in figure 37 HTF flows through 38 identical collectors to be heated up.

3.2 System Geometry

Currently there is no collector in the market specially manufactured for supercritical carbon dioxide. Hence, the geometric model of this research is generated based on the data of LS-2 collector. The main characteristics of this collector are summarized in Appendix F [36, 48, 86].

The heat collection element (HCE) of a PTC is basically a tube surrounded by an anti-reflective evacuated glass tube which protects the absorber from degradation and reduces the heat losses. (Figure 39, 40). To increase the absorptance for solar radiation and to decrease the emittance for the temperature range in which the surface emits radiation, the receiver tube is coated with a selective coating. The space between the glass cover and the absorber tube is evacuated to reduce heat losses at high operating temperatures and to protect the solar-selective absorber surface from oxidation. Either ends of HCE are sealed using conventional glass to metal seals and metal bellows. The space between bellows provides a place to attach the HCE support brackets. Over the time heat transfer oils, which are most commonly used as the heat transfer fluid, decompose at high temperatures and release Hydrogen which penetrates the stainless steel tube and enters the evacuated space. Hence, in LS-2 collectors chemical getters are placed in the annulus to absorb hydrogen. Since such a problem does not happen in S-CO$_2$ carrying collectors, getters might be removed from collectors especially designed for S-CO$_2$.
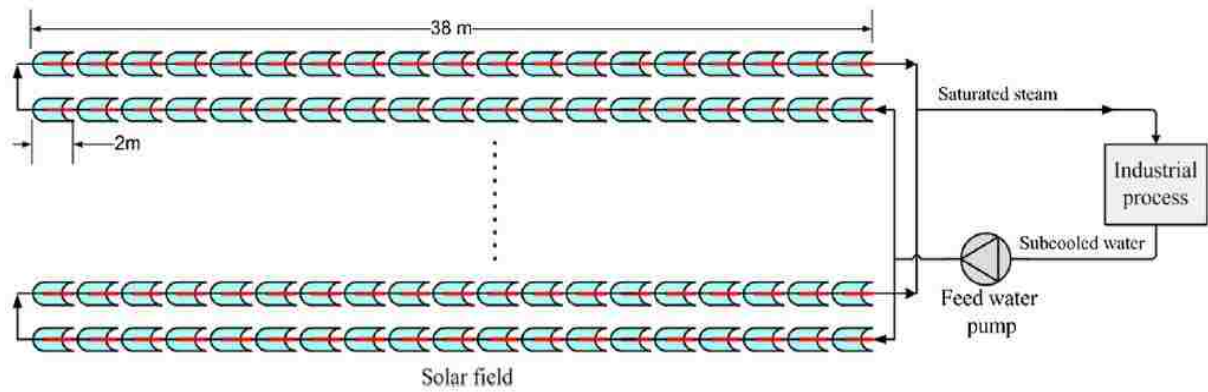
Figure 32 Simplified diagram of a solar field using Capsol-type parabolic-trough collectors configured [33]

Figure 33 LS-2 collector test at Sandia National Laboratory, USA [37]
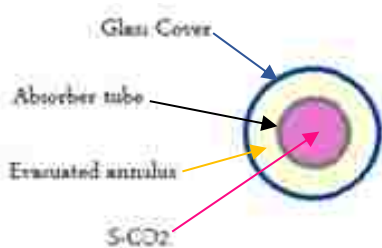
Figure 34 Cross-sectional schematic of parabolic receiver tube
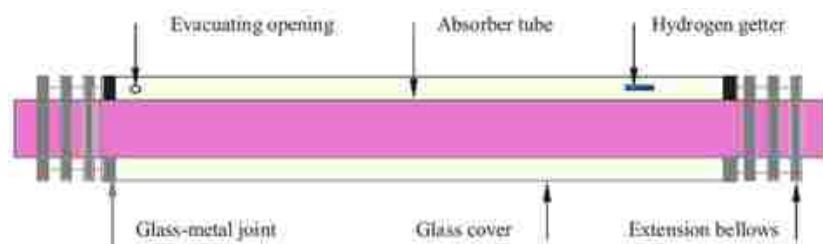
Figure 35 Schematic of the structures of a parabolic trough receiver.

A parabolic trough solar field consists of hundreds of similar collectors that are connected to each other through a piping system. This piping system collects the high pressure fluid that is pre-heated in recuperators and distributes it among the collectors in solar field. Then it collects

the high temperature fluid from the solar field and carries it to the turbine inlet. From a thermal-fluid point of view the only significant difference between these collectors is their inlet boundary conditions. Hence, modeling only one collector is enough to provide a comprehensive thermal-fluid analysis of the working fluid inside the parabolic trough collectors. As previously discussed S-CO_2 is pressurized in turbo compressors up to 10 MPa to 20 MPa and then is heated in recuperators way above its critical temperature before entering the solar field. Therefore, in none of the collectors transcritical phase change happens. This means that the flow field regime is almost the same inside the collectors and does not change along the collector line. Hence, in this research neither the variations of flow field through the whole receiver line nor the transcritical phase states are analyzed. Instead, a single collector is modeled to reduce both the memory capacity and the CPU time (figure 18, 19 and 20).

To avoid the geometric complications that increase the number of mesh and deteriorate the convergence of computational analysis, following simplifications are done.

   a. Glass-metal joint and extension bellows are ignored. Instead it is assumed that the receiver is sealed on both sides using adiabatic walls.
   b. Evacuating opening is ignored.
   c. Hydrogen getter is ignored.
   d. Bracket supports are ignored.
   e. The collector is a single parabolic mirror instead of 10 pieces of mirrors assembled together which means that all gaps between mirrors are ignored.

Figure 41 illustrates four views of the modeled LS-2 collector while figure 42 shows the cross section of receiver.

a)   b)

c)   d)
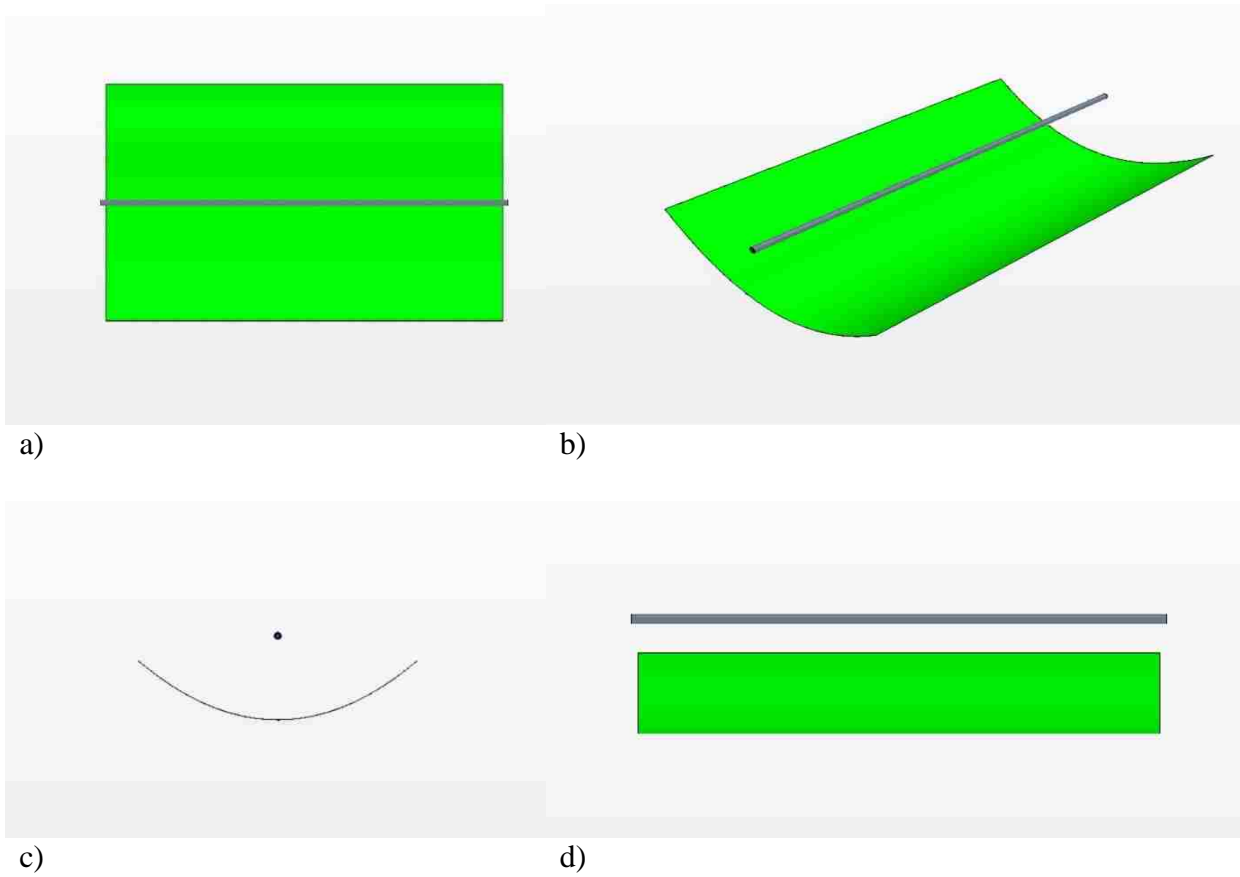
Figure 36 Geometry of LS-2 collector a) top view b) Isometric view c) front view d) side view
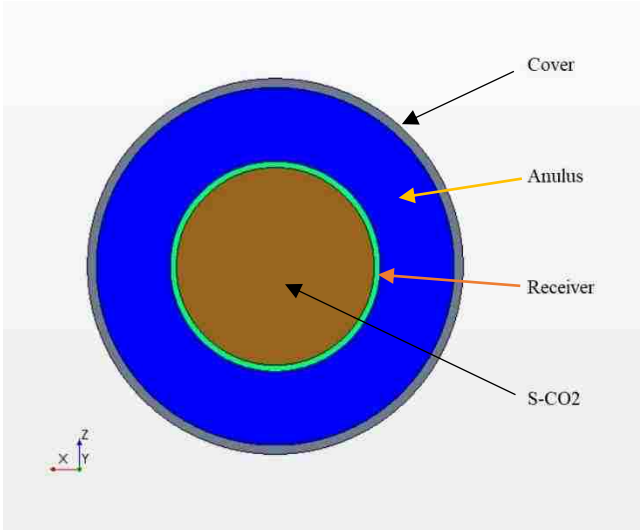
Figure 37 Cross section of LS-2 receiver. Replace the photo with LS-2 cross section

3.3 Mesh Generation

Three distinct types of mesh are used in this research.

- Thin mesher which generates a prismatic layered volume mesh for thin geometries. It is used to mesh the reflector, glass cover and receiver tube.

- Polyhedral mesher, which generates a volume mesh that is composed of polyhedral-shaped cells. This type of mesh is used to mesh the bulk fluid regions including the S-CO_2 inside the receiver tube and hydrogen inside the annulus. It is also used to mesh the plug inserted in the core of test model receiver used to evaluate the numerical simulation.
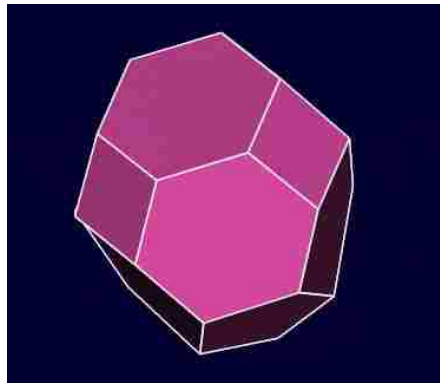
Figure 38 polyhedral mesh [82]

- Prismatic mesher is used to generate orthogonal prismatic cells next to wall surfaces or boundaries. Such a fine mesh is necessary in solid-fluid boundaries to capture sharp hydraulic and thermal gradients in boundary layers.

Among several methods for meshing the bulk fluid regions polyhedral meshes are relatively easy and efficient to build and contain approximately five times fewer cells than a tetrahedral mesh for a given starting surface. Figure 44 demonstrates the meshes generated in different regions of solution field. Meshes are aligned on either side of interfaces to improve the data transfer between cells from one region to another. In addition, the size, density and distribution of meshes are controlled to generate finer cells in solid-fluid boundaries where large gradients exist and coarser cells in the regions where the gradients are smaller. Such a distribution of cells helps to improve the accuracy of the flow solution with considerably lower number of cells compared to uniform distribution.
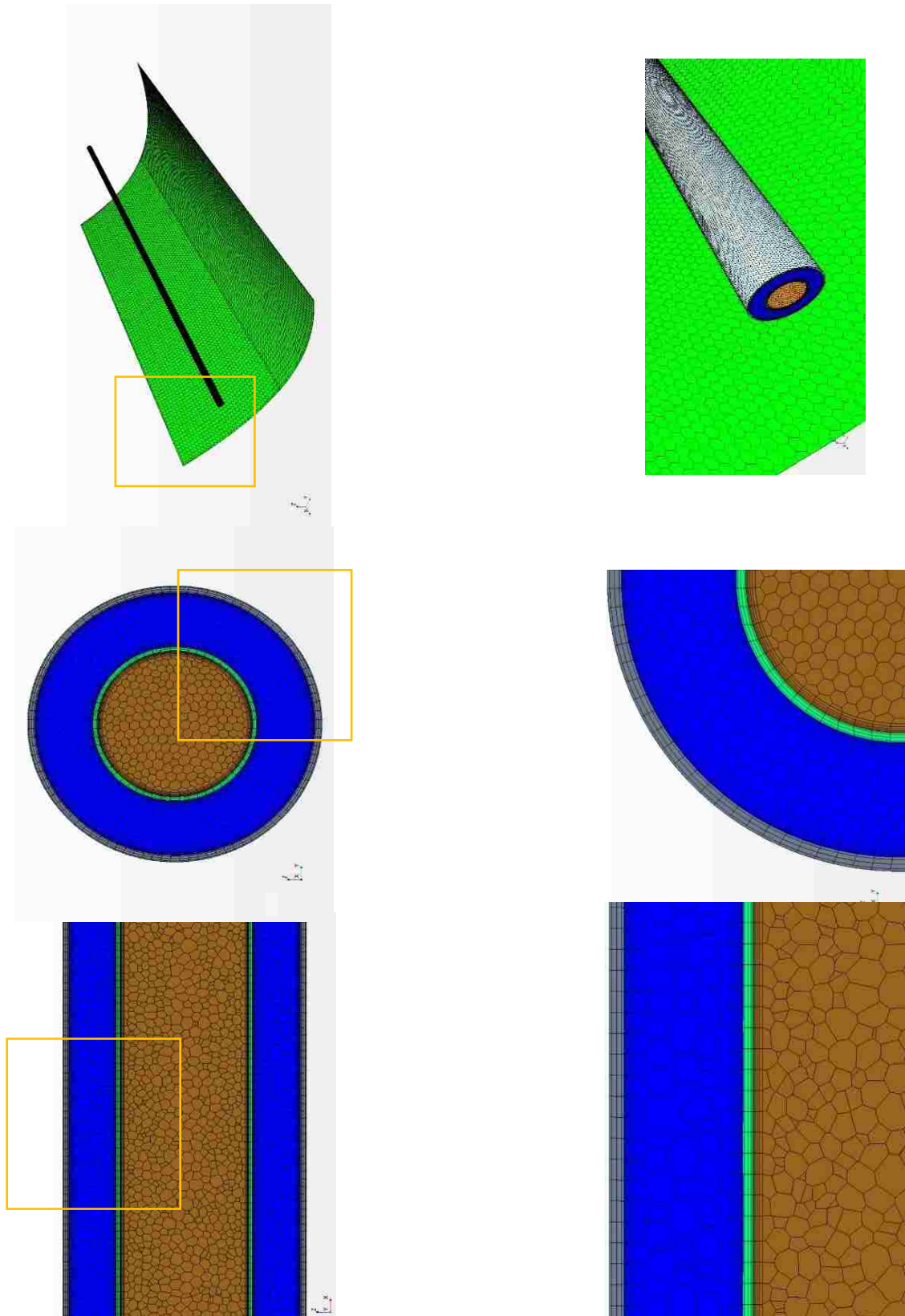
Figure 39 Meshes generated to discretize different regions of the solution domain

3.4 Governing Equations

That the parabolic trough tracks the sun continuously makes the receiver a moving container of flowing fluid. However, technically the PTC is not adjusted continuously, but in short periods which means the collector can be considered stationary in between adjustments. In addition, the rotation of PTC at each adjustment is of the order of degrees which makes it three orders of magnitudes slower than the flow velocity. Hence, compared to the flow inlet velocity the rotation of PTC is negligible, and a quasi-steady state scheme can provide a quite accurate solution.

Hence, governing equations of flow field consists of a set of three conservation equations plus the transport equations that model the turbulence supplemented by a set of empirical correlations to predict physical properties of S-CO_2 and H_2 with respect to the pressure and temperature. These equations are as following.

3.4.1 Conservation Laws

- Conservation of Mass (Continuity)

$$\frac{\partial \rho}{\partial t} + \frac{\partial}{\partial x_i}(\rho U_i) = 0$$

- Conservation of Momentum

$$\frac{\partial}{\partial t}(\rho U_i) + \frac{\partial}{\partial x_i}(\rho U_i U_j) = -\frac{\partial P}{\partial x_i} + \frac{\partial}{\partial x_j}\left[\mu\left(\frac{\partial U_i}{\partial x_j} + \frac{\partial U_j}{\partial x_i} - \frac{2}{3}\delta_{ij}\frac{\partial U_l}{\partial x_l}\right)\right] + \rho g_i$$

- Conservation of Energy

$$\nabla \cdot \rho\left(U + \frac{v^2}{2}\right)\vec{v} = \nabla \cdot (k\nabla T) + q_g + \rho\vec{g} \cdot \vec{v} - \nabla \cdot (\tau \cdot \vec{v})$$

Where τ indicates the stress tensor and q_g denotes the generated heat which in this case equals zero.

3.4.2 Reynolds Averaged Form of Conservation Laws

These equations may be averaged term by term to generate statistical equations of motion. These are based on Reynolds decomposition which assumes each random variable such as velocity consists of a mean term and a randomly fluctuating term.

$$U = \bar{U} + u \qquad\qquad P = \bar{P} + p \qquad\qquad T = \bar{T} + \theta$$

Substituting these decomposed variables in the governing equations for an incompressible fluid yields in well-known Reynolds averaged equations as following [78].

$$\frac{\partial \rho}{\partial t} + \frac{\partial}{\partial x_i}(\rho \bar{U}_i) = 0$$

$$\frac{\partial}{\partial t}(\rho \bar{U}_i) + \frac{\partial}{\partial x_j}(\rho \bar{U}_i \bar{U}_j) = -\frac{\partial \bar{P}}{\partial x_i} + \frac{\partial}{\partial x_j}\left[\mu\left(\frac{\partial \bar{U}_i}{\partial x_j} + \frac{\partial \bar{U}_j}{\partial x_i} - \frac{2}{3}\delta_{ij}\frac{\partial \bar{U}_l}{\partial x_l}\right)\right] + \frac{\partial}{\partial x_j}(-\rho\overline{u_i u_j}) + \rho g_i$$

$$\frac{\partial}{\partial x_i}(\rho u_i T) = \frac{\partial}{\partial x_i}\left[\left(\frac{\mu}{Pr} + \frac{\mu_t}{\sigma_T}\right)\frac{\partial T}{\partial x_i}\right] + S_R$$

These Equations are called Reynolds-averaged equations. Although their general form looks like the instantaneous governing equations, the velocities and other solution variables now represent time-averaged values. Moreover, additional terms now appear that represent the effects of turbulence. These Reynolds stresses $-\rho\overline{u_i u_j}$ must be modeled to close RANS Equations.

3.4. 3 Turbulent Flow Models

Available turbulence models have been originally developed to predict the flow field and heat transfer of constant property fluids. Hence, the extension of their applicability to variable property flows is questionable [39]. However, in last two decades the predictive capabilities of various turbulence models are tested to experimental data and some models are proved to predict such flow fields reasonably accurate. In 1995, Koshizuka et al. numerically analyzed a turbulent flow utilizing the Jones-Launder k-ε turbulence model and compared the results with Yamagata's experimental data for water at supercritical pressures [53]. Their study showed that the k-ε turbulence model without modification for fluctuating terms performed reasonably well compared with the Yamagata experimental results. Kim et al. studied the predictive capabilities

of a variety of two-equation turbulence models in 2004 [55]. Several low-Reynolds k-ε models, two k-ω models and three high-Reynolds k-ε models were tested against experimental data obtained from Yamagata using commercial software, Fluent. Although each model showed some deficiencies, the RNG k-ε model made the closest prediction to the Yamagata experimental values. In the same year, He et al. conducted a similar analysis to investigate the predictive capabilities of several two-equation low-Reynolds turbulence models for mixed convective heat transfer [56] using another CFD code, SWIRL. Their study found that the buoyancy effect on turbulence and heat transfer is poorly predicted by typical two-equation low-Reynolds number turbulence models. Roelofs [57] compared the predictive capabilities of an RNG k-ε model with a Reynolds Stress Model (RSM). The RNG k-ε model included enhanced wall functions. The results of RSM model found to be comparable to those produced by the RNG k-ε model in simple geometries. Roelofs concludes that even though the RSM predictions in a single channel may be on par with a common two equation model, for more complicated geometries the RSM will give a more accurate prediction. Later in 2006, Yang et al. [58] performed a similar analysis comparing several k-ε turbulence models, three two layer models, and four k-ω models to the experimental data of Yamagata. The two-layer model of Hassid and Poreh resulted in the best prediction and the k-ε model with standard wall functions also gave an acceptable prediction. Seo et al. (2006) [59] used the FLUENT software to prove that the standard k-ε model with standard wall functions works well in the normal heat transfer regime, however it failed in producing reasonable predictions in a high heat flux and low mass flow rate regime. He, S. et al. (2008) also compared the performance of a number of turbulent models in predicting supercritical pressure heat transfer in a vertical tube. They concluded that the V2F model performs the best among all models tested [58, 60]. In 2012, Mohseni et al. modified a low Reynolds number k–ε turbulence model for applications in supercritical fluid flows which led to the flow predictions that were in good agreement with the experiments for enhanced mode of heat transfer [46].

To conclude, multidimensional turbulence models are more successful in predicting the supercritical flow and heat transfer than the one-dimensional correlations. Given that in these conditions radial property variations have a significant effect on fluid flow and heat transfer, particularly in the boundary layer, such results are expected [104]. Among two dimensional models k-ε models work well for simple geometries and conditions while RSM model results in the best predictions when it comes to more complicated situations where other models poorly predict the flow field and heat transfer. To conclude, the simple geometry of flow field inside

the PTC receiver k-ε model is used to model the turbulence of the flow field inside the receiver tube.

$$\frac{\partial}{\partial t}(\rho k) + \frac{\partial}{\partial x_i}(\rho k u_i) = \frac{\partial}{\partial x_j}\left(\alpha_k \mu_{eff} \frac{\partial k}{\partial x_j}\right) + G_k + G_b - \rho\varepsilon - Y_M + S_k$$

$$\frac{\partial}{\partial t}(\rho \epsilon) + \frac{\partial}{\partial x_i}(\rho \epsilon u_i) = \frac{\partial}{\partial x_j}\left(\alpha_k \mu_{eff} \frac{\partial \epsilon}{\partial x_j}\right) + C_{1\epsilon}\frac{\epsilon}{k}(G_k + C_{3\epsilon}G_b) - C_{2\epsilon}\rho\frac{\epsilon^2}{k} - R_\epsilon + S_\epsilon$$

In these equations, G_k represents the generation of turbulence kinetic energy due to the mean velocity gradients. G_b is the generation of turbulence kinetic energy due to buoyancy. Y_M represents the contribution of the fluctuating dilatation in compressible turbulence to the overall dissipation rate. The quantities α_k and α_ε are the inverse effective Prandtl numbers for k and ε respectively. S_k and S_ε are user-defined source terms [79]. The term G_k represents the production of turbulence kinetic energy and is modeled as following.

$$G_k = -\rho\overline{u_\iota u_J}\frac{\partial u_j}{\partial u_i}$$

G_b denotes the generation of turbulence dut to boyancey and is estimated by

$$G_b = \beta g_i \frac{\mu_t}{Pr_t}\frac{\partial T}{\partial x_i}$$

Where g_i is the component of gravitational force in the i direction and Pr_t is the turbulent Prandtl number calculated

$$Pr_t = \frac{1}{\alpha}$$

Where α is given by

$$\left|\frac{\alpha - 1.3929}{\alpha_0 - 1.3929}\right|^{0.6321}\left|\frac{\alpha + 2.3929}{\alpha_0 + 2.3929}\right|^{0.3679} = \frac{\mu_{mol}}{\mu_{eff}}$$

In which

$$\alpha_0 = \frac{1}{Pr} = \frac{k}{\mu c_p}$$

The coefficient of thermal expansion, β, is defined as

$$\beta = -\frac{1}{\rho}\left(\frac{\partial \rho}{\partial T}\right)_p$$

The dilatation dissipation term, Y_M, is included in the k equation. This term is given by

$$Y_M = 2\rho\epsilon M_t^2$$

Where Mt is turbulent Mach number, defined as

$$M_t = \sqrt{\frac{k}{a^2}}$$

In which *a* denotes the speed of sound

$$a = \sqrt{\Upsilon RT}$$

Finally,

$$R_\epsilon = \frac{C_\mu \rho \eta^3 (1 - \eta/\eta_0)}{1 + \beta\eta^3}\frac{\epsilon^2}{k}$$

Where $\eta = Sk/\epsilon$, , $\eta_0 = 4.38$ and $\beta = 0.012$

The model constants are derived analytically by RNG theory, $C_{1\varepsilon} = 1.42$, $C_{2\varepsilon} = 1.68$

3.4.4 Heat Transfer Equations

In addition to the heat transfer inside the flow, several heat transfer modes exist between sun, parabolic trough collector, different regions of receiver, and the surroundings. A small portion of the direct solar irradiance received on the surface of collector is absorbed while the rest of it (up to 94% in LS-2 collectors) is reflected. Most of this reflected direct solar irradiance is concentrated on the glass cover. Glass cover in its turn reflects a small ration of this irradiance back to the surroundings, including the sky and the collector, and absorbs an even smaller portion while it transmits more than 90 % of the irradiance into the annulus. While thermal conduction spreads the absorbed energy inside the glass cover and heats it up, the transmitted portion of incident irradiance is emitted on the receiver tube through thermal radiation. This time above 94 % of the incident irradiance is absorbed by the coating of the tube and the rest of it is reflected back to the cover. The reciprocating reflection between the cover and the tube

occurs several times until the whole energy is either absorbed by either of which or is transmitted out to the surroundings through the glass cover.

The thermal energy absorbed by the receiver tube spread inside the tube via conduction and finally is swept by the fluid inside the tube. At the end, the thermal energy distributes inside the flow field and warms the fluid up. To complete this picture the natural convection inside the annulus and the forced or natural convection, depending on the wind velocity, around the glass cover as well as the collector should be considered. Figure 25 illustrates the system of this thermal network.
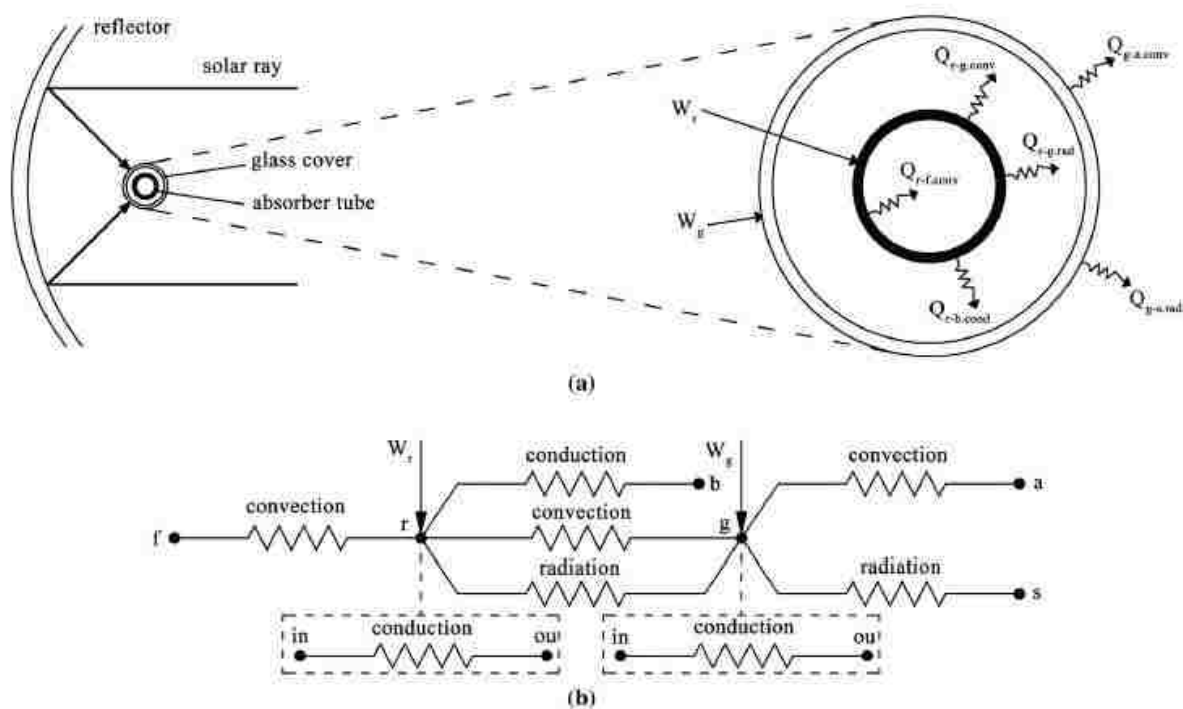
Figure 40 a. Heat Transfer Schematic of a Cross Section b. Thermal Resistance Network [83]

3.5   Boundary Conditions

Solar Radiation

One of the contributions of this research is to replace simplified thermal boundary conditions investigated previously by other researchers with more realistic boundary conditions. To reach this goal the solar incident radiation is modeled. This radiation is concentrated on one side of the receiver by the parabolic mirrors while the other side is exposed to the direct solar radiation.

Therefore, a circumferentially non-uniform radiation which is a strong function of the angle and varies along the axis incidents the receiver [8, 18, 23].

Moreover, the irradiance varies with time and is expected to meet its maximum around solar noon [7]. Figure 46 which is generated using TMY3 data illustrates the variation of direct normal irradiation and solar incidence on the collector during a typical summer day in Albuquerque, NM.
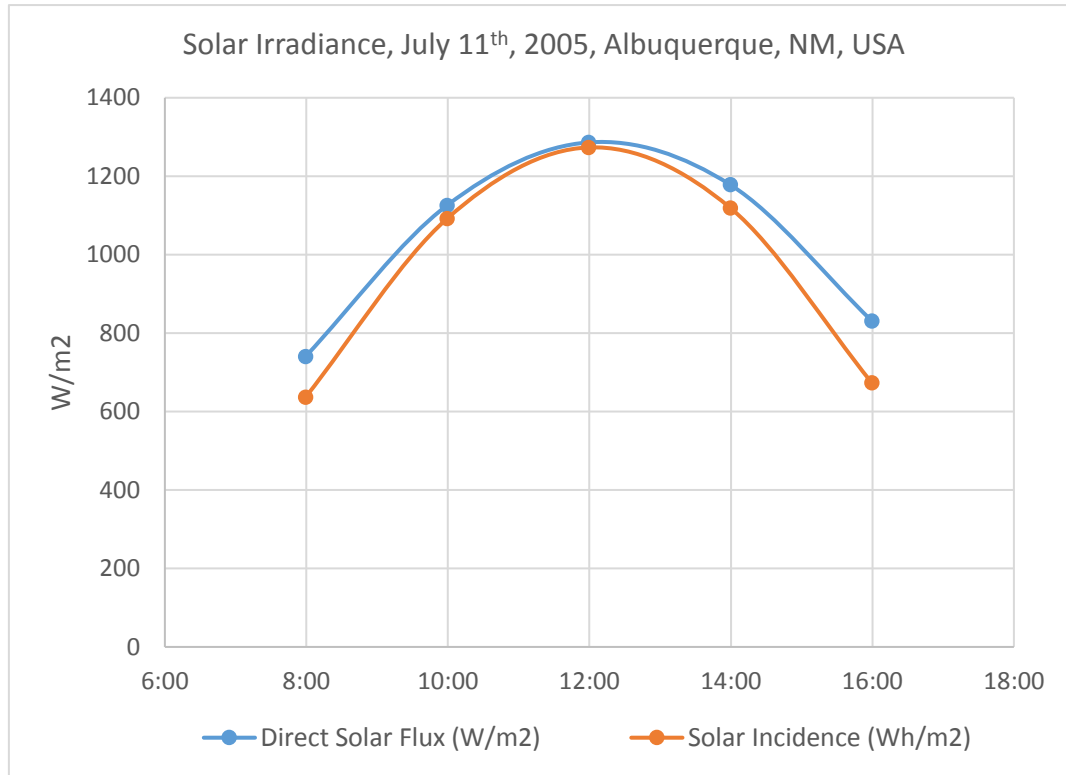
Figure 41 Variation of solar direct normal irradiation and solar irradiation incidence during a typical summer day [TMY3]

To reasonably estimate the variations of flow field and heat transfer during the whole solution time interval (July 11th, 2005 in this research) one can discretize the time interval into a series of shorter intervals. Then the solar irradiance and ambient conditions should be averaged for each of these short intervals and plugged into software. In the next step, governing equations should be solved in steady state form for each of these short intervals. Finally, the results can be plotted versus time and a curve can be fitted to the discrete points. Theoretically, the shorter the time intervals are, the more accurate is the estimation of the variation over time. However, shorter time intervals costs increased CPU time which should be balanced at some point. In this project, five time-steps are modeled, namely 8:00 AM, 10:00 AM, 12:00 PM, 2:00 PM, and 4:00 PM.

Convection

Conducting a coupled wind-heat transfer analysis causes huge problems including but not limited to the enormous number of cells which need both higher memory capacity and longer CPU time. In addition, it might adversely affect the convergence of numerical analysis or even yields in divergence. Hence, modeling the wind effect by a constant convection coefficient sounds like a reasonable method that simplifies the thermo-fluid analysis considerably. However, the fluid flow around a PTC is more sophisticated than cross flow around a single horizontal tube. Therefore, the cross-flow assumption fails in describing the flow around the receiver tube of a PTC [24]. Convection heat transfer coefficient around a tubular absorber with a glass cover was studied by Mullick & Nanda [25]. They proposed following correlation in metric system to predict the convection coefficient:

$$h_w = 4V_w^{0.58}D^{-0.42}$$

where V_w is the wind velocity and D is the outer diameter of glass cover. The exact flow pattern and subsequently heat loss around the collector tube though, is a strong function of the collector orientation and depends less on the wind velocity [24, 26, and 27]. As previously discussed the parabolic trough modeled in this research is equipped with a single axis tracking system oriented in south-north direction. So, depending on the apparent position of the sun in the sky, the pitch angle changes. This motion not only affects the absorbed solar irradiance but also changes the convection coefficient on the outer surface of collector. Therefore, to avoid over simplification in boundary conditions one needs to consider the effect of pitch angle on the averaged convection coefficient. Table 5 summarizes the Nusselt number versus pitch angle as tabulated by A. A. Hachicha et al [26].
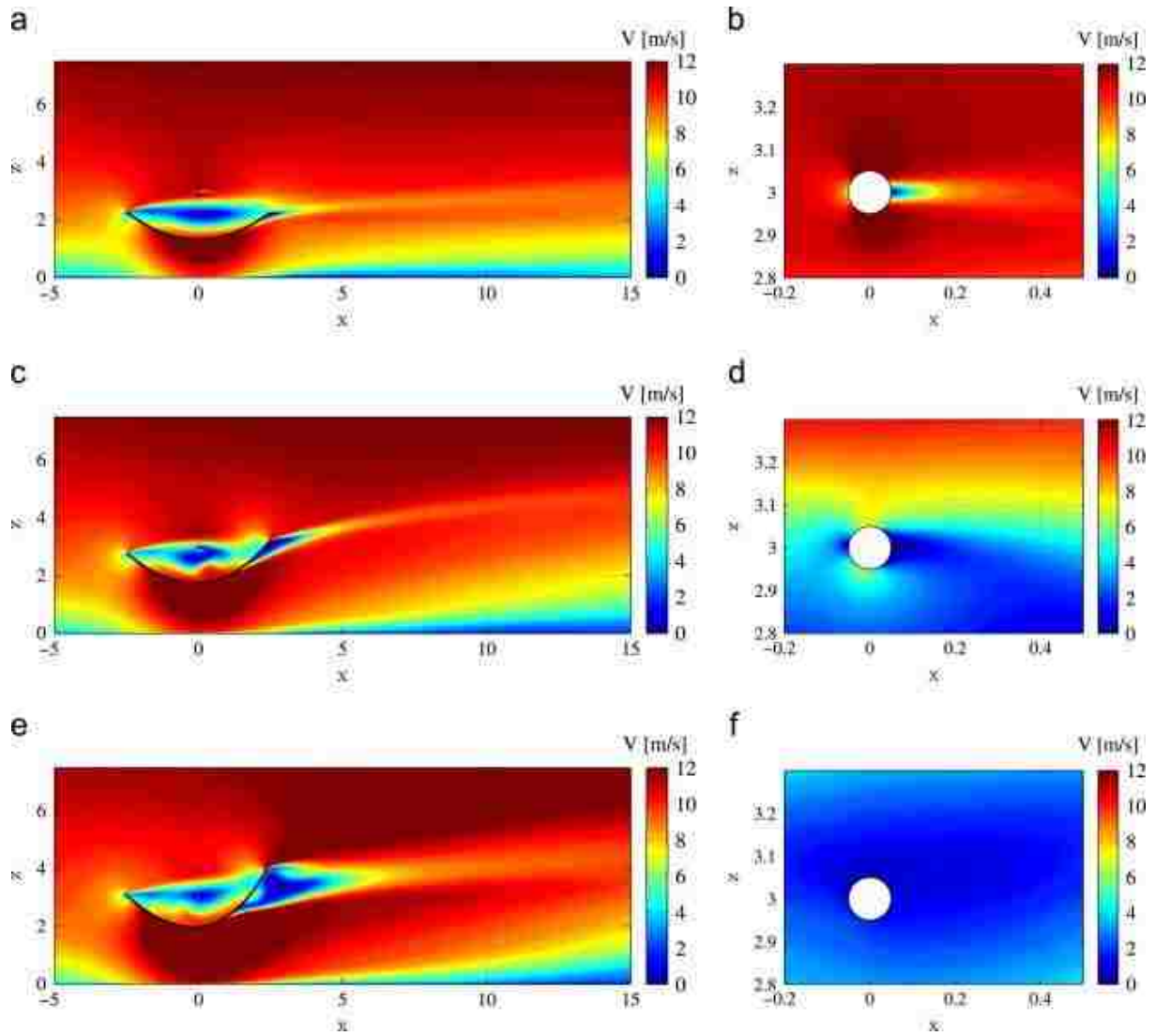
Figure 42 Velocity magnitude at the respective angles of highest heat loss for the three pitch angles. (a) and (b) Ɵ=0° shows the higher air speed around the receiver compared with (c) and (d) the medium trough at 5° pitch, and (e) and (f) the deep trough at 10° pitch. [27]

Position	Nu_{avg}	Nu_{fsp}	Nu_{max}/Pos	Nu_{min}/Pos
0°	24.5	33.1	41.4/289.5°	9.5/196.8°
45°	36.4	58	61.2/350.9°	15.9/67.5°
90°	47.4	86	86/0°	27.3/222°
135°	25.1	25.2	32.4/269.6°	15.1/64.6°
180°	22.5	23.7	29.1/269.5°	7.4/85.9°
270°	43.4	78.2	78.9/355.84°	21.1/273.4°
Cylinder	52.2	86	86.57/357.4 °	17.4/272.2°

Table 5 Numerical data of averaged, front stagnation, maximum and minimum Nusselt numbers for each pitch angle

Sky Radiation

To predict the performance of solar collectors, the radiation exchange between its surface and the sky should be assessed. Assuming that sky emits as a blackbody at some equivalent temperature T_s the actual net radiation between a horizontal flat plate and the sky is given by

$$Q = \varepsilon A \sigma \left(T^4 - T_s^4 \right)$$

Where ε *is the* emittance of the plate, A is its area, and T is the temperature of plate *while T_s* denotes the equivalent blackbody sky temperature and is computed using following equation proposed by Berdahl and Martin [102].

$$T_s = T_a \left[0.711 + 0.0056 \, T_{dp} + 0.000073 \, T_{dp}^2 + 0.013 \cos(15t) \right]^{\frac{1}{4}}$$

where T_s and T_a are in degrees Kelvin and T_{dp} is the dew point temperature in degrees Celsius.

Inlet

Constant total temperature and mass flow rate are applied as boundary conditions at the inlet boundary of the receiver. The inlet temperature is 300 ^{0}C , the inlet pressure is 10 MPa, and the flow rate equals 530 Lit/min. These conditions are reasonably close to the real conditions in a solar thermal power plant where recuperators are used to preheat the S-CO$_2$. Since the length of receiver is two orders of magnitude larger than its diameter, the axial thermal resistance is by far higher than the radial resistance. Therefore, the axial heat transfer in all solid components is ignorable compared to radial heat transfer. So, the boundaries of these component are thermally insulated.

Outlet

The length over diameter ratio of the PTC receiver is greater than the entry length criterion of turbulent flow i.e. 10 to 20 diameters [38]. So, fully developed condition is used at the outlet

boundary. As discussed earlier all solid components including the receiver tube, the extension bellows and the glass cover are assumed to be insulated at the outlet.

3.6   Initial Conditions

For steady-state simulations, the converged solution should be independent of the initial field. However, the path to convergence, and hence the computational effort that is required to reach convergence, is affected. Therefore, choosing the initial conditions and values judiciously, particularly when the physics is complex is crucial. Each model requires sufficient information for the primary solution data for the primary variables that are associated with the model to be set.   All initial conditions are set up directly. Except turbulence variables. In some cases, turbulence intensity and turbulent viscosity ratio are specified as initial conditions instead of turbulent kinetic energy and turbulent dissipation rate.

In this research, the system is at first solved for a set of simplified models

- Gray Thermal Radiation
- Laminar Flow inside the receiver
- Constant physical properties of S-CO_2

Then the simplified models are replaced with

- Multiband Radiation
- Turbulent Flow Field
- Temperature-dependent properties of S-CO_2

And the results of previous step are used as initial conditions in solving the original problem.

3.7 Summary and Assumptions of Research

- Multiband radiation model is used with two bands. This method allows the user to model the selective behavior of the receiver coating and glass cover.

- Turbulent flow field is modeled using k-ε model.

- Brackets are neglected.

- Sky is considered clear.

- Dust and imperfections of surfaces are not addressed.

- Physical properties of glass cover and selective coating are indeed temperature-dependent. However, in this research their variations are not addressed.

- The reflector is considered a single piece of mirror whereas in practice, it consists of several smaller pieces of mirrors assembled to form a big reflector. There are small gaps between adjacent pieces and mismatch in aligning the mirrors practically. Especially, there is a big gap in the center of reflector parallel to its axis. In an East – West oriented single axis tracking collector this gap is always shadowed by the receiver tube. Hence, it is neglected in this research along with all other gaps and possible misalignments.

- Extension bellows are replaced with adiabatic boundaries.

- The near vacuum condition inside annulus is replaced with a low-pressure hydrogen because the CCM+ software cannot model radiation transmission in a media surrounded by vacuum regions on both sides.

- The deflection of receiver due to its weight and thermal expansion is not addressed. The same goes with the glass cover and the reflector.

- The properties of S-CO_2 are considered a sole function of temperature which means the effect of pressure drop on the properties of S-CO_2 is neglected.

Chapter 4: Results and Discussion

4.1 Mesh Independency

Three meshes are generated for LS-2 collector. The type of meshes are the same but their base sizes are different. Since all other sizes including the prism layer thickness are defined relative to the base size, changing the base size accordingly changes all other sizes of mesh specially the prismatic meshes thickness which controls the wall Y+ function. The number of cells and boundary faces of these meshes are summarized in following table.

Base size of the finest mesh is 2.5 mm and that of coarsest mesh is 3 mm while the base size of the average mesh is 2.7 mm. The expension ratio of the meshes are the same. Also the number of mesh layers of reflector, cover, and receiver tube which are modeled as thin walls are not changed for in order to capture the heat transfer phenomena across a thin wall at least 3 to 5 layers of cells are needed. The temperature profile and axial velocity profile along a vertical line in the middle of receiver tube (x=0 and y = 0) are compared. Although 3 mm base size mesh needs the least CPU time and memory to converge, due to its lower cell numbers, its estimation of axial velocity is up tp 10% off from the finest mesh results in the regions close to the receiver-fluid interface. The error in estimating the temperature is even more and reachs to 14 % in near wall regions. Such a big difference might be the result of failour in capturing thermal and hydrodynamic phenomena in boundary layer where the sharpest gradients are expected. Reviewing the Wall Y+ graph shows that in this case the Y+ in the first cell adjacent to the solid wall varies from 47 to 212 which is quite a large number even for a two layer wall treatment model. In order to resolve this problem an all Y+ wall function scheme is utilized to model the near wall region, but expectedly this technique cannot fully overcome the coarse mesh size adverse ffects.

On the other hand, lowering the base size from 2.7 to 2.5 does not improve the results considerably while increases the number of cells to over 6.5 millions. Such a fine mesh generates a smoother profile specially in near wall regions, but it increases the CPU time drastically. More importantly analyzing such a large number of cells need more than 70 GB of RAM memory. In this research a PC equipped with 80 GB memory is used, but even for such a PC handling 6.5 million meshes is a challenging task. It might be advisable to use more powerful PCs equipped with at least 100 to 200 GB of memory to improve future studies.

Region / Boundary	Coarse Mesh	Medium Mesh	Fine Mesh	
Annulus	4.43E+05	1.68E+06	2.86E+06	cells
Inlet	4.99E+02	1.14E+03	1.64E+03	faces
Inner Wall	9.41E+04	1.08E+05	1.84E+05	faces
Outer Wall	1.50E+05	1.85E+05	3.03E+05	faces
Outlet	5.01E+02	1.14E+03	1.63E+03	faces
Cover	5.99E+05	7.40E+05	1.21E+06	cells
Inlet	3.52E+02	3.84E+02	4.96E+02	faces
Inner Wall	1.50E+05	1.85E+05	3.03E+05	faces
Outer Wall	1.50E+05	1.85E+05	3.03E+05	faces
Outlet	3.52E+02	3.84E+02	4.96E+02	faces
Fluid	7.87E+05	9.23E+05	1.68E+06	cells
Inlet	5.27E+02	5.51E+02	8.02E+02	faces
Interface	9.41E+04	1.08E+05	1.84E+05	faces
Outlet	5.26E+02	5.50E+02	8.08E+02	faces
Reflector	1.11E+05	9.19E+03	4.88E+04	cells
Faces	5.80E+04	5.37E+03	2.62E+04	faces
Tube	3.76E+05	4.32E+05	7.38E+05	cells
Inlet	2.24E+02	2.24E+02	3.04E+02	faces
Interface	9.41E+04	1.08E+05	1.84E+05	faces
Outer Wall	9.41E+04	1.08E+05	1.84E+05	faces
Outlet	2.24E+02	2.24E+02	3.04E+02	faces
Total Cells	**2,315,956**	**3,781,034**	**6,534,463**	
Total Boundary Faces	**944,971**	**1,001,967**	**1,704,939**	

Table 6 Characteristics of generated meshes

In brief, there are two main limits in choosing the base size of cells in meshing any turbulent flow field. The upper limit is imposed by Y+ which is a direct function of the near wall cell size and should be greater than 30 and less than 200 in a wall function type mesh and should not exceed 1 in a low Reynolds number type mesh [87]. Hence, to analyze a turbulent flow using k-ε model the meshes cannot be so coarse that Y+ exceeds 200. On the other hand, the

lower limit of cell base size is imposed by the memory capacity and CPU time both of which are direct functions of number of cells.

Figure 48 demonstrates the axial velocity and the temperature distribution along the vertical line in the center of receiver predicted by these three meshes in noon July 11th, 2005. It should be noted that none of the profiles reach the surface of the receiver tube because the flow field data are stored in the center of each cell.
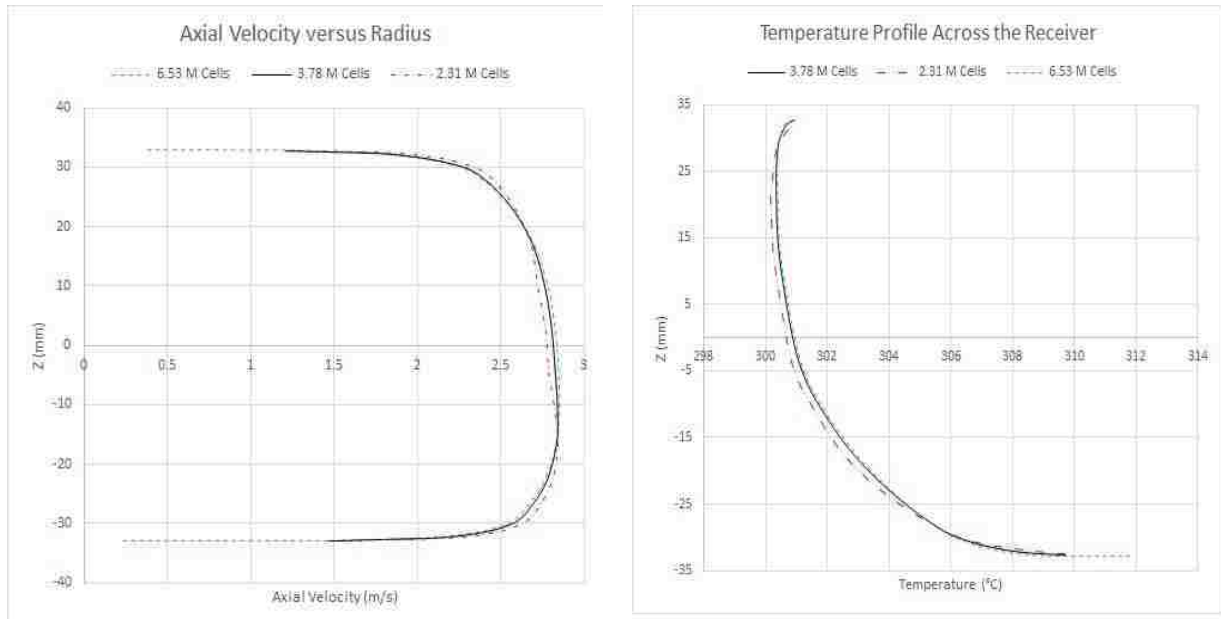
Figure 43 Axial velocity profile and temperature in the middle cross section of receiver on vertical.

Comparing the profiles predicted by the coarse mesh with the fine mesh predictions show that the coarse meshes estimate lower velocities and temperatures in the core of receiver and higher values in near wall regions. This difference might be the result of higher Y+ values with coarse mesh which weakens the software capability in capturing the velocity gradient in boundary layer and hence roughly estimates the shear stress in that region. Expectedly, to compensate the increase of flow rate due to higher velocities in near wall region, the velocity in the core region decreases so that the continuity law is not violated. Similar pattern is seen in comparing the profiles generated by medium size meshes with the fine meshes. However, the differences between these profiles are so small that the graphs are barely distinguishable. In fact, adding 72.8 % more cells and 70.1 % more boundary faces improves the estimation of velocity field only 1.2 %. Hence, using such a fine mesh to generate the results is not feasible. To summarize, in this research, a mesh consisting of 3,781,034 cells and 1,001,967 boundary faces is used. The base size of the mesh is 2.7 and its growing ratio is 1.3.

4.2   Verification of Numerical Simulation

In order to verify the numerical simulation, the experimental investigations conducted by Timothy A. Moss, and Doug A. Brosseau in Sandia National Laboratories [86], are simulated. Moss and Brosseau used a LS-2 collector with Schott PTR 70 HCEs (Heat Collector Element). The geometry of SNL system was pretty much the same as one described earlier in chapter 3 except that the SNL system is equipped with a continuous 2D tracking system to maximize the solar incidence on the collector. Moreover, Moss and Brosseau didn't use the flow rates that are usually used in the solar thermal power plants like SEGS plants. Instead, they reduced the flow rate through the HCE to about 55 lit/min which is about one tenth of the real flow rate in power plants like SEGS. To compensate for the lower flow rates a specially constructed plug was inserted down the full length of HCEs. The plug was made of a 50.8 mm diameter 304 SS tube. Figure 30 demonstrates the cross section of Schott PTR 70 HCE with the plug inserted in. Appendix F Summarizes the geometry of test set up.

The peak efficiency of LS-2 collector and Schott HCEs were measured. All tests were conducted around noon and the results were averaged. Therefore, the incidence angle for 2D tracking collector in all cases were near zero. DOW Corning Syltherm 800 was used as the heat transfer fluid (HTF) at elevated fluid temperatures, approaching 400˚C while at near ambient fluid temperatures, the working fluid was replaced with water.

Appendices D and E summarize the thermal properties of Syltherm 800 and water respectively within the temperature ranges used by Moss and Brosseau. The latter is generated using REFPROP software from NSIT [90, 81].
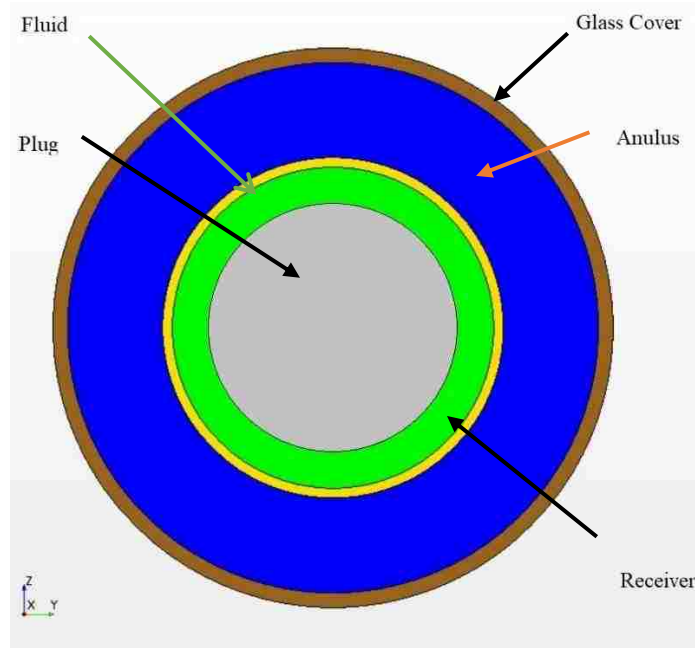
Figure 44 Cross Section of Sandia National Laboratories Receiver with Plug Inserted in.

Moss and Brosseau repeated the tests 24 times for the inlet temperatures ranging from 21.35 to 362.97 ℃. Only five tests among all their tests are chosen and simulated. A summary of these five tests is presented in table 8 along with the results of numerical simulations.

Comparing the results of computational analysis with Moss and Brosseau shows that the numerical simulation overestimates the outlet temperature of HTF and consequently the thermal efficiency in all cases. However, the declination from the experimental data is comparable to the uncertainty of the experiments. The most accurate result with only 0.51 % error is obtained with the lowest inlet temperature where water is used as the working fluid. By increasing the inlet temperature, the percentage of error in estimating the efficiency increases up to 4.01 % at T_{in} = 199.56 °C and then decreases again to 1.64% at T_{in} = 361.97 °C. In comparison with the uncertainty of each experiment the worst estimation occurs in case 3 with 2.45% error above the uncertainty of the experiment. However, even in this case the numerical simulation provides acceptable results.

In addition to the general errors of computational analysis, several other factors contribute to the overestimation of computational analysis.

Table 7 Summary of Verification Results

Tested conditions	Average NIP	Average Ambient Air Temp	Inlet Temp.	Outlet Temp.	Ave. HCE fluid Temp. Above Ambient	Average Flow Rate	Average Measured Efficiency		Ave. Wind Speed	Outlet Temp	Error in outlet temp.	Thermal Efficiency	Error in Efficiency
	W/m2	°C	°C	°C	°C	gal/min	%	± %	MPH	°C	°C	%	%
Case 1	999.45	17.98	21.35	33.13	9.26	9.95	78.6	2	4.5	33.19	0.06	79.00	0.51
Case 2	1029.05	6.38	100.02	121.98	104.62	14.34	74.2	1.61	3.1	122.68	0.70	76.57	3.19
Case 3	1051.08	5.83	199.56	221.28	204.59	14.27	70.1	1.56	5.3	222.15	0.87	72.91	4.01
Case 4	953.29	7.63	298.27	318.2	300.61	14.45	67.6	1.59	3	318.84	0.64	69.77	3.21
Case 5	1015.78	11.98	362.97	384.92	361.97	14.35	64.3	1.47	7.9	385.28	0.36	65.35	1.64
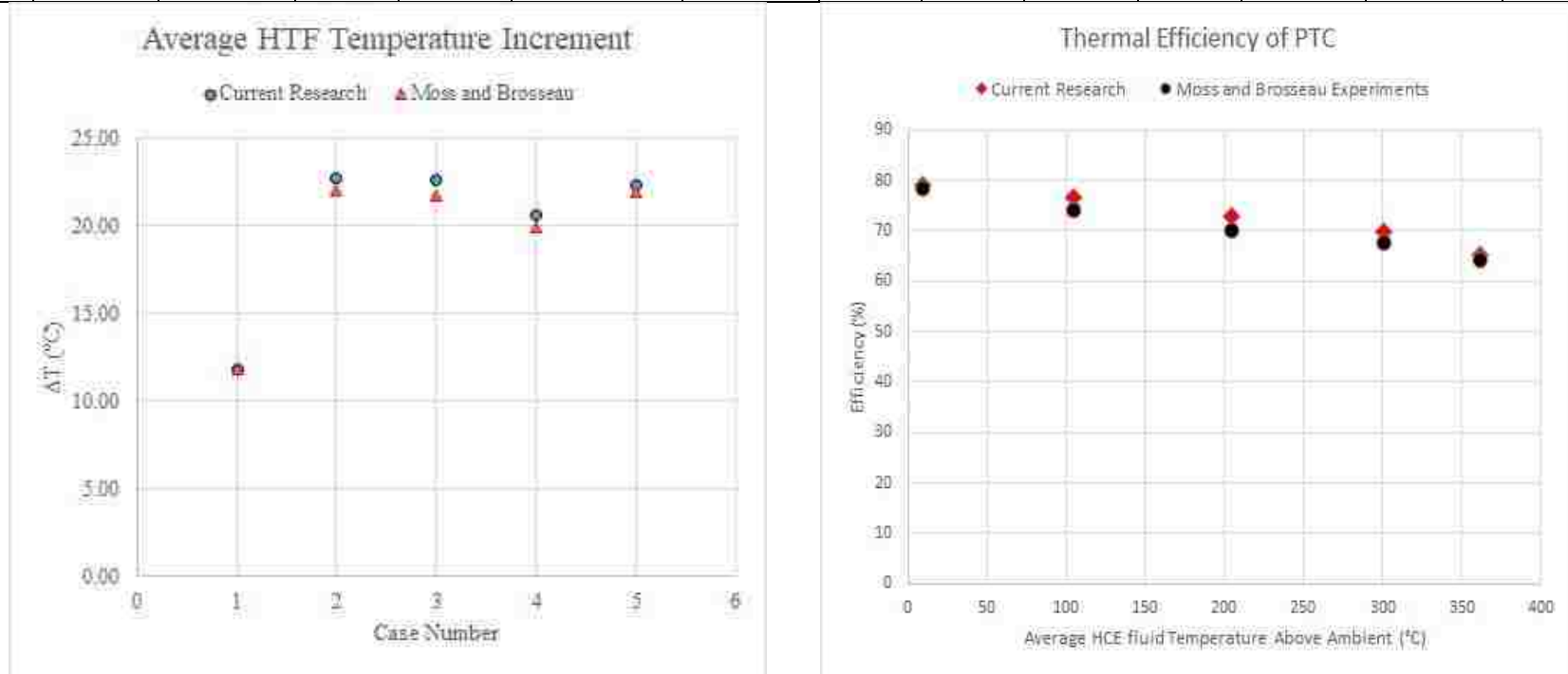
Figure 45 Comparison between the outlet temperature and the thermal efficiency predicted by this research and Moss and Brosseau Experiments

67

- Sky is considered clear. Although Moss and Brosseau has tried to conduct the experiments in the clearest sky but in practice there is no perfectly clear sky [86].

- Brackets that contribute in heat loss to the ambient are neglected.

- Wind effect is modeled roughly because CCM+ software is not capable of imposing several convection coefficients on one region. So convective heat loss of both the cover glass and the reflector are estimated roughly.

- Dust and imperfections of surfaces are not addressed.

- Although multiband radiation model is implemented, it still cannot estimate the absorbance and reflectance of solar irradiance completely for it models the spectral behavior of materials as a step function.

- Physical properties of glass cover and selective coating are indeed temperature-dependent. However, in this research their variations are not addressed.

- The reflector is considered a single piece of mirror whereas in practice, it consists of several smaller pieces of mirrors assembled to form a big reflector. There are small gaps between adjacent pieces and mismatch in aligning the mirrors practically. Especially, there is a big gap in the center of reflector parallel to its axis. In an East – West oriented single axis tracking collector this gap is always shadowed by the receiver tube. Hence, it is neglected in this research along with all other gaps and possible misalignments.

- Extension bellows are replaced with adiabatic boundaries at either of ends of receiver.

- The near vacuum condition inside annulus is replaced with a low-pressure hydrogen because the CCM+ software cannot model radiation transmission in a media surrounded by vacuum regions on both sides.

- The deflection of receiver due to its weight and thermal expansion is neglected. The same goes with the glass cover and the reflector.

Most of these simplifications lower the heat loss and tend to increase the thermal efficiency. Hence, it is understandable that this numerical simulation a little bit overestimates the thermal efficiency of parabolic trough collector especially in higher temperatures.

After assuring that the numerical method is able to predict the efficiency and outlet temperature of the parabolic trough collector accurately, it was applies on S-CO_2 at a set of constant inlet conditions during a summer day. Table 8 summarizes the main features of boundary conditions and computational results at each time step. In addition, following

graphs illustrate the main characteristics of flow field at 2 PM as a sample of the flow field during a summer day.

4.3   Solar Irradiation

TMY3 data are used to calculate total solar irradiance at each time-step. Then using the mass flow averaged temperature of S-CO₂ at the outlet, the amount of energy absorbed by the fluid is computed. Although the inlet temperature is constant and the thermal efficiency of PTC varies slightly, the total amount of absorbed energy and consequently the outlet temperature varies vastly over the time. At 8:00 AM when the thermal efficiency set its highest level at 70.45 %, the direct solar irradiance is in its lowest level at 740.43 W/m^2 and the difference between inlet and outlet temperature of receiver is only 8.69 °C. In contrast, At 12:00 PM the thermal efficiency decreases to its lowest level at 68.77 % while the direct solar irradiance experiences its maximum at 1286.21 W/m^2 and the difference between inlet and outlet temperature of receiver reaches to its peak at 24.52 °C. Regarding the fact that different terms of heat loss are almost constant during this summer day, the dominant parameter in determining the variation in thermal efficiency of HCE is most likely the difference between the sky temperature and the average receiver temperature which in turn determines the heat loss due to emission to the sky. In brief, while from 8 AM to 12 PM the thermal efficiency drops less than 2.4 % the difference between inlet and outlet temperature of receiver shows a dramatic grow of over 182 %.
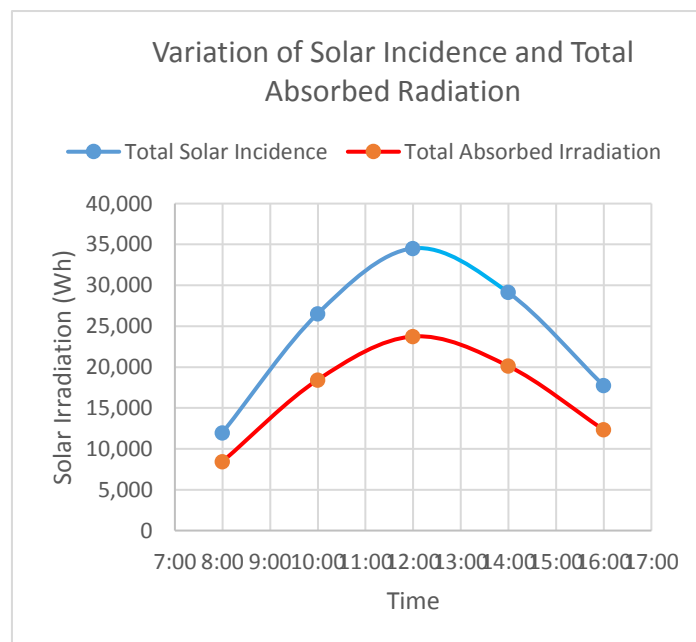
Figure 46 Variation of Solar Irradiance and Total Absorbed Radiation

69
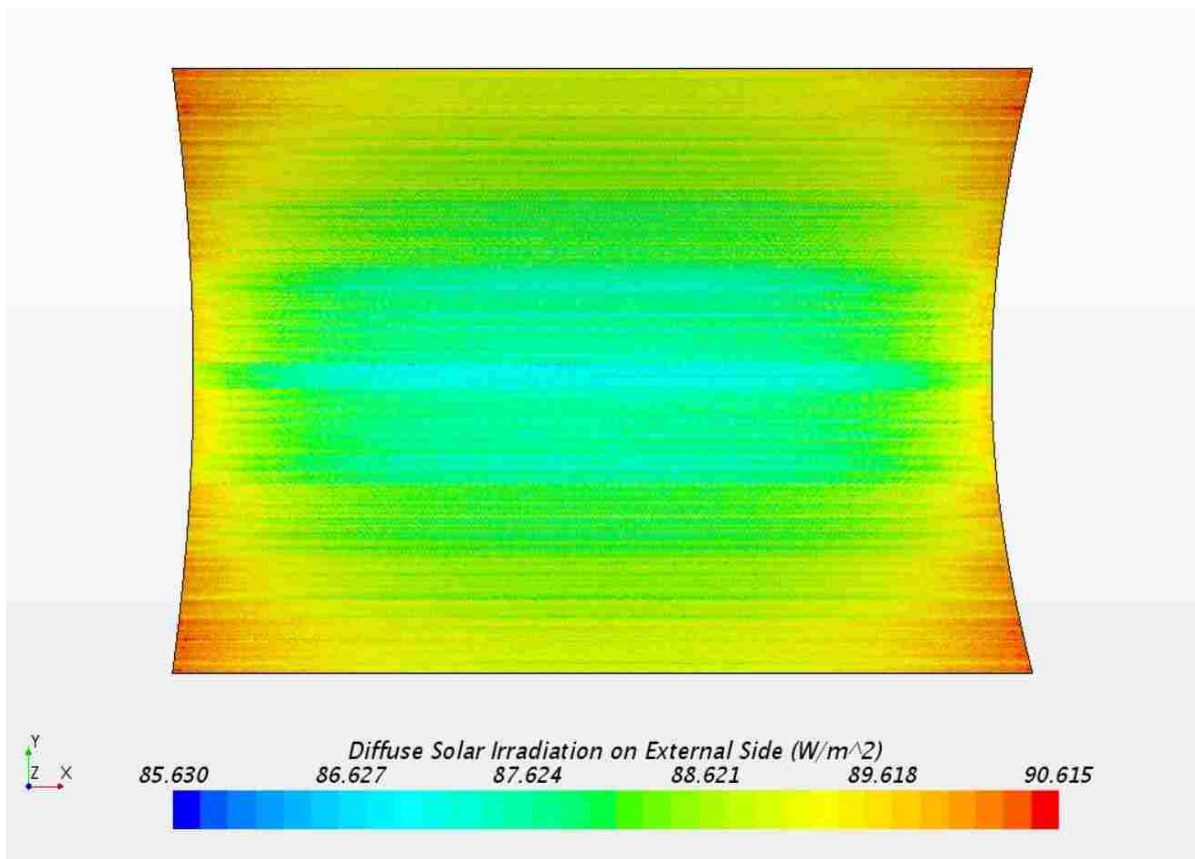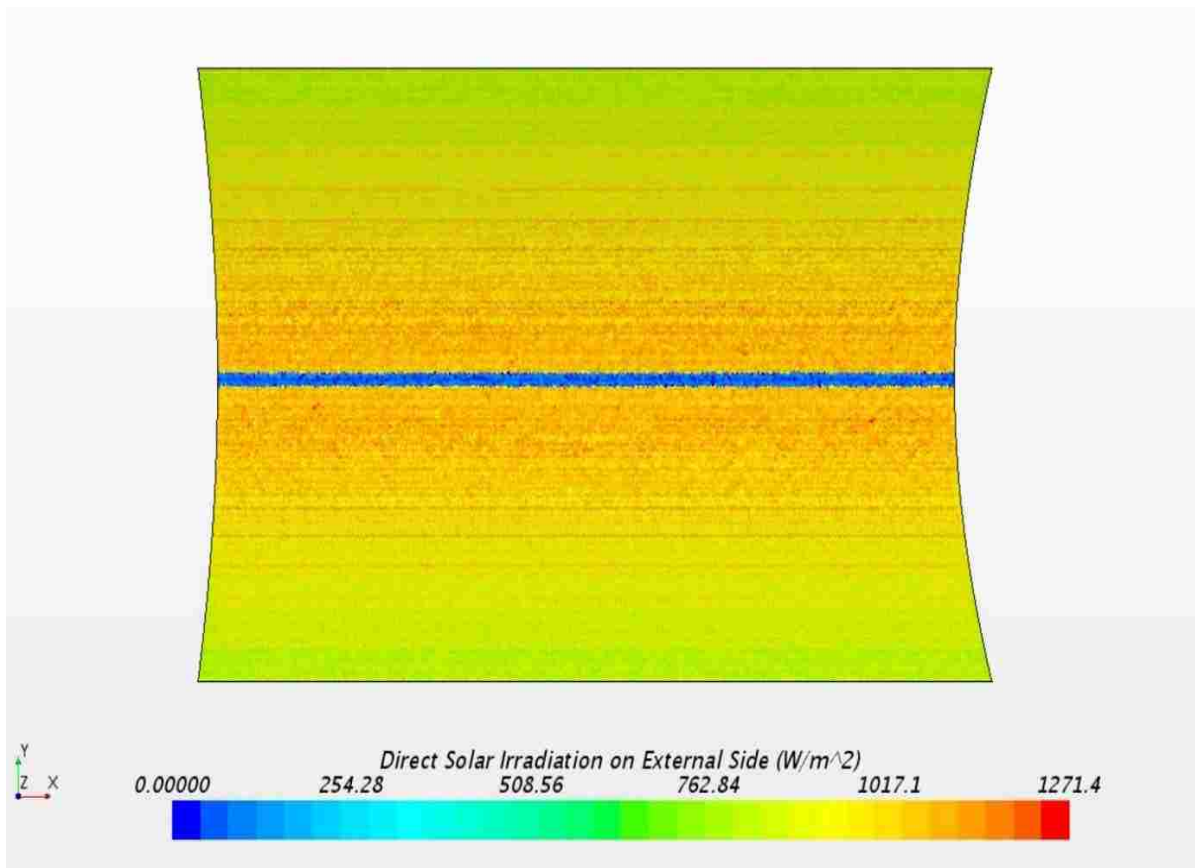
Figure 47 Direct and Diffuse Solar Irradiation on the Reflector

70

Site Location	Albuquerque, NM	ρ_{in} (kg/m3)	95.03
Date	7/11/2005	Cp_{in} (J/kgK)	1153.35
Inlet Pressure (Mpa)	10	Thermal Conductivity$_{in}$ (mW/m.K)	42.47200
Flow Rate (Lit/min)	530	Dynamic Viscosity$_{in}$ (μPa.s)	28.01
T_{in} °C	300	Mass Flux (kg/s)	0.839
V_{in} (m/s)	2.582	Re	578,183

Time	V_{wind} (m/s)	Azimuth (deg)	Altitude (deg)	G_b (Wh/m^2)	Direct Solar Flux (W/m^2)	Diffuse Solar Flux (W/m^2)	Rotation around E-W axis	R_b	Total Solar Incidence (Wh)	$T_{ambient}$ (°C)	T_O (°C)	ΔT (°C)
8:00 AM	3.6	85.46	34.07	356	740.43	72	55.93	0.86	11,940	24.4	308.69	8.69
10:00 AM	5.2	105.43	58.42	701	1125.87	106	-31.58	0.97	26,519	25.8	319.03	19.03
12:00 PM	5.2	167.78	76.71	894	1286.21	136	-13.29	0.99	34,517	30.6	324.52	24.52
2:00 PM	3.6	248.28	63.08	786	1178.33	154	-26.92	0.95	29,121	32.2	320.79	20.79
4:00 PM	5.2	271.22	38.97	562	831.11	107	51.03	0.81	17,754	33.3	312.75	12.75

Time	Efficiency (%)	Q'_{absorb} (Wh)	Ave. HCE fluid Temp. Above Ambient (°C)	ρ_{out} (kg/m^3)	Cp_{out} (J/kg.K)	Thermal Conductivity$_{Out}$ (mW/m.K)	Dynamic Viscosity$_{Out}$ (μ Pa.s)	T_{dp} (°C)	T_{sky} (°C)	h_{cover} (W/m^2. K)
8:00 AM	70.45	8,412	279.94	93.32	1,154.04	43.10	28.31	12.8	6.63	14.67
10:00 AM	69.47	18,422	283.71	91.37	1,155.17	43.85	28.68	13.3	8.28	11.96
12:00 PM	68.77	23,737	281.66	90.36	1,155.89	44.24	28.87	12.8	12.46	16.23
2:00 PM	69.12	20,129	278.20	91.04	1,155.39	43.97	28.74	11.1	12.81	11.74
4:00 PM	69.50	12,339	273.07	92.54	1,154.45	43.39	28.46	8.3	11.99	20.53

Table 8 Summary of Computational Analysis Results for LS-2 Collector Schott PTR 70 HCEs Carrying Supercritical CO₂

4.4 Heat Flux on Fluid-Receiver Interface

The heat flux graph looks puzzling at the first glance and needs to be interpreted. The key point in interpreting this graph is that the upper half of the receiver emits more heat to the sky than it receives from the sun for the temperature of the sky is about 20 degrees less than ambient while that of cover glass is well above the ambient. Some researchers even suggest filling the upper half of the annulus with insulator to lower the heat loss on the upper side.

In addition, following the general rule in mathematics of vector fields, CCM+ software considers the flux direction towards outside positive and towards inside negative. Hence, on the upper surface where the heat emits to the ambient the heat flux is positive while on the lower surface where the heat is absorbed from the collector (and heat flux is toward inside) the negative numbers appear.

Given that, reviewing the heat flux graph (figure 53) shows that a highly non-uniform heat flux exists around the receiver. While the lower half of HCE absorbs the concentrated solar irradiation, the upper half emits a small portion of it to the ambient. A very small region on the lower surface of either ends of receiver emits heat with fluxes up to 10,731.3 W/m^2 which is about three times more than heat loss flux on the upper surface. This is the region that neither receives the direct solar irradiance nor the radiation reflected by the reflector. Around sunset and sunrise when azimuth angle increases this shadowed region expands more.
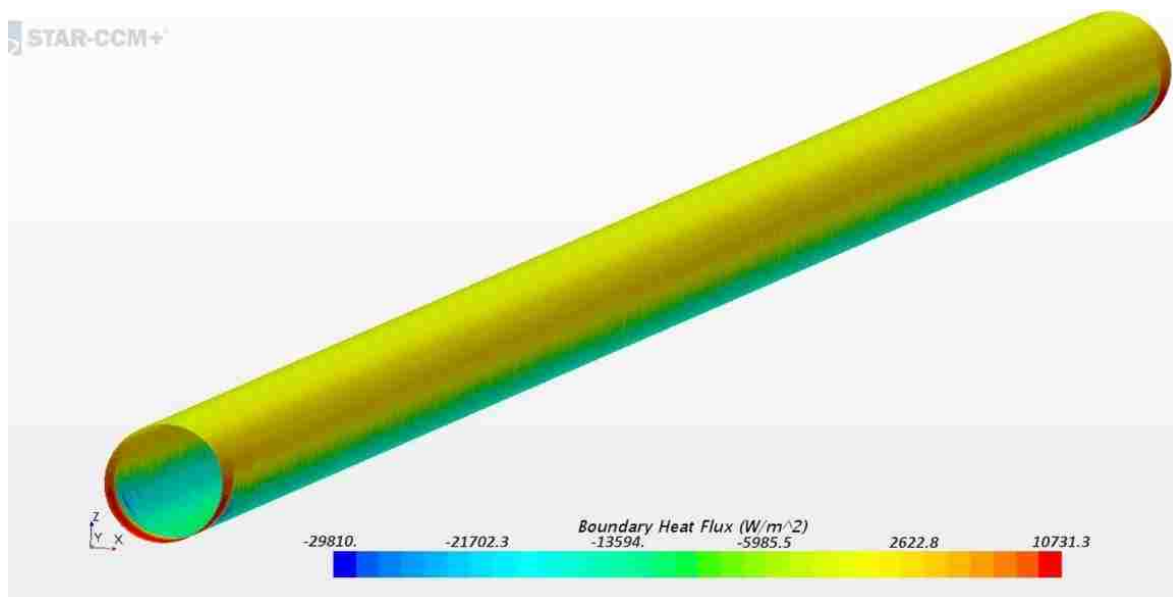
Figure 48 Heat Flux on Fluid-Receiver Interface

72

4.5 Temperature Distribution
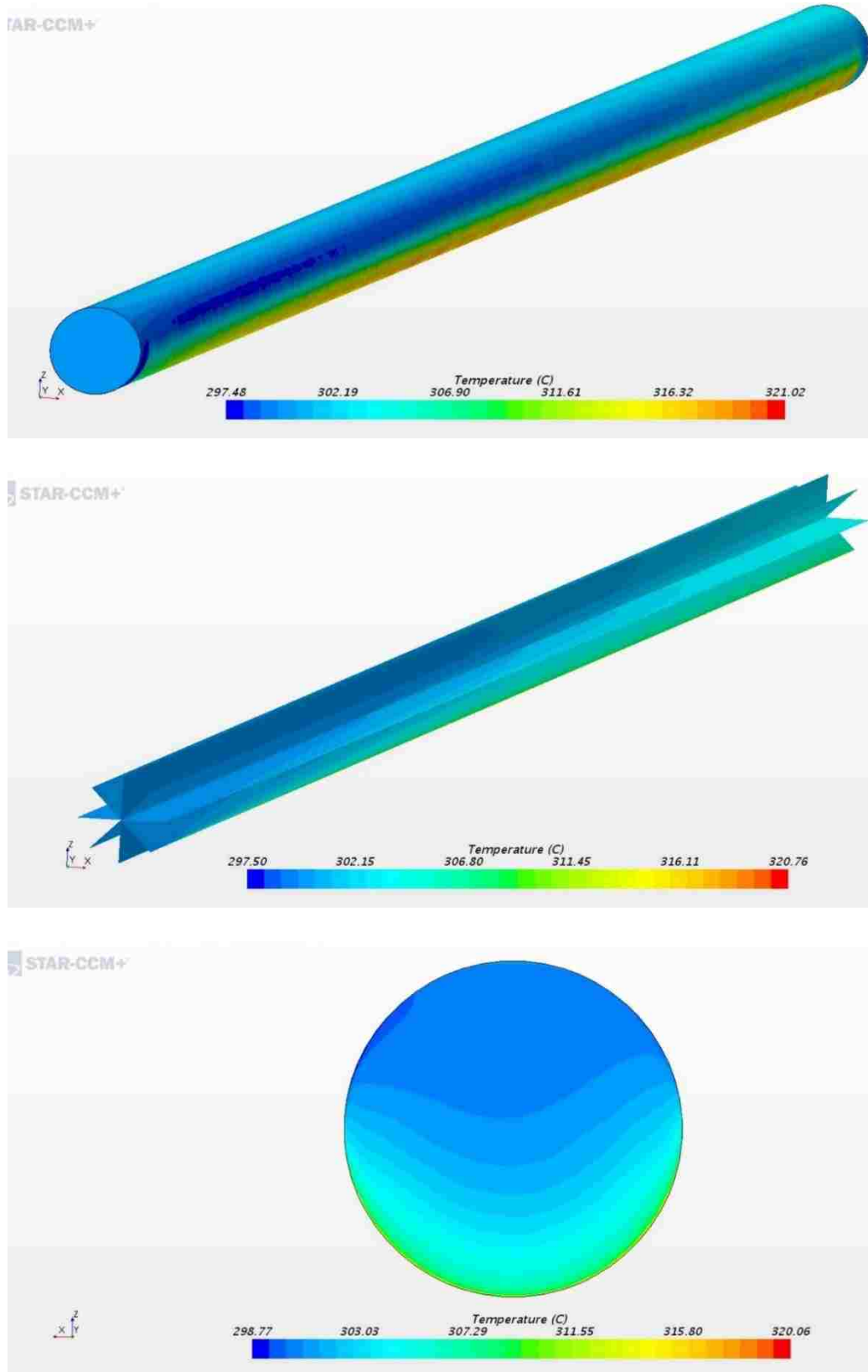
Figure 49 Temperature Distribution

4.6 Variation of Thermodynamic Properties of Supercritical CO_2

Density
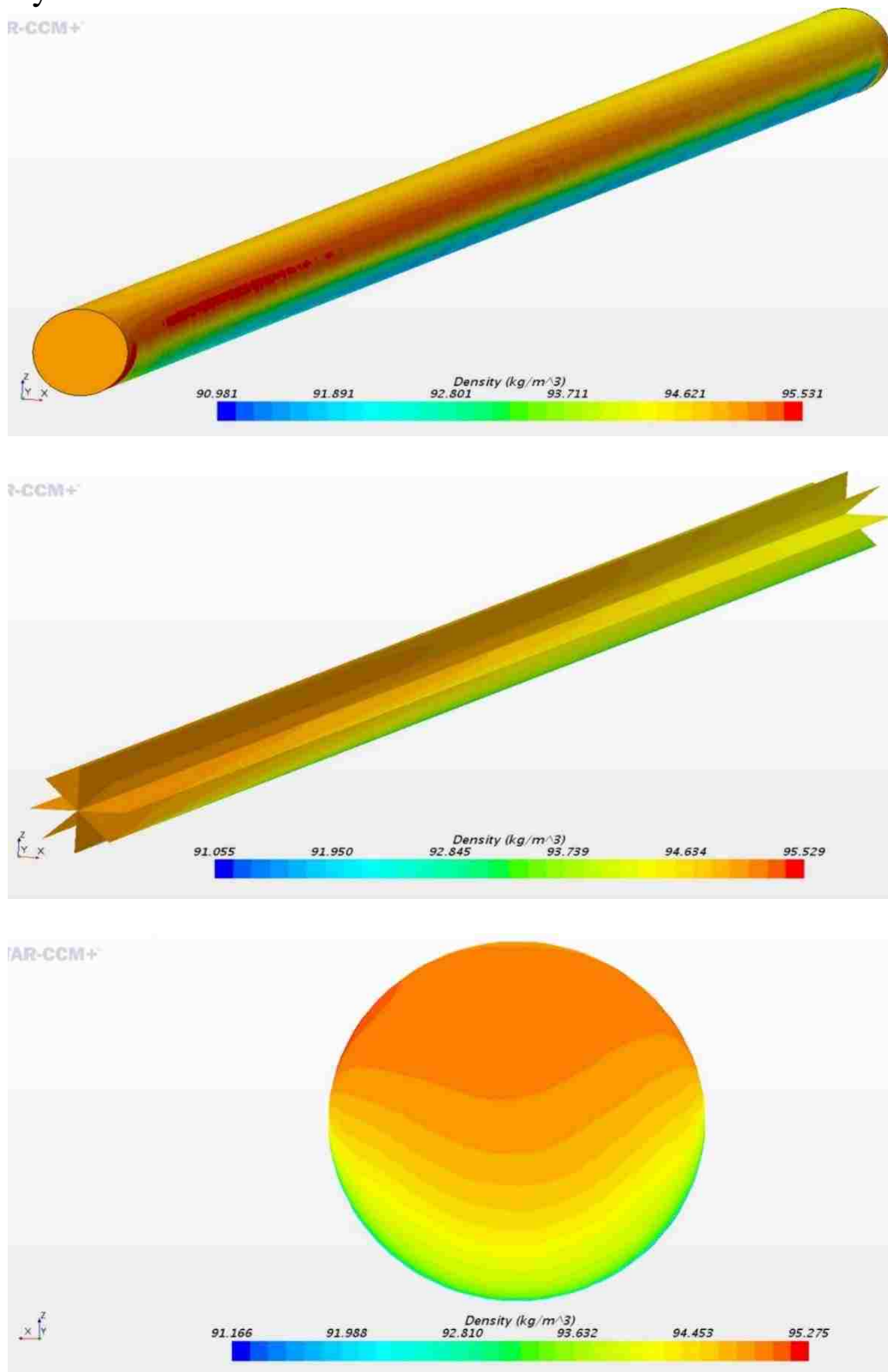
Figure 50 Variation of Density

Dynamic Viscosity
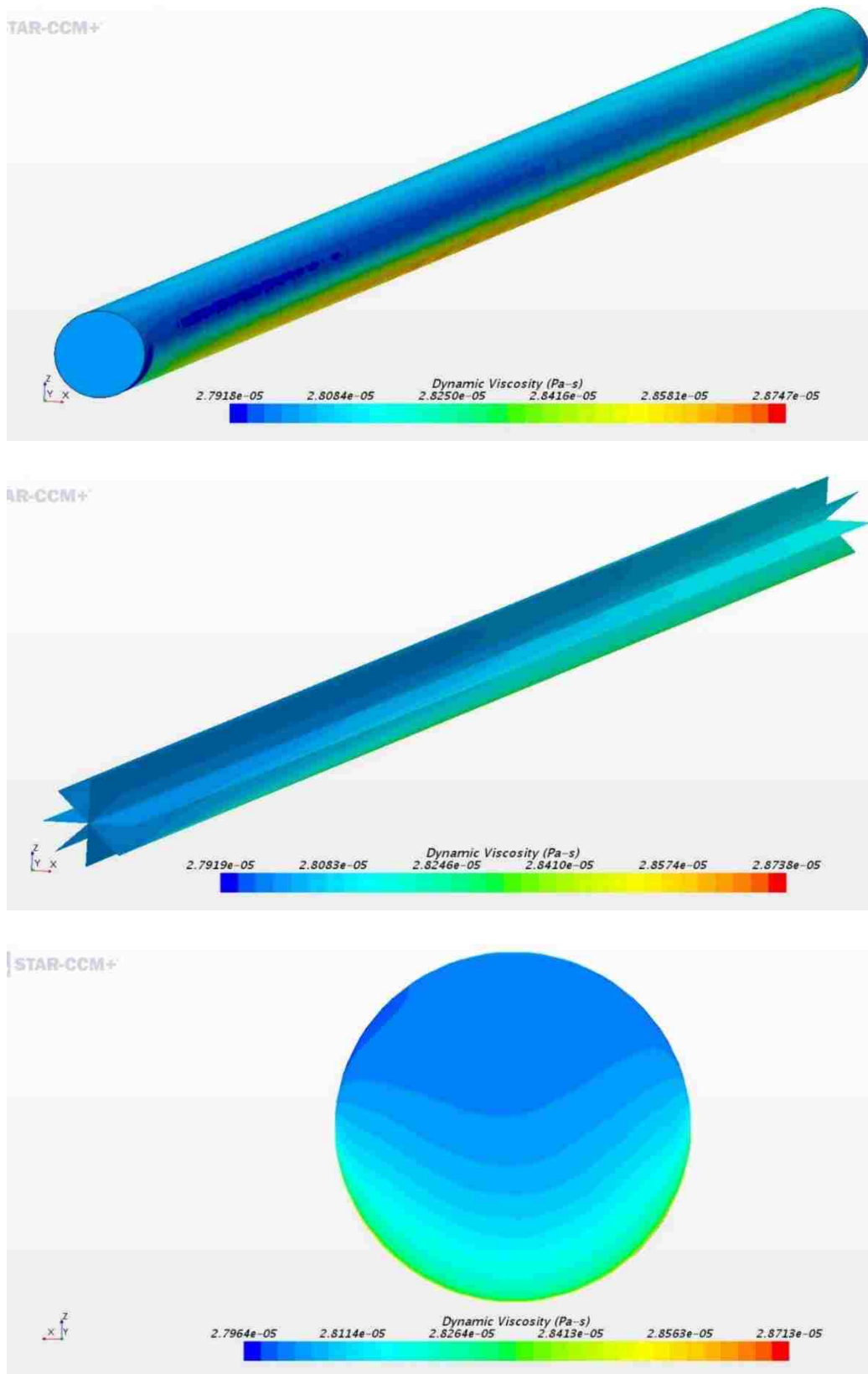
Figure 51 Variation of Dynamic Viscosity

Specific Heat
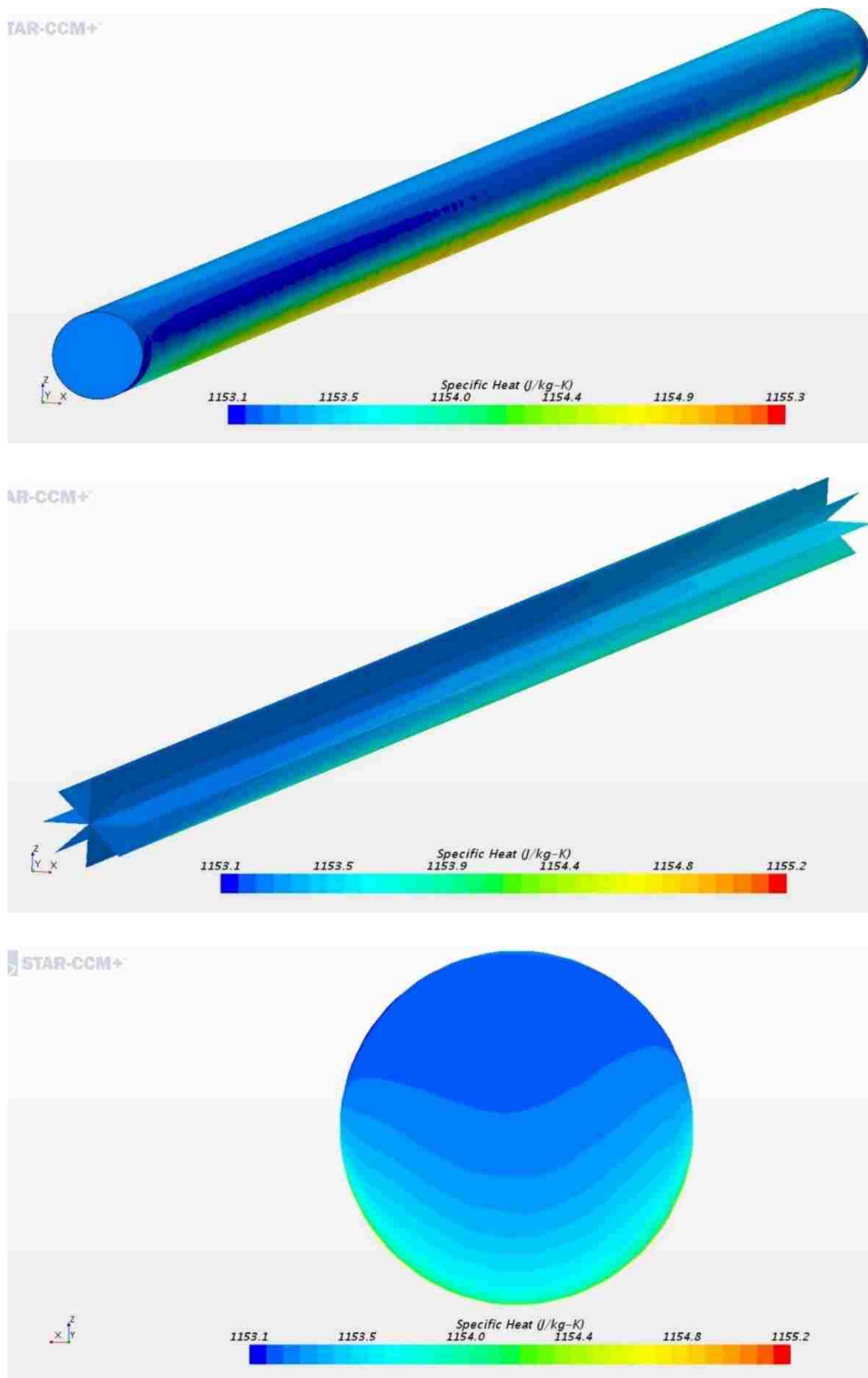
Figure 52 Variation of Specific Heat

4.7   Velocity Contours
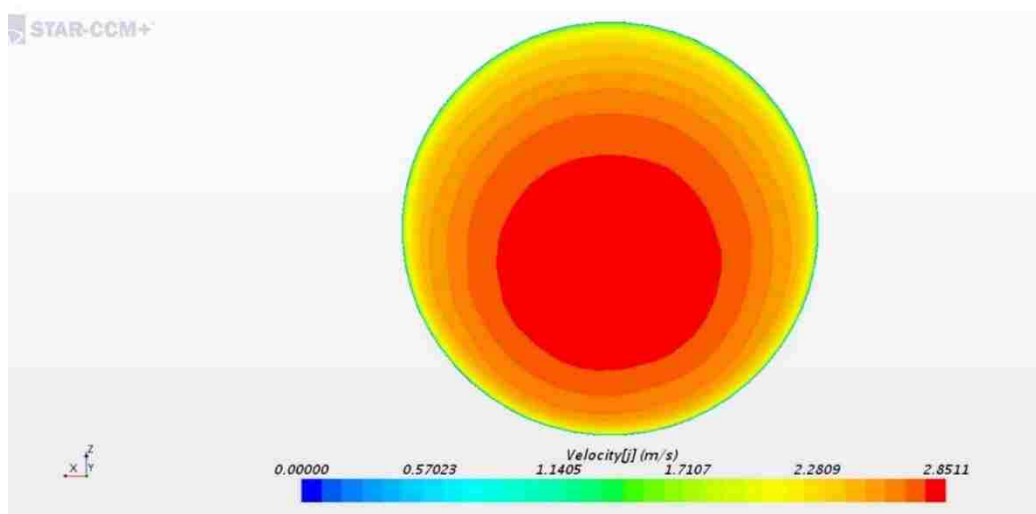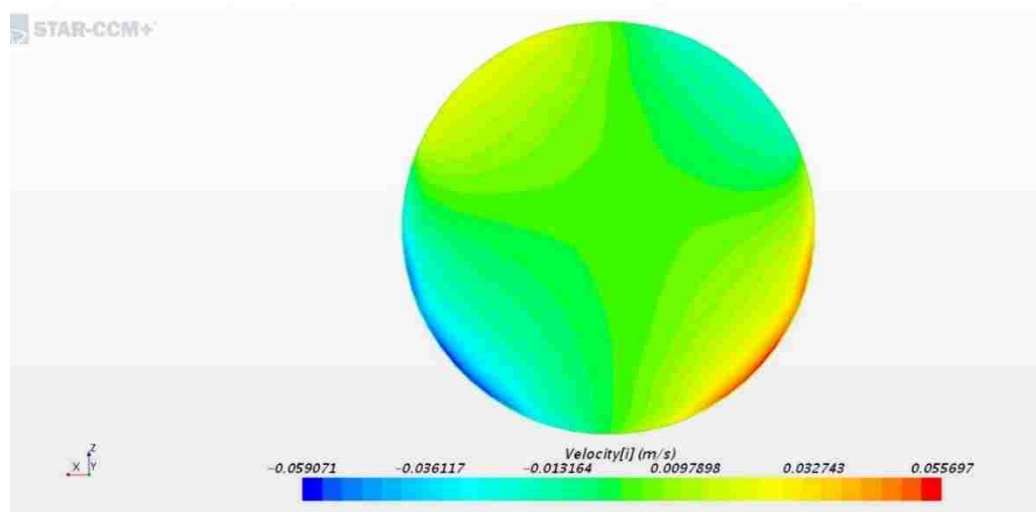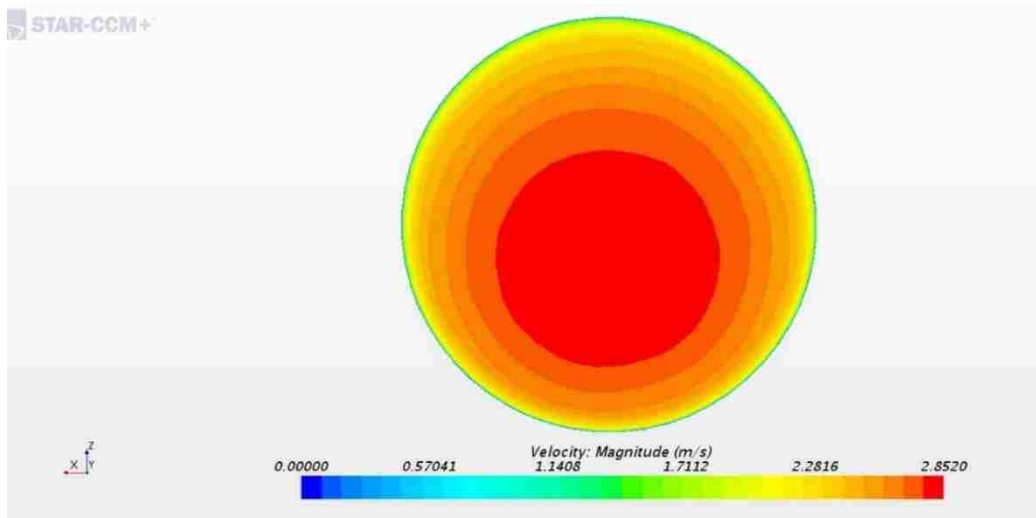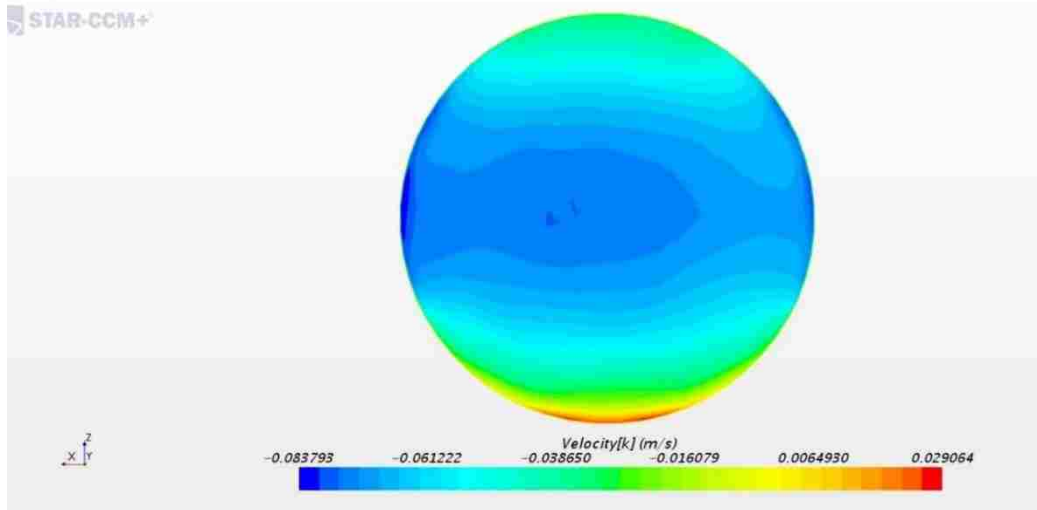
Figure 53 Velocity Contours

4.8   Pressure Distribution
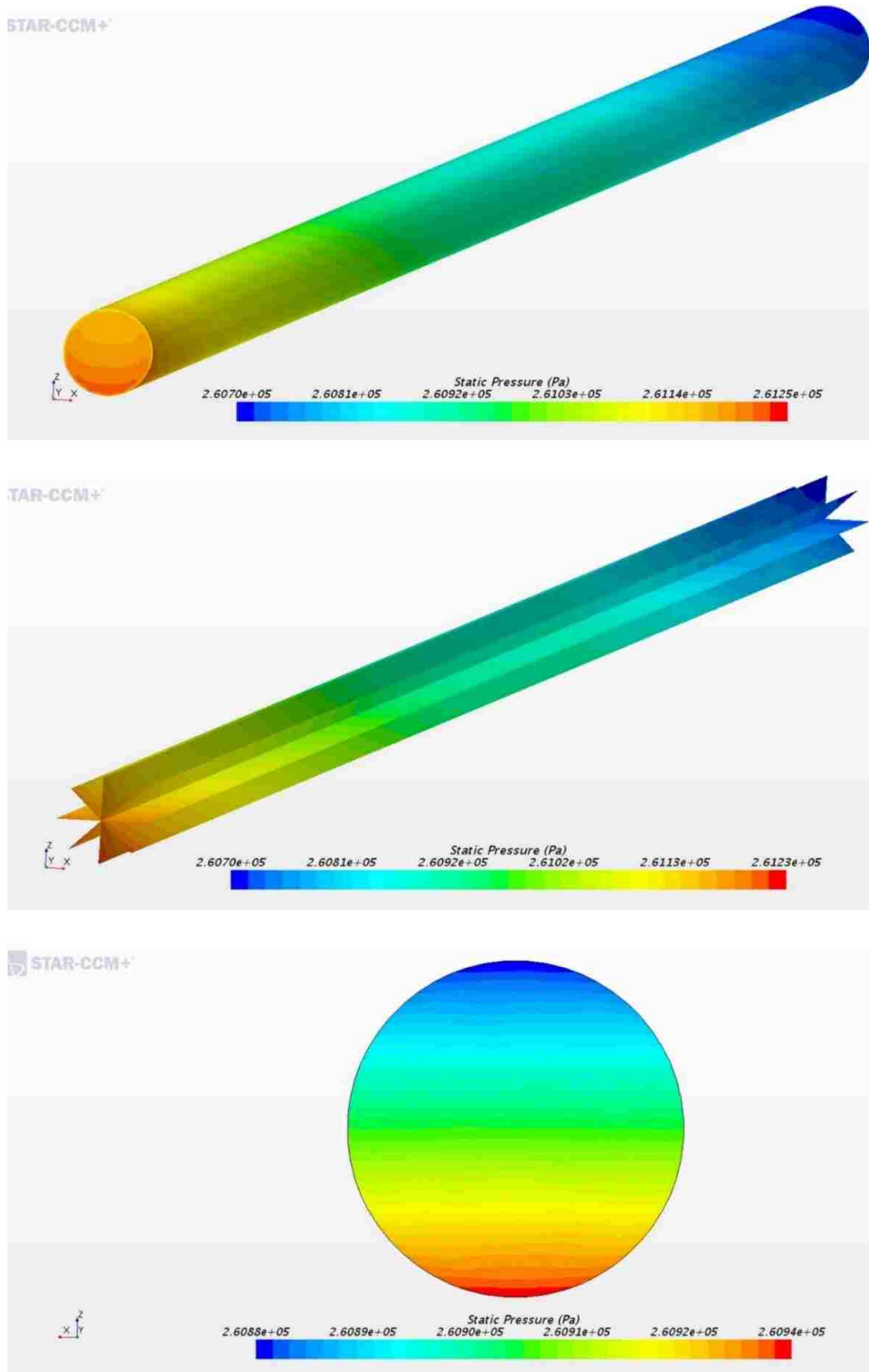
Figure 54 Pressure Distribution

Chapter 5: Conclusion and Recommendations

5.1 Conclusion

In this dissertation a comprehensive three-dimensional numerical simulation of flow field and heat transfer on the full-scale model of a parabolic trough solar collector of a direct Super Critical Carbon Dioxide (S-CO2) Brayton cycle is performed.

This research considers both the non-uniform solar irradiance on the Heat Collector Element (HCE) and the natural convection inside the receiver tube combined with the nonlinear variations in the physical properties of S-CO2.

The validation of the numerical simulation is checked by regenerating the results of a given experimental LS-2 PTC system, including the temperature increment in the receiver tube and thermal efficiency of PTC. The validation analysis shows that this numerical simulation always tends to slightly overestimate the efficiency of parabolic trough solar power plant. While the overestimation is in the range of uncertainty of experimental investigations in the morning and in the afternoon, its error margin increases around solar noon up to 2.45 % above the uncertainties. The possible origins of this overestimation are discussed in detail.

To avoid applying simplified thermal boundary conditions on the heat collecting element, the solar radiation is computed and then through simulating the concentration of solar irradiance on HCE the accurate heat flux on the HCE is calculated. In addition, a system of convection heat transfer, sky radiation, adiabatic boundary condition, and environmental boundary condition are applied on appropriate boundaries. For the first time in this research the variation in the properties of S-CO2 inside the receiver are presented. Also, more details of the characteristics of coupled heat transfer and the flow field inside the receiver is presented and discussed. It is shown that significant fluid property variations exist inside the tube and have a substantial effect on the flow field and heat transfer throughout the receiver.

In addition, to investigate the variations in the efficiency and outlet temperature of the receiver during a typical summer day a pseudo steady state scheme is applied. Given that the variations in ambient conditions are at least two degrees of magnitude slower than the variations in the flow field, in each time step the flow filed is considered to fulfill the steady state conditions. Therefore, the steady state numerical analysis is applied for five time-steps (8 AM, 10 AM, 12 PM, 2 PM and 4 PM) in a typical summer day. At each time-step the ambient conditions are calculated and applied as boundary conditions. Also, to build a more realistic model of a solar

thermal power plant, the single axis East-West oriented collector is rotated at each time step to minimize the angle of incidence.

The solar incidence, total absorbed heat, outlet temperature of the receiver and thermal efficiency of PTC are graphed. A curve is then fitted to each graph to let the user interpolate the conditions in between time steps. The thermal analysis of the system showed that although the efficiency of PTC during a typical summer day is almost constant, its outlet temperature varies dramatically due to the variation in the total solar incidence and a number of other minor factors that contribute in decreasing the radiation absorbance of the receiver.

5.2 Suggestions for future studies

The following recommendations are suggested for further research in this area:

- Since there are large temperature gradients across the receiver tube, applying heat augmentation methods is expected to enhance the thermal efficiency of Parabolic Trough Collector.
- In all cases that are studied in this research the heat loss from the upper half of the HCE, mainly due to emittance to the sky and convection on the glass cover, is more than the absorbed solar irradiance. Hence, the heat transfer from the upper half of the receiver decreases the thermal efficiency of HCE. The situation is expected to be even worse in higher inlet temperatures, and consequently the higher average temperature, of HCE for as the average temperature of HCE increases the amount of heat emittance to the sky increases. Hence, insulating the upper half of the heat collecting element is expected to enhance the efficiency. In addition, such an HCE is expected to be less expensive than the conventional HCEs.
- Regarding the huge variations in the outlet temperature of the receiver it is necessary to combine parabolic trough S-CO$_2$ direct Brayton solar power cycle with a backup heating system or a thermal storage. Hence, new thermal storage systems are needed to be developed for direct S-CO$_2$ cycle. Adapting conventional systems for direct S-CO$_2$ cycles might be the first step towards developing such systems.
- To estimate the heat loss more accurately brackets and extension bellows should be added to the model. These elements contribute in heat loss to the ambient.

- The gaps between adjacent pieces of mirror and mismatch in aligning the mirrors should be considered in modeling. Especially, misalignment can intensely deteriorate the performance of system.

- The deflection of receiver due to its weight and thermal expansion adversely affects the performance of PTC. It might be very difficult, if not impossible, to build a numerical model that combines stress analysis of PTC with thermal-fluid analysis. Especially, because such a numerical simulation will be difficult to converge. However, it is possible to run stress analysis and thermal-fluid analysis separately and then import the output of each one of analysis into the other one to correct the previous results. This prediction – correction scheme should be repeated until both analysis converge.

- The flow field inside the annulus should be investigated thoroughly by implementing rarified gas models in near vacuum cases and by applying natural convection models in broken vacuum condition.

- The effects of incident angle on the refraction and transmittance of the glass cover should be considered. It is expected that large incident angles after sunrise and before sunset drastically increase the reflectance and consequently decrease the thermal efficiency of PTC.

- The variations in the physical properties of glass cover and its selective coatings and also cermet coating on receiver should be considered.

- The capabilities of multiband radiation model in estimating the radiation heat transfer can be improved by defining more bands. To do so, detailed experimental characterization of the physical properties of the glass cover and its selective coatings as well as the cermet coating of receiver are needed.

- Convection heat transfer, especially in windy days, is the dominant term in heat loss of heat collecting element. So, to predict the efficiency of system more accurately it is needed to replace the convection boundary conditions on the glass cover with the results of wind analysis. Actually, the solution field should be extended to cover the air surrounding the PTC.

Appendix A

Solar Radiation Data of Albuquerque, NM, USA

Time	GHI (W/m^2)	DNI (W/m^2)	DHI (W/m^2)	Dry-bulb (C)	Dew-point (C)	RHum (%)	Pressure (mbar)	Wdir (degrees)	Wspd (m/s)
1:00	0	0	0	22.8	12.8	53	841	180	4.1
2:00	0	0	0	22.2	12.8	55	841	180	4.6
3:00	0	0	0	20	12.8	63	841	110	3.6
4:00	0	0	0	20	12.8	63	841	110	2.6
5:00	0	0	0	21.1	12.8	59	841	170	3.6
6:00	43	0	20	21.1	12.8	59	842	180	3.6
7:00	209	574	49	23.9	12.8	50	842	200	2.6
8:00	428	756	72	24.4	12.8	48	842	210	3.6
9:00	636	841	91	26.1	13.3	45	842	190	4.6
10:00	807	884	106	27.8	13.3	41	842	170	5.2
11:00	885	856	113	28.9	13.3	38	841	140	2.1
12:00	1030	930	136	30.6	12.8	34	841	180	5.2
13:00	978	884	119	31.1	11.7	30	840	230	5.2
14:00	940	845	154	32.2	11.1	27	839	220	3.6
15:00	827	827	132	32.8	9.4	24	838	180	5.7
16:00	669	793	107	33.3	8.3	21	838	210	5.2
17:00	516	673	151	33.9	8.3	21	837	220	5.7
18:00	163	166	104	32.2	8.9	24	837	210	6.7
19:00	65	0	59	30	9.4	28	838	230	9.3
20:00	4	0	1	27.2	11.1	37	839	220	3.6
21:00	0	0	0	26.7	11.1	38	839	80	7.7
22:00	0	0	0	25.6	11.1	40	840	40	5.2
23:00	0	0	0	25	12.2	45	840	100	5.2
24:00:00	0	0	0	22.8	13.3	55	840	340	3.6

Table 9 Solar Radiation Data of Albuquerque, NM, July 11th, 2005, Adapted from TMY3 Databases

Appendix B

Characteristics of some refrigerants

Table 10 Characteristics of some refrigerants.

	Water	R-134a	R-407C[a]	R-410A[b]	Ammonia	Propane	CO_2
ODP/GWP[c]	0/0	0/1300	0/1600	0/1900	0/0	0/3	0/1
Flammability/toxicity	N/N	N/N	N/N	N/N	Y/Y	Y/N	N/N
Molecular Mass (kg/kmol)	18	102	86.2	72.6	17	44.1	44
Normal Boiling Point[d] (^{0}C)	100	-26.2	-43.8	-52.6	-33.3	-42.1	-78.4
Critical Pressure (MPa)	22.06	4.07	4.64	4.79	11.42	4.25	7.38
Critical Temperature (^{0}C)	373.9	101.1	86.1	70.2	133	96.7	31.1
Reduced Pressure[e]	2.77 E-5	0.07	0.11	0.16	0.04	0.11	0.47
Reduced Temperature[f]	0.42	0.73	0.76	0.79	0.67	0.74	0.9
Critical Density (kg/m^3)	322.1	545.63	0.511		235.29	220.36	422.7
Critical Specific Heat (kJ/kg.K)	1469800000[g]	592.47					952.38

a. Ternary mixture of R-32/125/134a (23/25/52, %)

b. Binary mixture of R-32/125 (50/50, %)

c. Ozone Depletion Potential / Global warming potential in relation to 100 years integration time, from the Intergovernmental Panel on Climate Change (IPCC).

d. ASRAE handbook 2001 fundamentals.

e. Ratio of saturation pressure at 0 ^{0}C to critical pressure.

f. Ratio of 273.15 K (0 ^{0}C) to critical temperature in Kelvin.

g. Cp_{cr} given from the NIST is unrealistically high probably due to limitations of numerical models used in NIST to accurately predict the high peak values. [81]

Table 10 is Adapted from [12, 13, 81].

Appendix C

Thermodynamic Properties of S-CO$_2$ at P= 10 MPa

Temperature	Density	C$_p$	Thermal Conductivity	Viscosity	Prandtl
^{0}C	kg/m^3	kJ/kg.K	mW/m.K	μPa-s	
100	188.56	1.5218	31.287	21.796	1.0602
110	176.97	1.432	31.235	21.902	1.0041
120	167.31	1.3672	31.39	22.077	0.96162
130	159.06	1.3189	31.683	22.301	0.92837
140	151.89	1.282	32.072	22.558	0.90174
150	145.56	1.2534	32.53	22.84	0.88003
160	139.92	1.2308	33.037	23.141	0.86214
170	134.84	1.2129	33.575	23.457	0.84738
180	130.23	1.1987	34.118	23.783	0.83556
190	126.01	1.1873	34.766	24.117	0.82363
200	122.13	1.1783	35.428	24.458	0.8134
210	118.55	1.1711	36.103	24.803	0.80456
220	115.22	1.1655	36.787	25.152	0.79688
230	112.12	1.1612	37.48	25.504	0.79017
240	109.21	1.1579	38.179	25.858	0.78426
250	106.49	1.1556	38.883	26.214	0.77905
260	103.93	1.154	39.592	26.57	0.77442
270	101.51	1.1531	40.305	26.926	0.77031
280	99.223	1.1527	41.02	27.282	0.76663
290	97.055	1.1527	41.738	27.638	0.76332
300	94.996	1.1532	42.457	27.994	0.76036
310	93.037	1.154	43.178	28.348	0.75768
320	91.171	1.1552	43.9	28.702	0.75525
330	89.389	1.1566	44.622	29.054	0.75305
340	87.685	1.1582	45.345	29.406	0.75105
350	86.055	1.1599	46.067	29.755	0.74922
360	84.492	1.1619	46.789	30.104	0.74755
370	82.992	1.164	47.511	30.451	0.74602
380	81.552	1.1662	48.232	30.796	0.74462
390	80.167	1.1685	48.952	31.139	0.74332
400	78.833	1.1709	49.671	31.481	0.74213
410	77.548	1.1734	50.388	31.821	0.74102
420	76.309	1.1759	51.105	32.16	0.74
430	75.113	1.1785	51.819	32.496	0.73905
440	73.958	1.1811	52.533	32.831	0.73816
450	72.842	1.1838	53.244	33.164	0.73733
460	71.762	1.1865	53.954	33.495	0.73656
470	70.716	1.1892	54.662	33.824	0.73583
480	69.703	1.1919	55.368	34.151	0.73515
490	68.722	1.1946	56.072	34.476	0.73451
500	67.77	1.1973	56.774	34.8	0.73391

Appendix D

Thermodynamic Properties of Syltherm 800

Table 11 Properties of Syltherm® 800 Heat Transfer Liquid [91]

Temperature (°C)	Specific heat (kJ/kg.K)	Density (kg/m³)	Thermal conductivity (W/m.K)	Viscosity (mPa.s)	Vapor pressure (kPa)
0.001	1.574	953.16	0.1388	15.33	0
40	1.643	917.07	0.1312	7	0.1
80	1.711	881.68	0.1237	3.86	1.46
120	1.779	846.35	0.1162	2.36	9.3
160	1.847	810.45	0.1087	1.54	35
200	1.916	773.33	0.1012	1.05	94.6
240	1.984	734.35	0.0936	0.74	204.8
280	2.052	692.87	0.0861	0.54	380.2
320	2.121	648.24	0.0786	0.41	630.5
360	2.189	599.83	0.0711	0.31	961.2
400	2.257	547	0.0635	0.25	1373
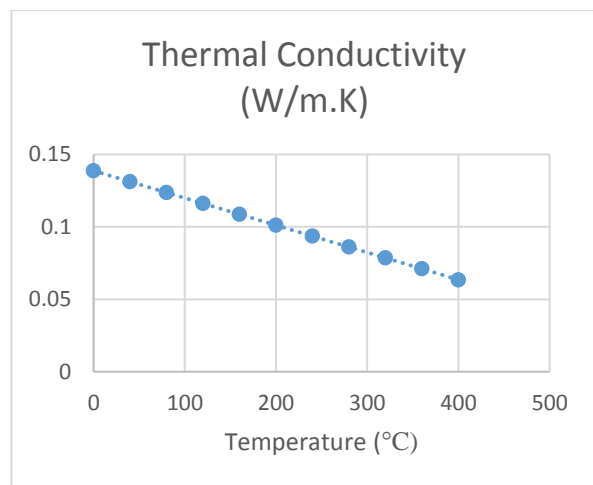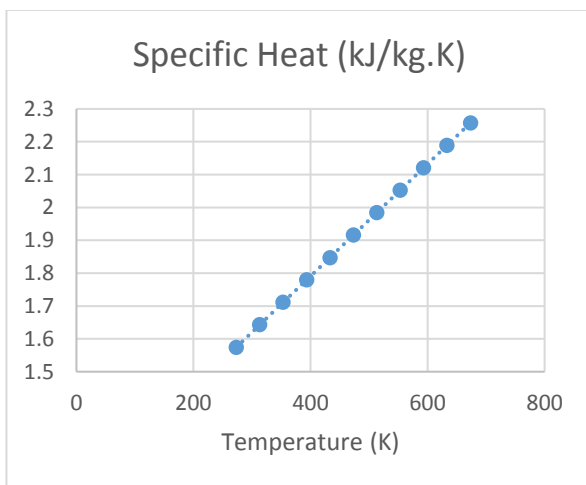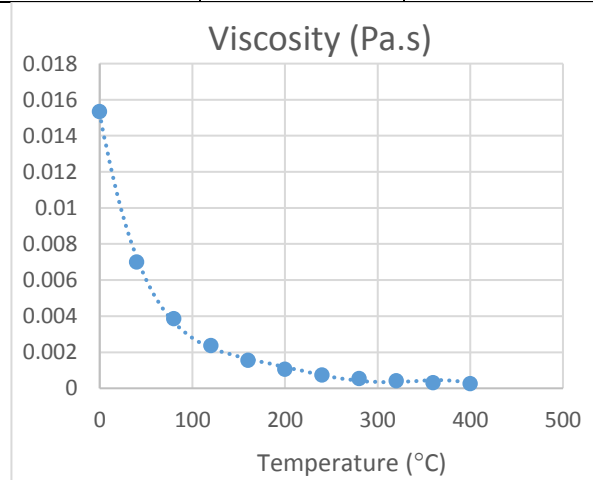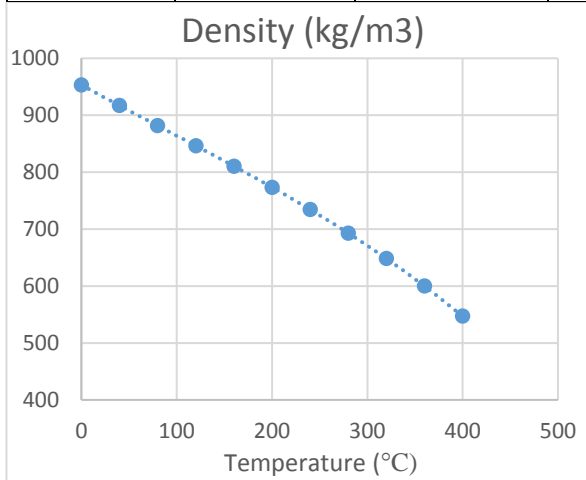
Appendix E

Thermodynamic Properties of Water at P=1atm

Table 12 Thermodynamic Properties of Water at P=1atm [90]

Temperature	Density	C_v	C_p	Therm. Cond.	Viscosity
(C)	(kg/m^3)	(kJ/kg-K)	(kJ/kg-K)	(mW/m-K)	(uPa-s)
1	999.9	4.2148	4.2161	558.18	1731
6	999.94	4.2022	4.2028	570.08	1471.5
11	999.61	4.1875	4.1936	580.85	1269.2
16	998.95	4.171	4.1874	590.71	1108.1
21	998	4.153	4.1834	599.77	977.54
26	996.79	4.1336	4.1809	608.14	870.11
31	995.34	4.113	4.1796	615.9	780.54
36	993.69	4.0914	4.1792	623.1	704.99
41	991.83	4.0688	4.1795	629.78	640.64
46	989.79	4.0454	4.1803	635.99	585.35
51	987.58	4.0213	4.1816	641.74	537.47
56	985.21	3.9966	4.1833	647.05	495.71
61	982.68	3.9714	4.1854	651.95	459.08
66	980	3.9458	4.1878	656.44	426.75
71	977.19	3.9199	4.1907	660.55	398.08
76	974.24	3.8938	4.1939	664.28	372.53
81	971.16	3.8676	4.1975	667.64	349.68
86	967.96	3.8413	4.2016	670.64	329.14
91	964.63	3.8151	4.2062	673.29	310.62
96	961.19	3.789	4.2112	675.6	293.86

Appendix F

Specifications of LS-2 Collectors

Table 13 Specifications of LS-2 Collectors

Parameter	SNL LS-2	Unit
Year	1988	
Max. Operating temp.	390	^{0}C
Collector aperture width	5	M
Collector length	7.8	M
Collector reflectance	0.935	-
Focal length	1.40	M
Mean focus distance	1.84	M
Rim angle	80	Degree
Acceptance angle	1.59	Degree
Geometric concentration ratio	22.74	-
Receiver outer diameter	0.070	m
Receiver inner diameter	0.066	m
Cover outer diameter	0.125	m
Cover inner diameter	0.119	m
Cover thickness	0.003	m
Absorber thermal conductivity	54	W/m.K
Cover thermal conductivity	0.78	W/m.K
Absorber absorbance	0.96	-
Cover emittance	0.86	-
Cover transmittance	0.95	-
Cover absorbance	0.02	-
Cover extinction coefficient	12.5	m^{-1}
Cover refractive index	1.526	-
Absorber material	316L SS with a high solar absorptance Cermet coating	
Cover material	Pyrex	
Mirror material	MIRO-SUN	
Annulus condition	Evacuated	

References

[1]   DOE, 2012. SunShot Vision Study. NREL Report No. BK-5200-47927; DOE/GO-102012-3037. Washington DC: U.S. Department of Energy.

[2]   DOE, 2014. SunShot Initiative Portfolio Book. Washington DC: U.S. Department of Energy.

[3]   SEAI., Q4 2014. SMI Fact Sheet. Solar Energy Industries Association.

[4]   Kenneth A. Kroos and Merle C. Potter, 2015. Thermodynamics for Engineers, 15th Edition; Cengage Learning; USA

[5]   Dunlap, M.A., Marion, W. and Wilcox, S., 1994. Solar Radiation Data Manual for Flat-Plate and Concentrating Collectors; NREL; USA;

[6]   S.A. Sharaf Eldina, M.S. Abd-Elhadyb, and H.A. Kandilc, 2016. Feasibility of solar tracking systems for PV panels in hot and cold regions; Renewable Energy; 85; PP. 228-233.

[7]   John A. Duffie and William A. Beckman, 2013. Solar Engineering of Thermal Processes; 4th Edition; John Wiley and Sons; USA

[8]   Cheng, Z. D., He, Y. L., Cui, F. Q., Xu, R. J., & Tao, Y. B., 2012. Numerical simulation of a parabolic trough solar collector with non-uniform solar flux conditions by coupling FVM and MCRT method. Solar Energy, 86(6), 1770-1784.

[9]   He, S., Kim, W. S., & Jackson, J. D., 2008. A computational study of convective heat transfer to carbon dioxide at a pressure just above the critical value. Applied Thermal Engineering, 28(13), 1662-1675

[10]   Mehos, M., Kabel, D., Smithers, P., 2009. Planting the Seed, Greening the Grid with Concentrating Solar Power. IEEE Power & Energy Magazine. Vol. 7, No. 3, May/June.

[11]   Turchi, C. 2009. Calculations of Ideal CSP Resource Potential and Land Area in Seven Southwestern States. Golden, CO: NREL

[12]   Gupta, S., Saltanov, E., Mokry, S. J., Pioro, I., Trevani, L., & McGillivray, D. 2013. Developing empirical heat-transfer correlations for supercritical CO2 flowing in vertical bare tubes. Nuclear Engineering and Design, 261(0), 116-131

[13] Kim, M., Pettersen, J., & Bullard, C. W. 2004. Fundamental process and system design issues in CO2 vapor compression systems. Progress in Energy and Combustion Science, 30(2), 119-174.

[14] Xiao-Dong, N., Hiroshi, Y., Xin-Rong, Z., Yushiro, I., & Naoki, H. 2011. Experimental study of heat transfer characteristics of supercritical CO2 fluid in collectors of solar Rankine cycle system. Applied Thermal Engineering, 31, 1279-1285.

[15] V. Dostal, M.J. Driscoll, P. Hejzlar, 2004. A Supercritical Carbon Dioxide Cycle for Next Generation Nuclear Reactors. Advanced Nuclear Power Technology Program. MIT-ANP-TR-100. Massachusetts Institute of Technology, Cambridge (MA) Available from: http://hdl.handle.net.ezproxy.library.unlv.edu/1721.1/17746

[16] Yifang Gong, N.A. Carstens, M.J. Driscoll, I.A. Matthews. 2006. Analysis of Radial Compressor Options for Supercritical CO_2 Power Conversion Cycles. Report No: MIT-GFR-034

[17] Steven A. Wright, Ross F. Radel, Milton E. Vernon, Gary E. Rochau, and Paul S. Pickard, 2010. Operation and Analysis of a Supercritical CO2 Brayton Cycle. Sandia National Laboratories. SAND2010-0171

[18] Khanna, S., Kedare, S. B., & Singh, S. 2013. Analytical expression for circumferential and axial distribution of absorbed flux on a bent absorber tube of solar parabolic trough concentrator. Solar Energy, 92(0), 26-40

[19] Ahn, Y., Bae, S. J., Kim, M., Cho, S. K., Baik, S., Lee, J. I., & Cha, J. E. 2015. Review of supercritical CO_2 power cycle technology and current status of research and development. Nuclear Engineering and Technology

[20] H.J. Lee, H. Kim, C. Jang, 2014. Compatibility of candidate structural materials in high-temperature S-CO2 environment. Supercritical CO2 Power Symposium, Pittsburgh (PA)

[21] Was, G. S., Ampornrat, P., Gupta, G., Teysseyre, S., West, E. A., Allen, T. R., Pister, C. 2007. Corrosion and stress corrosion cracking in supercritical water. Journal of Nuclear Materials, 371(1–3), 176-201

[22] Cengel, Y. A., Boles, M. A. 2014. Thermodynamics an Engineering Approach. 8th Ed. McGraw-Hill Education. ISBN: 978-0-07-339817-4

[23] Cheng, Z. D., He, Y. L., Xiao, J., Tao, Y. B., & Xu, R. J. 2010. Three-dimensional numerical study of heat transfer characteristics in the receiver tube of parabolic trough solar collector. International Communications in Heat and Mass Transfer, 37(7), 782-787.

[24] Naeeni, N., & Yaghoubi, M. 2007. Analysis of wind flow around a parabolic collector (2) heat transfer from receiver tube. Renewable Energy, 32(8), 1259-1272.

[25] Mullick, S. C., & Nanda, S. K. 1989. An improved technique for computing the heat loss factor of a tubular absorber. Solar Energy, 42(1), 1-7.

[26] Hachicha, A. A., Rodríguez, I., Castro, J., & Oliva, A. 2013. Numerical simulation of wind flow around a parabolic trough solar collector. Applied Energy, 107, 426-437.

[27] Paetzold, J., Cochard, S., Vassallo, A., & Fletcher, D. F. 2014. Wind engineering analysis of parabolic trough solar collectors: The effects of varying the trough depth. Journal of Wind Engineering and Industrial Aerodynamics, 135, 118-128

[28] Feher, E.G. 1967.The Supercritical Thermodynamic Power Cycle. Douglas Paper No. 4348, IECEC, Miami Beach (FL)

[29] G. Angelino, G. 1968. Carbon dioxide condensation cycles for power production, ASME Paper No. 68-GT-23, J. Eng. Power, 90, pp. 287–295

[30] Iverson, B. D., Conboy, T. M., Pasch, J. J., & Kruizenga, A. M. 2013. Supercritical CO_2 Brayton cycles for solar-thermal energy. Applied Energy, 111(0), 957-970.

[31] Cheang, V. T., Hedderwick, R. A., & McGregor, C. 2015. Benchmarking supercritical carbon dioxide cycles against steam rankine cycles for concentrated solar power. Solar Energy, 113(0), 199-211.

[32] Singh, R., Miller, S. A., Rowlands, A. S., & Jacobs, P. A. 2013. Dynamic characteristics of a direct-heated supercritical carbon-dioxide brayton cycle in a solar thermal power plant. Energy, 50(0), 194-204.

[33] Lobón, D. H., & Valenzuela, L. 2013. Impact of pressure losses in small-sized parabolic-trough collectors for direct steam generation. Energy, 61(0), 502-512.

[34] Serrano-Aguilera, J. J., Valenzuela, L., & Parras, L. 2014. Thermal 3D model for direct solar steam generation under superheated conditions. Applied Energy, 132(0), 370-382.

[35] Behar, O., Khellaf, A., & Mohammedi, K. 2015. A novel parabolic trough solar collector model – validation with experimental data and comparison to engineering equation solver (EES). Energy Conversion and Management, 106, 268-281.

[36] Dudley V, Kolb G, Sloan M, Kearney D. 1994. SEGS LS2 solar collector-test results. Report of Sandia National Laboratories, SAN94-1884.

[37] Forristall R. 2003. Heat transfer analysis and modeling of a parabolic trough solar receiver implemented in engineering equation solver. Colorado: National Renewable Energy Laboratory (NREL).

[38] Jiji, M. Latif, 2009. Heat convection, 2nd ed. Springer

[39] Bazargan, M., Mohseni, M. 2012. Algebraic zero-equation versus complex two-equation turbulence modeling in supercritical fluid flows. Computers & Fluids, 60(0), 49-57

[40] Edward J. Parma, Steven A. Wright, Milton E. Vernon, Darryn D. Fleming, Gary E. Rochau, Ahti J. Suo-Anttila, Ahmad Al Rashdan, and Pavel V. Tsvetkov, 2011. Supercritical CO_2 Direct Cycle Gas Fast Reactor (SC-GFR) Concept, SANDIA REPORT, SAND2011-2525

[41] D. Bella, A. Francis (May 24–25, 2011. Gas turbine engine exhaust waste heat recovery navy shipboard module development, Supercritical CO_2 Power Symposium, Boulder (CO)

[42] Niu, X., Yamaguchi, H., Zhang, X., Iwamoto, Y., & Hashitani, N. 2011. Experimental study of heat transfer characteristics of supercritical CO_2 fluid in collectors of solar Rankine cycle system. Applied Thermal Engineering, 31(6–7), 1279-1285.

[43] Kim, Y. M., Kim, C. G., & Favrat, D. 2012. Transcritical or supercritical CO_2 cycles using both low- and high-temperature heat sources. Energy, 43(1), 402-415.

[44] Ničeno, B., & Sharabi, M. 2013. Large eddy simulation of turbulent heat transfer at supercritical pressures. Nuclear Engineering and Design, 261(0), 44-55.

[45] Wang, K., Xu, X., Wu, Y., Liu, C., & Dang, C. 2015. Numerical investigation on heat transfer of supercritical CO2 in heated helically coiled tubes. The Journal of Supercritical Fluids, 99(0), 112-120.

[46] Mohseni, M., & Bazargan, M. 2012. Modification of low Reynolds number k–ε turbulence models for applications in supercritical fluid flows. International Journal of Thermal Sciences, 51(0), 51-62.

[47] Hachicha, A. A., Rodríguez, I., Capdevila, R., & Oliva, A. 2013. Heat transfer analysis and numerical simulation of a parabolic trough solar collector. Applied Energy, 111(0), 581-592.

[48] Fernández-García, A., Zarza, E., Valenzuela, L., & Pérez, M. 2010. Parabolic-trough solar collectors and their applications. Renewable and Sustainable Energy Reviews, 14(7), 1695-1721.

[49] Hachicha, A. A., Rodríguez, I., Lehmkuhl, O., & Oliva, A. 2014. On the CFD&HT of the flow around a parabolic trough solar collector under real working conditions. Energy Procedia, 49(0), 1379-1390.

[50] Hachicha, A. A., Rodríguez, I., & Oliva, A. 2014. Wind speed effect on the flow field and heat transfer around a parabolic trough solar collector. Applied Energy, 130(0), 200-211.

[51] Zemler, M. K., Bohl, G., Rios, O., & Boetcher, S. K. S. 2013. Numerical study of wind forces on parabolic solar collectors. Renewable Energy, 60(0), 498-505.

[52] Wang, P., Liu, D. Y., & Xu, C. 2013. Numerical study of heat transfer enhancement in the receiver tube of direct steam generation with parabolic trough by inserting metal foams. Applied Energy, 102(0), 449-460.

[53] S. Koshizuka, N. Takano, and Y. Oka. 1995. Numerical analysis of deterioration phenomena in heat transfer to supercritical water. Int. J. Heat Mass Transfer, 38(16), pp. 3077-3084.

[54] Naeeni, N., & Yaghoubi, M. 2007. Analysis of wind flow around a parabolic collector (1) fluid flow. Renewable Energy, 32(11), 1898-1916.

[55] S. H. Kim, Y. I. Kim, Y. Y. Bae, and B. H. Cho. 2004. Numerical simulation of the vertical upward flow of water in a heated tube at supercritical pressure. Proc. of ICAPP.

[56] S. He, S. W. Kim, P. X. Jiang, and J. D. Jackson, 2004. Simulation of mixed convection heat transfer to carbon dioxide at supercritical pressure. J. Mech. Eng. Sci., 218.

[57] F. Roelofs, 2004. CFD analysis of heat transfer to supercritical water owing vertically upward in a tube. Technical report, Netherlands Ministry of Economic Affairs.

[58] J. Yang, Y. Oka, Y. Yishiwatari, J. Liu, and J. Yoo, 2006. Numerical study of heat transfer in supercritical pressure water in tight fuel rod channels. Proc. Of ICAPP.

[59] K. W. Seo, M. H. Kim, M. H. Anderson, and M. L. Corradini. 2006. Heat transfer in a supercritical fluid classification of heat transfer regimes. Nucl. Technol., 154. Pp. 335-349.

[60] He, S., Kim, W. S., & Bae, J. H. (2008). Assessment of performance of turbulence models in predicting supercritical pressure heat transfer in a vertical tube. International Journal of Heat and Mass Transfer, 51(19–20), 4659-4675.

[61] Yamaguchi, H., Zhang, X. R., Fujima, K., Enomoto, M., & Sawada, N. 2006. Solar energy powered Rankine cycle using supercritical CO_2. Applied Thermal Engineering, 26(17–18), 2345-2354.

[62] Zhang, X. R., Yamaguchi, H., Fujima, K., Enomoto, M., & Sawada, N. 2007. Theoretical analysis of a thermodynamic cycle for power and heat production using supercritical carbon dioxide. Energy, 32(4), 591-599.

[63] Zhang, X. R., & Yamaguchi, H. 2008. An experimental study on evacuated tube solar collector using supercritical CO_2. Applied Thermal Engineering, 28(10), 1225-1233.

[64] Chen, L., & Zhang, X. 2014. Experimental analysis on a novel solar collector system achieved by supercritical CO_2 natural convection. Energy Conversion and Management, 77(0), 173-182.

[65] Song, Y., Wang, J., Dai, Y., & Zhou, E. 2012. Thermodynamic analysis of a transcritical CO_2 power cycle driven by solar energy with liquefied natural gas as its heat sink. Applied Energy, 92(0), 194-203.

[66] Feher, E.G. 1968. The supercritical thermodynamic power cycle, Energy Conversion, 8, pp. 85–90

[67] Angelino, G. 1968. Carbon Dioxide Condensation Cycles for Power Production, ASME Paper 68-GT-23.

[68] Chacartegui, R., Muñoz de Escalona, J. M., Sánchez, D., Monje, B., & Sánchez, T. 2011. Alternative cycles based on carbon dioxide for central receiver solar power plants. Applied Thermal Engineering, 31(5), 872-879.

[69] Yang, X., Ding, J., Shao, Y., & Fan, H. 2012. Numerical simulation study on the heat transfer characteristics of the tube receiver of the solar thermal power tower. Applied Energy, 90(1), 142-147.

[70] Ho, C. K., & Iverson, B. D. 2014. Review of high-temperature central receiver designs for concentrating solar power. Renewable and Sustainable Energy Reviews, 29(0), 835-846.

[71] Al-Sulaiman, F. A., & Atif, M. 2015. Performance comparison of different supercritical carbon dioxide Brayton cycles integrated with a solar power tower. Energy, 82(0), 61-71.

[72] Padilla, R. V., Soo Too, Y. C., Benito, R., & Stein, W. 2015. Exergetic analysis of supercritical CO2 Brayton cycles integrated with solar central receivers. Applied Energy, 148(0), 348-365.

[73] N.A. Carstens, P. Hejzlar, M.J. Driscoll, 2006. Control System Strategies and Dynamic Response for Supercritical CO_2 Power Conversion Cycles, MIT-GFR-038

[74] R.B. Vilim et al., Dynamic System Analysis of a Supercritical CO_2 Compression Loop, Proceedings of ICAPP '08 Anaheim, CA USA, June 8–12, 2008, Paper 8343.

[75] M. Utamura, Thermal-hydraulic characteristics of microchannel heat exchanger and its application to solar gas turbines, Proceedings of ASME Turbo Expo, 2007. Power for Land, Sea, and Air, May 14–17, 2007, Montreal, Canada.

[76] Lobón, D. H., Baglietto, E., Valenzuela, L., & Zarza, E. 2014. Modeling direct steam generation in solar collectors with multiphase CFD. Applied Energy, 113, 1338-1348.

[77] Roldán, M. I., Valenzuela, L., & Zarza, E. 2013. Thermal analysis of solar receiver pipes with superheated steam. Applied Energy, 103, 73-84.

[78] Hinze, J. O. 1975. Turbulence, McGraw-Hill series in mechanical engineering, 2nd ed.

[79] Choudhury, D. 1993. Introduction to the Renormalization Group Method and Turbulence Modeling. Fluent Inc. Technical Memorandum TM-107

[80] Marion William, Wilcox Stephen, 1994. Solar Radiation Data Manual for Flat-Plate and Concentrating Collectors, National Renewable Energy Laboratory

[81] Reference Fluid Thermodynamic and Transport Properties Database (REFPROP): Version 9.1, National Institute of Standards and Technology

[82] CD-Adapco, 2017. Star CCM+ 12.02.010-R8 users' guide

[83] Hongbo Liang, Shijun You, Huan Zhang, 2015. Comparison of Different Heat Transfer Models for Parabolic Trough Solar Collectors, Applied Energy, 148, 105-114

[84] Gueymard, C., 2004. "The sun's total and spectral irradiance for solar energy applications and solar radiation models". Solar energy, 76(4), pp. 423–453

[85] Goswami, D. Y., Kreith, F., Kreider, J. F., and Kreith, F., 2000. Principles of Solar Engineering. second ed., Taylor & Francis, Philadelphia, PA.

[86] Timothy A. Moss, and Doug A. Brosseau, 2005. SEGS LS2 Final Test Results for the Schott HCE on a LS-2 Collector. Report of Sandia National Laboratories, SAND2005-4034.

[87] Rodi, W. 1991. Experience with Two-Layer Models Combining the k-e Model with a One-Equation Model Near the Wall, 29th Aerospace Sciences Meeting, January 7-10, Reno, NV, AIAA 91-0216.

[88] ASHRAE, 2003. Methods of testing to Determine the Thermal Performance of Solar Collectors (ANSI approved), Standard 93-2003

[89] ASTM Standard E905-87, 2001. Standard Test Method for Determining Thermal Performance of Tracking Concentrating Solar Collectors

[90] NIST Standard Reference Database 10, 2004. NIST/ASME Steam Properties, Version 2.21

[91] Properties of Syltherm® 800 Heat Transfer Liquid, Midland, MI: Dow Corning Corporation, 1985

[92] Woolf, H. M., 1968. "On the Computation of Solar Evaluation Angles and the Determination of Sunrise and Sunset Times". National Aeronautics and Space Administration Report NASA TM-X-164, USA.

[93] Stine,W. B., and Harrigan, R.W., 1985. Solar Energy Fundamentals and Design: With Computer Applications. Wiley-Interscience, Apr.

[94] Goswami, D. Y., Kreith, F., Kreider, J. F., and Kreith, F., 2000. Principles of Solar Engineering. second ed., Taylor & Francis, Philadelphia, PA.

[95] Gueymard, C., 2004. "The sun's total and spectral irradiance for solar energy applications and solar radiation models". Solar energy, 76(4), pp. 423–453.

[96] Gueymard, C., 1995. SMARTS2: A Simple Model of the Atmospheric Radiative Transfer of Sunshine: Algorithms and Performance Assessment. Tech. Rep. FSECPF-270-95, Florida Solar Energy Center Cocoa, FL, USA.

[97] Iqbal, M., 1983. An Introduction to Solar Radiation, Academic, Toronto

[98] Spencer, J., W., 1971. Fourier Series Representation of the Position of Sun, Search, 2 (5), 172

[99] Hay, J. E. and J. A. Davies, 1980. Calculation of the Solar Radiation Incident on an Inclined Surface, Proceedings of the First Canadian Solar Radiation Data Workshop, Toronto, Canada, P. 50

[100] Rendl, D. T., W. A. Beckman and J. A. Duffie, 1990. Evaluation of Hourly Tilted Surface Radiation Models, Solar Energy, 45, 9

[101] Cengel, Yunus A., and Boles, Michael A. 2014. Thermodynamics: An Engineering Approach, 8th ed., McGraw-Hill Education, 2 Penn Plaza, New York

[102] Berdahl, P. and M. Martin, 1984. Emissivity of Clear Skies, Solar Energy, 32, 5 663

[103] Borgnakke, Claus and Sonntag, Richard E. 2013. Fundamentals of Thermodynamics; 8th ed., John Wiley and Sons; USA

[104] Gallaway, Tara, 2011. Modeling of Flow and Heat Transfer Fluids at Supercritical Conditions; Dissertation; Rensselaer Polytechnic Institute Troy, New York, USA

Curriculum Vitae

Graduate College

University of Nevada, Las Vegas

Samad Gharehdaghimollahajloo

gharehda@gmail.com

Samad Gharehdaghi Mollahajloo was born in Tehran, Iran in June 1980. He received his bachelor degree in mechanical engineering from K. N. Toosi University of Technology in 2003. After gaining three years of experience in construction projects he pursued his master of science at University of Tehran in Mechanical Engineering – Energy Conversion. At University of Tehran, Samad was especially trained in designing and computational analyzing of turbomachinery which allowed him to join power plant industry upon his graduation. In 2012, Samad began doctoral studies at University of Nevada, Las Vegas under the guidance of Dr. Samir F. Moujaes on thermal-fluid sciences. His most significant areas of research in PhD program were experimental and numerical analysis of the flow field and heat transfer in Solar Thermal Power plants and HVAC systems.